“Chrome Poisoning of Non-Manganiferous Cathode Materials for Solid Oxide Fuel Cells (SOFCs)“

„Chromvergiftung von nicht-manganhaltigen Kathodenmaterialien für die Festoxid-Brennstoffzelle (SOFC)“

Von der Fakultät für Mathematik, Informatik und Naturwissenschaften der RWTH Aachen University zur Erlangung des akademischen Grades eines Doktors der Ingenieurwissenschaften genehmigte Dissertation

vorgelegt von

Kevin Schiemann, M.Sc.

aus

Essen

Berichter: Prof. Dr. Rüdiger-A. Eichel

Prof. Dr. Regina Palkovits

Prof. Dr. Lorenz Singheiser

Tag der mündlichen Prüfung: 03.07.2018

Table of Contents

List of Figures

List of Tables

Table of Abbreviations

AC	=	Alternating Current
APU	=	Auxiliary Power Unit
ASC	=	Anode-Supported Cell
ASR	=	Area Specific Resistance
C	=	Capacitor
CE	=	Counter Electrode
DBL	=	Diffusion Barrier Layer
DC	=	Direct Current
DRT	=	Distribution of Relaxation Times
D_{50}	=	Median Particle Size Distribution
EC	=	Equivalent Circuit
EDX	=	Energy-Dispersive X-Ray Spectroscopy
EIS	=	Electrochemical Impedance Spectroscopy
ESC	=	Electrolyte-Supported Cell
FZJ	=	Forschungszentrum Jülich
G_1	=	Gerischer Element
GDC	=	Gadolinium Doped Ceria
HC	=	Half-Cell
ICP-OES	=	Inductively Coupled Plasma-Optical Emission Spectrometry
ICSD	=	Inorganic Crystal Structure Database
I/V	=	Current/Voltage
KIT	=	Karlsruher Institut für Technologie
KK	=	Kramers-Kronig
MCFC	=	Molten Carbonate Fuel Cell
OCP	=	Open-Cell Potential
OCV	=	Open-Cell Voltage
PEM	=	Proton Exchange Membrane Fuel Cell
PSD	=	Particle Size Distribution
PVD	=	Physical Vapor Deposition
Q	=	Constant Phase Element
R	=	Resistance
RE	=	Reference Electrode
R_{ohm}	=	Ohmic Resistance
R_{pol}	=	Polarization Resistance
R_{total}	=	Total Cell Resistance
SEM	=	Scanning Electron Microscopy
SE	=	Sense Electrode
SOFC	=	Solid Oxide Fuel Cell
TPB	=	Triple Phase Boundary
W_1	=	Warburg Element
WE	=	Working Electrode
W_s	=	Finite Warburg Element
XPS	=	X-Ray Photoelectron Spectroscopy
XRD	=	X-Ray Diffraction
YSZ	=	Yttria Stabilized Zirconia Dioxide

Statutory Declaration

I declare that I have authored this thesis independently, that, to the best of my knowledge, I have not used other than the declared sources/resources and that I have explicitly marked all material which has been quoted either literally or by content from the used sources.

Place, Date ***Signature***

Acknowledgement

The current Phd-thesis was written during my work at the Institute for Energy and Climate Research (IEK-9: Fundamental Electrochemistry) which is part of the Forschungszentrum Jülich GmbH.

First and foremost, I want to thank Prof. Dr. R-A. Eichel for the opportunity and the supervision of this thesis. Furthermore, I especially want to thank Dr. L.G.J. de Haart and Dr. I.C. Vinke for the theoretical as well as experimental guidance of my work. It was my pleasure to work in your group and benefit from your excellent knowledge in the fields of "fuel-cells" and "electrochemistry". Furthermore, thanks to Prof. Dr. R. Palkovits and Prof. Dr. L. Singheiser for being my second and third examiner.

I also want to thank Dr. Granwehr and Dr. Kungl for their continuous support of my work and the many good scientific advices they gave me. Special thanks are also directed to Dr. Vibhu, Dr. Hartmann, Dr. Nischwitz and Andreas Mertens-von Rüden for their help to perform high quality analysis of my data and samples. I also want to appreciate the work of Trutz Theuer and Cinar Karacan, who wrote their Master-Thesis under my supervision and helped to install custom-built electrochemical test-rigs. Additional thanks also to all my good colleagues with whom I liked to spent my lunch break.

Many thanks also to Dr. N.H. Menzler for the possibility to cooperate with the IEK-1 and Alexander Beez ("my brother in chrome") for many interesting discussions about the topic of "chrome poisoning". Furthermore, I want to thank Mr. Jan Plewinski for the continuous preparation of specimens in order to continue my work.

Most important I want to thank my mother Carmen Schiemann, my father Klaus Schiemann and my girlfriend Stefanie Seidel for their constant support of my career. Finally, special thanks to my grandfather Dipl.-Ing. Heinz Schiemann to whom I would like to dedicate this Phd-thesis. Your ambitions, persistence and success have extremely impressed me and will guide me through my entire life.

Dedicated to ***Dipl.-Ing. Heinz Schiemann***

1. Abstract

English

Solid Oxide Fuel Cells which represent highly efficient energy conversion concepts, can be considered as alternative technologies for de-/centralized power plants or in the automotive sector as auxiliary power units. However, chrome poisoning accompanied with cathode degradation has been identified as a major cause for reduced SOFC stack/component lifetimes. As in-depth knowledge of the mechanism has been obtained for (La,Sr)MnO_3 (LSM) based cathode materials, it was long thought that (La,Sr)(Co,Fe)$O_{3-\delta}$ (LSCF) cathodes were less susceptible towards chrome poisoning, because of other mechanisms, i.e. mainly the formation of less conductive $SrCrO_4$-phases on the cathode surface. Recently, however, similar poisoning effects as seen for LSM have been observed for LSCF as well, inducing an additional in-depth investigation of the chrome poisoning of non-manganiferous cathode materials. Here, it should be identified whether interactions of chrome and LSCF-cathode materials can be attributed to a chemical or electrochemical reaction mechanism. To realize this objective, anode-supported SOFCs (full-cells) and symmetrical electrolyte-supported half-cells were investigated under various different operating conditions, such as the working temperature, cathode-gas humidity, applied current densities and in absence/presence of a Cr-source. An interplay of electrochemical in-operando direct- and alternating-current techniques, i.e. current-voltage characteristics and electrochemical impedance spectroscopy, as well as several pre/post-test characterization methods showed enhanced Cr-related cell degradation especially at high operating temperatures and current densities in humid cathode-gas atmospheres. It was shown, that besides the formation of $SrCrO_4$-phases (Cr(VI)), also Cr(III)-species were formed during operation. Here, the formation of Cr(VI)-species could be solely confirmed on the LSCF-cathode surface whereas Cr(III) has been detected on top of the electrode and at the triple phase boundary between electrode, electrolyte and gas-phase. With the implementation of the new 2-D DRT method, the presence of four different processes as well as a fifth process that was strongly superimposed by anodic contributions, had been confirmed. This knowledge facilitated the adaption of a suitable equivalent circuit model for the electrochemical description of anode excluding half-cells with $La_{0.58}Sr_{0.4}Co_{0.2}Fe_{0.8}O_{3-\delta}$-, $La_{0.58}Sr_{0.4}FeO_{3-\delta}$- and $La_{0.58}Sr_{0.4}CoO_{3-\delta}$-cathodes. In comparison to the analysis of full-cells, half-cells showed enhanced degradation tendencies and enabled a more detailed analysis, also with regard to the B-site stoichiometry of the perovskite cathode material. The results showed that, in fact, the deposition of Cr(VI)-species on the cathode surface can be affected with the application of higher current densities (i.e. higher cathodic overpotentials). This, however, does not confirm a direct electrochemical degradation mechanism as the formation can also be indirectly induced by disassembly of the material, leading to a chemical degradation mechanism. As measurements at (continuously) high overpotentials did not reveal an increased formation of Cr(III) at the cathode surface compared to measurements at lower overpotentials, it is assumed to be chemically induced. However, the presence of Cr(III)-species at the triple-phase boundary can be identified as

solely electrochemically induced as no signal has been detected for the occurrence of Cr(VI) in this electrochemical highly active region.

Deutsch

Festoxidbrennstoffzellen (engl. Solid Oxide Fuel Cells, SOFCs), die hocheffiziente Energiekonversionskonzepte darstellen, können als alternative Technologien eine Anwendung in de-/zentralen Energiekraftwerken oder als Hilfsaggregat im automobilen Sektor finden. Allerdings, ist die durch die Chromvergiftung hervorgerufene Degradation des Kathodenmaterials als eine der Hauptursachen für eine reduzierte Langlebigkeit von Einzelkomponenten als auch von ganzen Zellstacks identifiziert worden. Aufgrund eines vertiefenden Verständnisses bzgl. der Degradationsmechanismen von (La,Sr)MnO_3-Kathoden (LSM) war lange Zeit davon auszugehen, dass (La,Sr)(Co,Fe)$O_{3-\delta}$-Kathoden, aufgrund anderer Mechanismen (d.h. hauptsächlich der Bildung von $SrCrO_4$-Phasen auf der Kathodenoberfläche) weniger empfindlich gegenüber Chromvergiftung sind. Allerdings konnten durch kürzlich durchgeführte Stackstudien ähnliche Vergiftungserscheinungen für LSCF-Kathoden, wie auch bereits in der Vergangenheit für LSM-Kathoden, festgestellt werden. Durch weiterführende Studien dieser nicht-manganhaltigen Kathodenmaterialien, sollen Wechselwirkungen zwischen Chromspezies als auch dem Kathodenmaterial identifiziert und einem geeigneten Reaktionsmechanismus (chemisch bzw. elektrochemisch) zugeschrieben werden. Zur Umsetzung dieses Ziels werden anodengestützte Zellkonzepte (Vollzellen) als auch symmetrische, elektrolytgestützte Halbzellen unter verschiedenen Betriebsbedingungen in Gegenwart bzw. Abstinenz einer Chromquelle untersucht (z.B. Temperatur, Luftfeuchte, Stromdichte). Im Zusammenspiel von sowohl elektrochemischen In–Operando Gleich- sowie Wechselstrommessungen (d.h. Strom-Spannungs-Charakteristiken und Impedanzspektroskopie) als auch Pre/Post-Test Charakterisierungs-methoden, können starke chrombedingte Zelldegradationsraten insbesondere bei hohen Betriebstemperaturen, hohen Stromdichten und in feuchten Atmosphären, festgestellt werden. Hierbei ist es möglich, neben der Bildung von $SrCrO_4$-Phasen (Cr(VI)) auch die Präsenz von Cr(III)-Verbindungen nachzuweisen. Während die Bildung von Cr(VI)-Phasen ausschließlich auf der LSCF-Oberfläche bestätigt werden kann, ist es möglich Cr(III) an der Elektrodenoberfläche sowie nahe der Dreiphasengrenze zwischen Elektrode, Elektrolyt und Gasphase zu detektieren. Darüber hinaus können, mit Hilfe einer neu entwickelten 2-D DRT Methode, vier verschiedene Prozesse (sowie ein durch Anodenbeiträge stark überlagerter fünfter Prozess) identifiziert werden. Anhand dieser Kenntnisse ist es möglich ein zuvor adaptiertes Ersatzschaltbild, hinsichtlich der Verwendung von symmetrischen Halbzellen (Ausschluss einer Anode) mit $La_{0.58}Sr_{0.4}Co_{0.2}Fe_{0.8}O_{3-\delta}$-, $La_{0.58}Sr_{0.4}FeO_{3-\delta}$- und $La_{0.58}Sr_{0.4}CoO_{3-\delta}$-Kathoden anzupassen, um eine optimierte Beschreibung des vorhandenen Systems zu gewährleisten. Im Gegensatz zur Analyse von anodengestützten Vollzellen, ermöglicht eine erhöhte chrombezogene Degradationsrate von elektrolytgestützten Halbzellen eine detailliertere Betrachtung der relevanten Operations-/Einflussparameter (z.B. auch der B-Platz Dotierung des Kathodenmaterials). Durch die Ergebnisse kann eine erhöhte Abscheidung von Cr(VI)-Verbindungen auf der Elektrodenoberfläche in direkten Zusammenhang mit der Verwendung höherer Stromdichten (d.h. stärker Überpotenziale) gesetzt werden. Allerdings

kann hierdurch nicht auf einen direkten elektrochemischen Degradationsmechanismus geschlossen werden, da hohe Stromdichten ebenfalls zur Destabilisierung des Kathodenmaterials beitragen können und somit eine chemische Degradation implizieren (mit Cr(VI) als Hauptprodukt und Cr(III) als Nebenprodukt). Außerdem zeigen Messungen bei konstant hohen Überpotenzialen (im Vergleich zu Messungen bei niedrigen Überpotenzialen) keine Zunahme in der Bildung von Cr(III)-Verbindungen an der Kathodenoberfläche (bzw. einer Abnahme des Verhältnisses zwischen Cr(VI):Cr(III)), sodass deren Bildung einem chemischen Prozess zugeschrieben werden kann. Im Gegensatz hierzu kann die Präsenz von Cr(III) an der elektrochemisch hochreaktiven Dreiphasengrenze lediglich einem elektrochemischen Degradationsmechanismus zugeschrieben werden, da die Präsenz von Cr(VI)-Verbindungen, trotz geeigneter Analysemethoden, nicht nachgewiesen werden konnte.

2. Motivation

In times of global warming, induced by a progressive industrial globalization and a steady use of fossil fuels with continuous shrinkage of their occurrences, reliable renewable energies sources gain in importance. A strong disadvantage and most probably the main reason why renewable energy technologies still remain as niche technologies in most industrial countries, is their inconsistent availability throughout the year (e.g. weather and season dependency, day & night cycle etc.). As a result, many of these technologies remain underdeveloped and thus cannot provide sufficient performance.

In this regard, fuel cells represent promising and already well-developed highly efficient energy conversion technologies. Fuel cells can be used as auxiliary power units (APUs) in the automotive sector and in de-/centralized power plants or as backup alternatives for large companies. Especially high-temperature modifications (e.g. Solid Oxide Fuel Cells, SOFCs) possess the potential to provide high cell efficiencies and sufficient power outputs. In order to successfully commercialize SOFCs, operational-lifetimes of more than 100,000 h have to be realized. An approach to guarantee these elevated lifetimes is to investigate long-term degradation phenomena of the utilized materials. As these can be caused by a variety of different parameters, such as the gas-supply and purity, the composition of the interconnecting materials (Cr-content, protective layer) etc., detailed knowledge of the individual aging mechanisms as well as the influencing operational parameters is of critical importance. In this regard, it is possible to define countermeasures and, thus, reduce or at best prevent degradation effects.

As one of the major degradation issues and the main aging cause of SOFC cathode materials, chrome poisoning leads to drastically reduced SOFC component performances in combination with a decreased system durability [1,2]. For this reason, deeper understanding of the related chrome degradation mechanisms is of fundamental interest. Since $(La,Sr)(Co,Fe)O_3$ based cathodes show both, a good electronic and sufficient ionic conductivity, these materials are considered to be the best state-of-the-art cathode materials. The mixed ionic-electronic conducting properties can be also considered as the main reason for LSCF-materials to be less susceptible towards chrome poisoning than pure electronic conductors such as $(La,Sr)MnO_3$. Nevertheless, these materials show strong tendencies in the formation of mobile SrO-species, even under open cell conditions, which can enhance the formation of Cr-species (e.g. $SrCrO_4$). Recently performed short-term stack tests also showed similar poisoning effects for LSCF materials as seen for LSM cathodes, indicating a more complex poisoning behavior than assumed so far [3–5].

The main goal of this thesis is to define whether the interactions of chrome and the non-manganiferous cathode material LSCF can be attributed to a chemical or an electrochemical mechanism (or both). Furthermore, in particular for the electrochemical induced degradation, emphasis should be put to the chrome deposition preferred local areas and promoting conditions such as the temperature, cathode-gas humidity, applied current density (overpotential) and the cathode compositions (B-site stoichiometry). Finally, with this knowledge it should be possible to define countermeasures and improve operational conditions.

3. Introduction

Fuel cells, in general, represent some of the most efficient energy conversion concepts that have been developed in recent years [6]. Since their development by Grove and Schönbein (around the year 1838) and the basic zirconia related assumptions and proposals of Nernst et. al. (around 1900) [6,7], many different cell variations have been developed and considerable advances are still being made. In general, it can be distinguished between low-temperature fuel cells (< 200 °C) and high temperature fuel cell concepts (> 600 °C). In case of low-temperature fuel cells, the concepts of phosphoric-acid fuel cells (PAFCs), alkaline fuel cells (AFCs), proton-exchange membrane fuel cells (PEMFCs) and direct methanol fuel cells (DMFCs) are well known [8]. To give an example, PEMFCs consist of two electrodes and a polymer-based, proton conduction Nafion electrolyte (developed from Teflon, PTFE). As PEMFCs represent a low-temperature fuel cell variation, typical operating temperatures are 85 °C-105 °C which make this cell type interesting for its use in mobile applications (e.g. automotives) [9]. However, PEMFCs suffer from the adsorption of carbon monoxide within the electrochemically active area and, thus, reduced cell performances. For this reason, the appearance of CO has to be prevented by the utilization of ultrapure combustion gasses [10].
Contrary to PEMFCs and other low-temperature modifications, high-temperature SOFCs are operated at temperatures between 650-900 °C and enable higher efficiencies and large power outputs. As one of the most promising cell variations for mobile and stationary applications, the next chapters of this paragraph will provide detailed information about state-of-the-art SOFC research and development [9,10].

3.1. Solid Oxide Fuel Cells (SOFCs)

Solid Oxide Fuel Cells mainly consist of a cathode (air electrode), an anode (fuel electrode) as well as an electrode separating solid electrolyte. As the central component of the cell, the electrolyte represents a dense, electronically insulating and solely oxygen-ion conducting 8 mol-% yttria-stabilized zirconia dioxide (8YSZ) thin-film layer. Contrary to the dense electrolyte, both electrodes show porous and electronically conductive structures that are able to provide a sufficient gas transport to the electrochemically active triple-phase boundary (gas phase-electrode-electrolyte, TPB). Here, NiO serves as the standard anode material and is reduced to elemental Ni by gradually introducing H_2 during the cell starting period. For cathodes, however, several different materials such as $La_{0.58}Sr_{0.4}MnO_{3-\delta}$ (LSM) or $La_{0.58}Sr_{0.4}Co_{0.2}Fe_{0.8}O_{3-\delta}$ (LSCF, both incl. stoichiometric variations) have been established within the past years.
Such as most other types of fuel cells, also SOFCs are operated under continuous gas-flows in the anode and cathode room, respectively (Figure 3.1). According to (1), air or pure oxygen is led through the porous cathode structure where it is reduced by electrons from the external circuit. At the same time, pure hydrogen (H_2) flows through the anode structure and is being oxidized. The resulting excess electrons are transported to the external circuit and are provided at the electrochemically active cathode. Throughout the transport through the external circuit, these electrons perform electrical work, which can be utilized by an electrical

consumer. Since the 8YSZ electrolyte represents a dense and insulating layer, no hydrogen can diffuse towards the cathode. As solely O^{2-}-ions can overcome the electrolyte, the oxygen partial pressure difference between the anode and cathode room serves as the driving force of the redox reaction. The migration related transport through the electrolyte is described as a hopping mechanism of oxygen ions by occupation of oxygen vacancies [11]. By reaching the anode, the O^{2-}-ions react with hydrogen under the formation of H_2O (2). The complete reaction is defined in (3).

Reduction: $$\frac{1}{2}\,O_2 + 2\,e^- \rightleftharpoons O^{2-} \quad (1)$$

Oxidation: $$H_2 + O^{2-} \rightleftharpoons H_2O + 2\,e^- \quad (2)$$

Complete Reaction: $$H_2 + \frac{1}{2}\,O_2 \rightleftharpoons H_2O \quad (3)$$

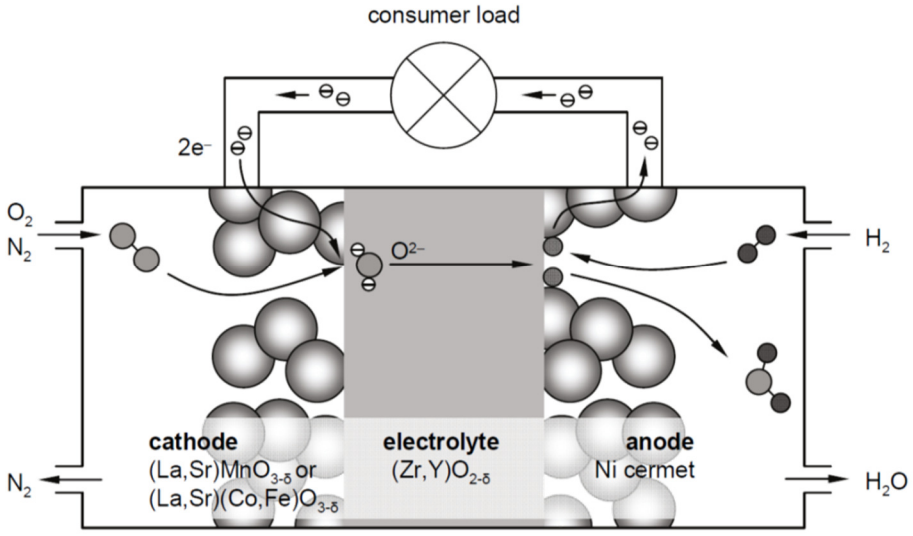

Figure 3.1: Scheme of the working principle of a Solid Oxide Fuel Cell (SOFC) [12].

Furthermore, the high operating temperatures of SOFCs enable the utilization of methane (CH_4) as a combustion gas. This is a strong advantage compared to other fuel cell types as in case of CH_4 utilization, a direct internal reforming step is initiated at the anode side, leading to the production of H_2 (4). Alongside the internal reforming, also a shift reaction has to be mentioned which converts carbon monoxide (CO) residuals in humid atmospheres (H_2O) to thermodynamically preferred carbon dioxide (CO_2) and further H_2 (5). Additionally, with the production of CO_2 the possibility of a second reforming step with CH_4 arises (6) [6,8,13].

1. Reforming: $$CH_4 + H_2O \rightleftharpoons CO + 3\,H_2 \quad (4)$$

Shift-Reaction: $$CO + H_2O \rightleftharpoons CO_2 + H_2 \quad (5)$$

2. Reforming: $$CH_4 + CO_2 \rightleftharpoons 2\,CO + 2\,H_2 \quad (6)$$

3.1.1. Designs/Geometries

With the continuous development of the SOFC technology also new approaches in terms of cell design/geometry were investigated. Two main design alternatives emerged which are still in use today. The tubular design provides sufficient power densities and was already used as an alternative power-plant with performances of up to 20-200 kW [14]. A strong advantage of the tubular concept is the prevention of any sealing in the high-temperature area [8,14]. This simplifies the assembling procedure and leads to reduced costs. As a disadvantage, long conduction pathways through the cell have to be mentioned that lead to higher ohmic resistances and, thus, diminish the practically achievable current densities. Another common cell concept is the planar design. Here, short conduction pathways enable significantly higher current densities as for the tubular alternative. Furthermore, a planar design allows for cost-efficient production procedures such as screen printing or tape casting. These processes are favorable since they are already implemented into many large industrial production lines and can be realized with high production volumes. The main disadvantage of the planar design is the utilization of sealings in the high-temperature region. To withstand the elevated operating temperatures of a SOFC and provide sufficient sealing, expensive materials like glass solder have to be used. Nevertheless, the ease of production combined with the highest power output make this design concept the most favorable [14,15].

3.1.2. ASC & ESC configurations

The planar cell design can further be subgrouped into different cell architectures such as anode-supported cells (ASCs) and electrolyte supported cells (ESCs, both Figure 3.2). The ASC consists of a multilayered Ni-anode that can be divided into the mechanical stabilizing coarse anode substrate (400-600 µm) and a thin, fine structured anode functional layer (10 µm). Furthermore, a thin electrolyte (10-20 µm) and the cathode (40-60 µm) are deposited on top of the anode. In case of a non-manganiferous cathode material (e.g. LSCF), a diffusion barrier layer (DBL, 5-8 µm) is installed between cathode and electrolyte to prevent interdiffusion and the formation of a less conductive phase. In contrast to ASCs, ESCs consist of a thick electrolyte (150-300 µm) which serves as a mechanically stabilizing part of the cell and two electrodes with a thickness of 50 µm each (incl. DBL of 5-8 µm).

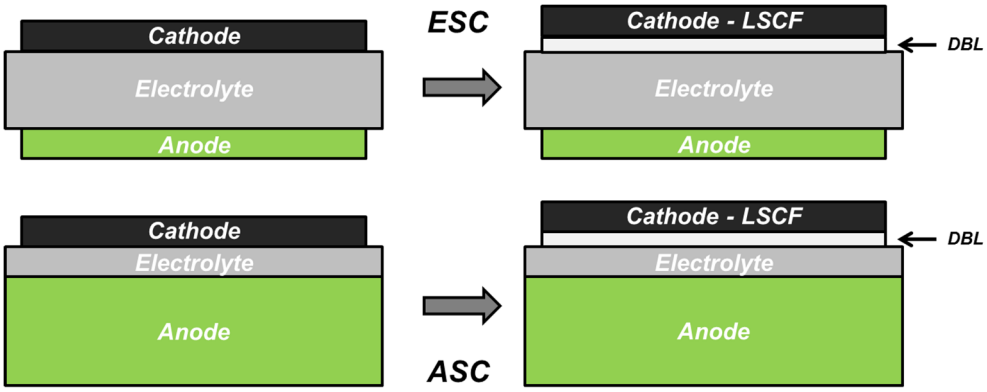

Figure 3.2: Structural scheme of anode-supported (ASCs) and electrolyte-supported SOFCs (ESCs) with and without additional diffusion barrier layer (DBL).

As already included within the cell specifications, the mechanically stabilizing functional layer differs for both cell types. Whereas ASCs consist of a multilayer anode, providing mechanical stability, ESCs shift this task to the electrolyte. Even though both cell architectures can be used, the ASC based systems are much more common due to higher power outputs at lower temperatures compared to their ESC counterparts. The reason for this can be attributed to a thinner electrolyte leading to much smaller ohmic losses. Furthermore, the possibility to work at lower operating conditions enables the replacement of expensive metal alloys by cheaper ferritic steels during stack construction [14].
Another promising cell architecture is the metal supported design (MSC). MSCs have the advantage of easy processing during stack construction but suffer from interdiffusion of atoms from the metal substrate into the anode material and vice versa. Since MSCs are still in an early stage of development and not focus of this thesis, they are not further discussed.

3.1.3. Cell Stacks

Single SOFCs can be connected in parallel or series to meet the requirements of high energy consuming applications. Therefore, each cell is stacked with a, so-called, interconnect by forming a stack repeating unit. Interconnects are bipolar plates which are equipped with numerous gas channels on both sides that provide a homogenous gas diffusion across the electrode surface. Common interconnect materials are ferritic steels like Crofer 22 APU and Crofer 22 H [16–19].
To improve the contact area between interconnects and cells, either thin metallic meshes or contact layers are installed/deposited on top of the ferritic steels. To successfully operate such a stack, each electrode has to be separated from the others electronically as well as in terms of mixing fuel and oxidant gases. These separations are accomplished with glass solder to prevent electronic shortcuts and uncontrolled formation of water [8].
At standard SOFC operating temperatures, a passivating Cr_2O_3 and $MnCr_2O_4$ oxidation layer is formed on top of the interconnect surface [20]. A problem is the evaporation of Cr-species from the interconnect oxide layers which can poison the air electrode (cathode). Here, Cr-poisoning can lead to the formation of passivating strontium chromate phases such as $SrCrO_4$ or $SrCr_2O_4$ and chrome(III)oxides (Cr_2O_3) which block electrochemically active areas of the cathode.

3.2. Degradation: Chrome Poisoning

Since Cr-poisoning was identified as one of the major issues for long-term SOFC performance degradation, several research groups recorded remarkable efforts in understanding the influence of several operational parameters on the poisoning behavior and the related poisoning mechanisms [8,21–24]. However, the focus of this thesis is set on the analysis of the Cr-poisoning behavior of LSCF cathodes, since they represent the actual standard air electrode materials for SOFC applications.

3.2.1. State-of-the-Art

As mentioned in the previous chapter, the thermodynamic instability of chrome at high temperatures and the resulting volatility of Cr(VI)-species within a SOFC system are a major

cause for reduced cathode and stack lifetimes, respectively. The following reactions represent the volatilization products in relation to dry (7) and humid gas atmospheres (8) [21,25].

Dry atmospheres: $$Cr_2O_{3\,(s)} + xO_{2(g)} \rightleftharpoons 2\,CrO_{3(g)} \quad (7)$$

Humid atmospheres: $$Cr_2O_{3\,(s)} + xO_{2(g)} + yH_2O_{(g)} \rightleftharpoons 2\,CrO_2(OH)_{2(g)} \quad (8)$$

It has been proven that the volatility of Cr-species is strongly affected by the oxygen partial pressure and water content at the air electrode. Here, the influence of Cr-species on the fuel electrode can be neglected as the present oxygen partial pressure is between 10^{-12} Pa and 10^{-7} Pa [25]. Ebbinghaus et al. [26] showed that $CrO_2(OH)_2$ can be determined as the dominant species in humid atmospheres whereas just small fractions of $CrO_{3(g)}$, $CrO(OH)_3$, CrO_2OH and $CrO(OH)_2$ were found at temperatures between 800 K - 1600 K. In accordance to the literature and the performed experiments, it can be stated that CrO_3 (dry conditions) and $CrO_2(OH)_2$ (humid conditions, 3 % H_2O) are the dominant species within the experiments performed for this thesis [27]. Furthermore, Chen et al. [27] described a strong decrease of the partial pressure of CrO_3 with decreasing the operational temperature ($1.4 \cdot 10^{-3}$ Pa at 900 °C and $3.4 \cdot 10^{-7}$ Pa at 600 °C). However, for $CrO_2(OH)_2$ the associated partial pressure decreased from a value of $9.2 \cdot 10^{-2}$ Pa (900 °C) to $1 \cdot 10^{-2}$ Pa (600 °C), representing a less strong temperature dependency as measured for CrO_3 . Chen et al. [27] also pointed out that higher chrome partial pressures inevitably lead to stronger chrome depositions. A study of Tucker et al. [28] described the chrome contamination of a wide range of metal oxides as well as of LSM and LSCF cathodes without contact to a Fe-Cr alloy. They identified surface diffusion from the Fe-Cr alloy and vapor deposition from the atmosphere as two separate pathways for chrome contamination. They specified the extent to which chrome deposition was caused by these pathways, heavily depending on the presence of MnO_x (LSM) or Co_3O_4 (LSCF) and thus the formation of $Mn_xCr_{3-x}O_4$ or $Co_{3-x}Cr_xO_4$ spinels [28]. Even though the formation of $Co_{3-x}Cr_xO_4$ phases could not be detected for LSCF cathodes (and Fe-Cr alloys), they suggested that cobalt is responsible for the chrome deposition. As several studies and internal FZJ short-term tests revealed the frequent presence of $SrCrO_4$ phases, mobile SrO is considered to be the main factor for chrome deposition on the surface of LSCF cathodes [21,23,29,30]. This fact was confirmed by the work of Zhen and Jiang [31] who substituted strontium with barium in LSCF-cathodes. They pointed out that the amount of chrome species found on the surface of $(La_{0.6}Ba_{0.4})(Co_{0.2}Fe_{0.8})O_{3-\delta}$ (LBCF) electrodes was significantly lower as compared to LSCF cathodes. They also showed that lower strontium contents in $(La_{0.6}Sr_{0.4-x}Ba_x)(Co_{0.2}Fe_{0.8})O_{3-\delta}$ (LSBCF) electrodes lead to a decreased amount of chrome deposits [21,32].

It is known that the deposition of chrome species on LSCF electrodes causes strong changes on oxygen surface exchange kinetics and diffusion processes [21]. By investigation of surface exchange kinetics and diffusion of oxygen isotope traces on chrome poisoned surfaces of dense LSCF pellets at 800 °C, Finsterbusch et al. [33] observed a significant reduction of the surface exchange rate constant on a 7 nm thick Cr_2O_3-film by one order of magnitude. In this regard, Bucher et al. [34] performed measurements of the chemical diffusion and oxygen surface exchange coefficient of dense LSC and LSCF samples at 600 °C in presence of chrome with

help of the conductivity relaxation method. The group reported a strong reduction of the oxygen surface exchange coefficient by a factor of 2 for dry and a factor of 5 in humid O_2/Ar atmospheres after 1000 h of operation/exposure. Furthermore, Lee et al. [35] reported strong increases in the polarization resistance at already low chrome impregnation contents of the electrodes (e.g. 0.01 wt%).

3.2.2. Poisoning Mechanisms

As already shown in the literature as well as proven by FZJ internal stack-tests, Cr-deposition for LSCF/YSZ systems preferentially occurs at the cathode surface rather than at the triple-phase boundary between cathode and electrolyte [21–23,29,30,36]. It is also stated that the dominant product of the deposition of chrome on the LSCF surface is $SrCrO_4$. Since the deposition of $SrCrO_4$ layers is observed on the LSCF surface, it can be assumed that its formation is thermodynamically preferred and constitutes a kinetically fast reaction step [37]. As already mentioned, SrO is considered to act as a precursor in the formation of $SrCrO_4$ and, thus, the segregation of mobile SrO-phases plays an important role in the deposition of Cr-species [21,38–42]. Assuming a chemically induced reaction between the mobile SrO-species and CrO_3, interaction of both would lead to the formation of intermediate Cr-Sr-O nuclei (9) followed by subsequent crystallization and grain growth of Cr_2O_3 and $SrCrO_4$ layers (10, 11) [21,30,43].

Nuclei Formation: $$CrO_{3(g)} + SrO_{(s)} \rightleftharpoons Cr - Sr - O_{(nuclei)(s)} \quad (9)$$

Cr_2O_3 Formation: $$Cr - Sr - O_{(nuclei)(s)} + CrO_{3(g)} \rightleftharpoons Cr_2O_{3(s)} \quad (10)$$

$SrCrO_4$ Formation: $$Cr - Sr - O_{(nuclei)(s)} + CrO_{3(g)} + SrO_{(s)} \rightleftharpoons SrCrO_{4(s)} \quad (11)$$

Nevertheless, a recently performed SOFC short-stack test (1300 h at 700 °C followed by 1200 h at 600 °C) at a constant current density of 0.5 A/cm² revealed the presence of $SrCrO_4$ on the LSCF surface as well as Cr-species at the LSCF/GDC interface using a thin-film 8YSZ electrolyte (prepared by sol-gel synthesis) and a physical vapor-deposited (PVD) diffusion barrier layer [5,3]. In comparison to current state-of-the-art cells equipped with screen-printed electrolytes (10 µm) and diffusion barrier layers (5 µm), all cells in this short-stack only comprised of 2 µm of ion conducting layers (1 µm 8YSZ + 1 µm GDC). Another study of a four-layer Jülich F-design short-stack revealed the presence of Sr- and Cr-containing crystals on the LSCF surface and small Cr-deposits at the LSCF/GDC interface after operation of 1240 h at 700 °C (240 h operated at a current density of 0.5 A.cm^{-2} and 1000 h at 0.75 A.cm^{-2}). Beez et al. [3] explained their experimental findings by a strong CrO_3 and O_2 partial pressure dependency of the reaction between gaseous Cr-species and SrO. The group pointed out that sufficiently high partial pressures of both species lead to the formation of $SrCrO_4$ whereas a deposition of Cr-species at the LSCF/GDC interface can be even triggered at very low oxygen partial pressures, which are induced by the current flow (see Figure 3.3). As these effects were not observed in previous state-of-the-art stack-tests at 0.5 A.cm^{-2}, the interplay between a higher current density (0.75 A.cm^{-2}), combined with an adequate

operating temperature and appropriate CrO_3/O_2 partial pressures, strongly influences the Cr-poisoning behavior of those cells.

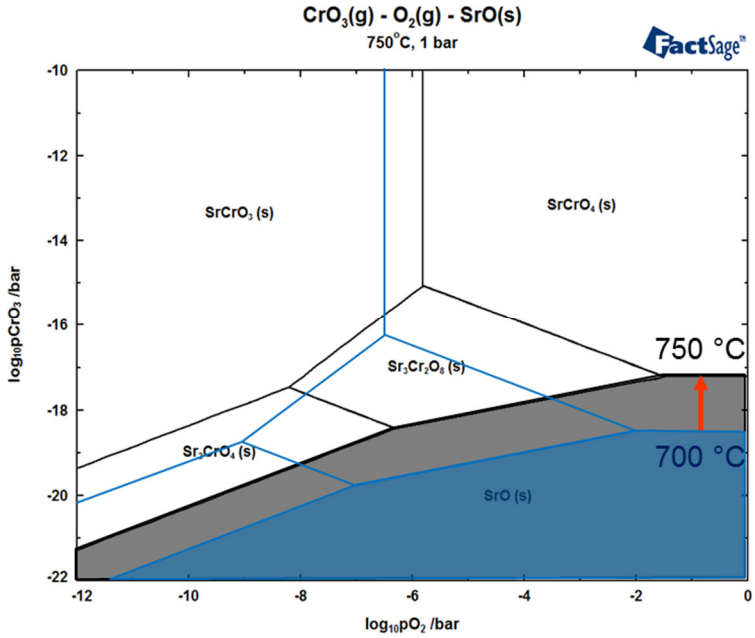

Figure 3.3: : $CrO_3(g)$-$O_2(g)$-$SrO_{(g)}$ phase-diagram at 1 bar incl. temperature shift from 700 °C to 750 °C [3].

These findings indicate a far more complex Cr-related degradation behavior of LSCF-based systems than predicted by nucleation theory [3] and can be considered as motivation to perform an in-depth analysis of the Cr-poisoning behavior of non-manganiferous SOFC cathode materials. Based on previous findings, it has been mainly focused on the interplay between temperature, current density (overpotential), humidity and cathode composition.

3.3. Electrochemical Basics

As already mentioned in previous chapters, SOFCs rely on the electrochemical reduction of O_2 and the oxidation of a combustion gas such as H_2 or CH_4. To describe the influence of chrome on the system and identify related degradation processes, extensive knowledge of its electrochemical behavior under open circuit voltage as well as polarization is of critical importance.

3.3.1. Open Cell Voltage (OCV)

The redox reaction in SOFCs which are not connected to a consumer (i.e. open circuit) is taking place until an electrochemical equilibrium state is reached [44,45]. Under open circuit conditions, electrons cannot be transported from the anode to the cathode side, leading to a charge separation which induces an electric field force oppositely directed to the driving force of the reaction. In equilibrium, both forces show the same order of magnitude so that O^{2-}-ion migration through the electrolyte is prevented. This state is called Open Cell Voltage (OCV) or Open Cell Potential (OCP) and is described by the Nernst equation (12) [12]:

1. Nernst Equation: $$U_N = \frac{RT}{zF} \ln \sqrt{\frac{pO_{2,cat}}{pO_{2,an}}} \quad , \tag{12}$$

where U_N is the Nernst voltage, R the gas constant, T the absolute temperature, z the number of transferred electrons within the SOFC reaction, F the Faraday constant and pO_2 the oxygen partial pressure at cathode and anode. With the utilization of compressed air, the oxygen partial pressure on the cathode side can be set as $pO_{2,cat}$ = 0.21 atm. However, the anode partial pressure $pO_{2,an}$ has to be indirectly determined with help of the law of mass action (K_p, equilibrium constant) and the H_2O and H_2 partial pressure on the anode side (13). As the partial pressure and, thus, also the equilibrium constant are temperature dependent, they can be related to the change of the Gibbs free energy ΔG^0 (14) [8].

Law of Mass Action: $$K_p \left[\frac{1}{\sqrt{atm}}\right] = \frac{pH_2O_{an}}{pH_{2,an}\sqrt{pO_{2,an}}} \tag{13}$$

Gibbs Free Energy: $$K_p = \exp\left\{-\frac{\Delta G^0}{RT}\right\} \tag{14}$$

With knowledge of the standard electrode potential E^0 (15), the alternative notation for the Nernst potential can be written as shown in (16) [8].

Standard electrode potential: $$E^0 = -\frac{\Delta G^0}{zF} \tag{15}$$

2. Nernst Equation: $$U_N = E^0 + \frac{RT}{zF} \ln \frac{\sqrt{pO_{2,cat}}\, pH_{2,an}}{pH_2O_{an}} \tag{16}$$

3.3.2. Polarization Processes

The Nernst potential describes the theoretical potential of a fuel cell such as a SOFC. Nevertheless, the addition of a consumer to the external circuit forces the cell to perform work. Here, the theoretically achievable cell potential is limited by various sorts of loss processes. These polarization processes have to be subtracted from the Nernst potential to determine the current-dependent cell potential (17) [8].

Cell Potential (Closed Circuit):

$$U(I) = OCV - \eta_{ohm} - \left|\eta_{gas}\right|_{an,cat} - \left|\eta_{act}\right|_{an,cat} - \left|\eta_{conc}\right|_{an,cat}, \tag{17}$$

where η_{ohm} is the ohmic polarization, $\left|\eta_{gas}\right|_{an,cat}$ the gas polarization, $\left|\eta_{act}\right|_{an,cat}$ the activation polarization and $\left|\eta_{conc}\right|_{an,cat}$ the concentration or diffusion polarization of anode and cathode, respectively.

Ohmic polarization:

Ohmic polarization losses are induced by the transport of ions and/or electrons through the electrode structures or the 8YSZ electrolyte [12,46]. The main contribution to the ohmic polarization is provided by the electrolyte. In planar anode-supported solid oxide fuel cells, the electrolyte thickness ranges from 10-20 µm such that the ohmic resistance contribution

can be estimated to a value of 0.020 Ωcm^2 at 800 °C or 0.176 Ωcm^2 at 600 °C, respectively (ionic conductivity of 8YSZ at 800 °C= 5 S.m^{-1}) [47]. By utilization of mixed ionic-electronic conductors (MIECs) such as LSCF or LSC [48] and an additional diffusion barrier layer, also the ohmic resistance increases, leading to reduced cell performances. However, without a DBL, less conductive Sr_2ZrO_4 would be formed [49,50] which would lead to an even stronger increase of the ohmic resistance. In general, the ohmic overpotential (η_{ohm}) can be described as the sum of all ohmic contributions in linear relation to the current density (18) [12].

Ohmic -Overpotential: $$\eta_{ohm} = j \sum_n R_n \quad (18)$$

Gas polarization:

The gas polarization or gas conversion loss is caused by high current densities that induce high fuel and air consumption. The concentration of both gasses is decreased while the production of H_2O on the anode side is increased. As a consequence, an increased oxygen concentration in the anode room leads to a decreased partial pressure difference between both electrodes and a reduced driving force of the reaction.

Activation polarization:

In order to initialize the redox reaction of SOFCs, a certain energy barrier has to be exceeded. Therefore, an activation energy is needed, as otherwise, no (spontaneous) reaction would be initiated. These activation losses mainly occur at the triple phase boundary where electrode, electrolyte and gas-phase are in direct contact with each other. In case of MIEC cathode materials like LSCF, the triple-phase boundary expands over the entire electrode. Due to that, also the process of activation polarization can take place over the entire electrode. From a thermodynamical point of view, the activation polarization and thus the applied overpotentials can be reduced with increasing temperature. The Butler-Volmer equation, generalized for multi-electrodes, describes the relation between current density and activation polarization and is shown in (19) [44,51,52].

Butler-Volmer: $$j = j_{o,el}\left[\exp\left(\alpha_{el}\frac{z_e F \eta_{act,el}}{RT}\right) - exp\left(-\langle 1-\alpha_{el}\rangle \frac{z_e F \eta_{act,el}}{RT}\right)\right], \quad (19)$$

where $j_{0,el}$ is the exchange current density between electrode and electrolyte, α_{el} the charge transfer coefficient and $\eta_{act,el}$ the activation overpotential of the electrode.

Concentration polarization:

Concentration polarization or gas diffusion losses are correlated with undersupply of air or combustion gas at the triple-phase boundary of cathode and anode, respectively. Together with an undersupply at the anode, also the transportation of the reaction product (H_2O) is rate limiting. Physically, an enhanced gas conversion induced by high current densities can cause insufficient gas transport which triggers those losses. The mathematical description for the concentration overpotential can be derived from the modified Nernst-equations (20, 21) [53].

Pol. Overpot., Anode: $$\eta_{conc,an} = \frac{RT}{2F} \ln\left(\frac{pH_2O_{an}^{TPB}\, pH_{2,an}}{pH_2O_{an}\, pH_{2,an}^{TPB}}\right) \quad (20)$$

Pol. Overpot., Cathode: $$\eta_{conc,cat} = \frac{RT}{4F} \ln\left(\frac{pO_{2,cat}}{pO_{2,cat}^{TPB}}\right), \quad (21)$$

where $\eta_{conc,an}$ and $\eta_{conc,cat}$ represent the concentration overpotential either at the anode or cathode, whereas $pH_{2,an}$, pH_2O_{an} and $pO_{2,cat}$ describe detectable partial pressures within the pores and atmospheres and $pH_2O_{an}^{TPB}$, $pH_{2,an}^{TPB}$ and $pO_{2,cat}^{TPB}$ are the non-detectable partial pressures. The latter have to be determined by implementation of Fick´s 1st-law. Here, linear concentration gradients (as a function of the current density) between atmosphere and triple-phase boundary are assumed (22, 23) [54].

Pol. Overpot. Adjusted, Anode: $$\eta_{conc,an} = \frac{RT}{2F} \ln\left(\frac{1 + \frac{R\,T\,L_{an}}{2\,F\,D_{H2O}^{eff}\, pH_2O_{an}\, P_0} j}{1 - \frac{R\,T\,L_{an}}{2\,F\,D_{H2}^{eff}\, pH_{2,an}\, P_0} j}\right) \quad (22)$$

Pol. Overpot. Adjusted, Cathode: $$\eta_{conc,cat} = \frac{RT}{4F} \ln\left(\frac{1}{1 - \frac{R\,T\,L_{cat}\,(1 - pO_{2,cat}\,I\,P)}{4\,F\,D_{O2}^{eff}\, p\,O_{2,cat}\, P_0} j}\right), \quad (23)$$

with L_{an} and L_{cat} being the diffusion layer thicknesses, D_{H2O}^{eff}, D_{H2}^{eff} and D_{O2}^{eff} as the molecular diffusion coefficients, P describing the absolute pressure as well as P_0, the pressure conversion factor (atm to Pa).

All mentioned processes provide individual contributions to the overall cell impedance. These contributions differ in their relevance depending on the operational parameters. In this PhD-thesis influences induced by changing the cell temperature, current density, humidity and the electrode material are investigated. Besides, the implementation of a specific Cr-poisoning procedure should provide information about possible poisoning mechanisms. With this knowledge Cr-poisoning promoting operational parameters should be identified and countermeasures should be established.

3.4. Electrochemical Characterization

The electrochemical in-operando characterization is the most powerful tool to interpret the influence of Cr poisoning in combination with variable operational parameters. Whereas other characterization methods (e.g. microscopic investigations) describe a pre- or post-test moment of the characterized cell condition, electrochemical in-operando methods provide continuous information about the cell. Furthermore, solely electrochemical characterization methods describe the cell behavior under realistic conditions such as the operating temperature or applied overpotentials. In the following chapters, essential direct current (DC) and alternating current (AC) methods are presented and explained.

3.4.1. *I/V-Characterization*

The Current/Voltage-characterization is the standard procedure to evaluate the performance of an electrochemically active SOFC. This DC-method describes the correlation between voltage and current by stepwise reduction of the potential, from OCV to a previously defined value (e.g. 0.6 V). Figure 3.4 depicts a corresponding SOFC performance curve and identifies the most interesting regimes. The diminished realistic OCV-value can be explained by the occurrence of small gas and electron leakages, resulting in unwanted fuel/air distribution. Furthermore, also loss processes as ohmic polarization, gas polarization, activation polarization and concentration polarization as well as their occurrence in the I/V-curve are depicted. From a general electrochemical point of view, the latter processes are referred to as polarization losses as they all show a strong dependence on the applied current density.

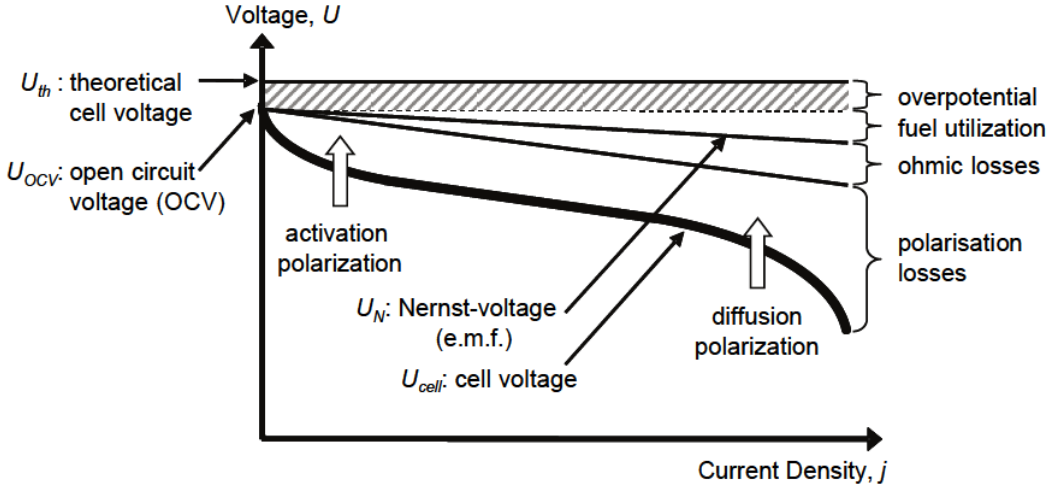

Figure 3.4: Characteristic I/V-plot of a high temperature SOFC incl. identification of the loss processes [6,12,55] .

3.4.2. *Electrochemical Impedance Spectroscopy (EIS)*

In contrast to performance assessing DC-methods, such as the I/V-characterization, the electrochemical impedance spectroscopy (EIS) has the capability of identifying loss processes and their individual contributions to the complex cell chemistry of a SOFC. Here, the individual time and frequency dependence of each polarization process helps to analyze the behavior of a SOFC system as well as a single cell. By applying an AC-signal (potentiostatic or galvanostatic) at selected frequencies in a defined frequency range, it is possible to measure the responding phase shift and amplitude of the obtained current or voltage, respectively. In detail, a sinusoidal shaped current/voltage signal with a small amplitude is superimposed to a previously defined DC signal. The obtained sinusoidal phase-shifted current/voltage response can then be measured and the overall cell impedance calculated, as shown in (24) [12].

Complex Impedance:

$$Z^*(\omega) = \frac{u(t)}{i(t)} = \frac{u_0(\omega)}{i_0}\, e^{j\varphi(\omega)} = |Z(\omega)|\, e^{j\varphi(\omega)} = Re\{Z^*(\omega)\} + jIm\{Z^*(\omega)\}, \quad (24)$$

where ω is the angular frequency and $\varphi(\omega)$ the angular frequency dependent phase shift between the input and response signal.

As shown in (24), the overall cell impedance is defined by the sum of a real $Re\{Z^*(\omega)\}$ and an imaginary contribution $jIm\{Z^*(\omega)\}$. The resulting curve can be depicted in a complex plane also referred to as Nyquist-plot [12,51,56]. Here, the first intercept with the x-axis (high-frequency regime) represents the pure ohmic resistance whereas the second intercept (low-frequency regime) is the total resistance (slope of the I/V-curve at the operational points). The range between both points is defined as the polarization resistance which contains all information about the individual polarization losses of the SOFC ($R_{total} - R_{ohm} = R_{pol}$).
To successfully interpret the individual electrochemical behavior of each cell, certain boundary criteria have to be fulfilled. These criteria include a stable, linearly responding, and causal system. More precisely, the system should not suffer from increasing system perturbations and respond linearly to a defined perturbation signal without preceding it [51]. Finally, the so-called Kramers-Kronig relations (KK-relations) can be used to verify the measured data regarding their suitability to be further evaluated. Here, it should be possible to calculate the imaginary part of the impedance with help of the real part and vice versa.

3.4.3. Equivalent Circuit Model

In order to interpret impedances and identify individual loss processes and their contributions to the overall cell impedance, equivalent circuit models can be used. To establish a suitable model that helps to explain the cell electrochemistry, different elements such as resistors, capacitors and inductors (etc.) have to be combined. Depending on the complexity of the cell electrochemistry, also the equivalent circuit model has to be a complex description. In the following, several elements will be discussed that are essential to understand the utilized EC-model within this work.

RQ Element:

The problem with analyzing EIS-data is that they often cannot be adequately explained by ideal circuit elements. As an example, a pure capacitor (C) can be mentioned which has a single well-defined resonance frequency, suitable for the description of an ideal system. However, a real non-ideal system shows a distribution of relaxation times that are not considered within an ideal element. This leads to inadequate approximations of distributed impedances by usage of a finite number of elements [56,57]. In case of SOFCs, the actual 3-dimensional electrode structure differs strongly from the 2-dimensional microstructure of an ideal capacitor leading to a non-ideally distributed behavior [12]. To describe this non-ideal RC-like behavior, a distributed RQ impedance element (Q = Constant phase element) is used and can be defined as (25) [12,56,57].

RQ Element: $$Z_{RQ}(\omega) = \frac{R}{1+RQ^{-1}} \quad (25)$$

The resulting time constant and frequency are defined as (26, 27):

Time Constant, RQ: $$\tau_{RQ} = \sqrt[n_Q]{(RY_Q)} \quad (26)$$

Frequency, RQ: $$f_{max,RQ} = \frac{1}{2\pi\tau_{RQ}} = \frac{1}{2\pi\sqrt[n_Q]{RY_Q}} \quad (27)$$

With decreasing the value of $n_Q < 1$, the semicircle is pivoted around the high frequency intercepts which represents most realistic systems. In the case of $n_Q = 1$, the semicircle can be explained by a parallel RC element with a perfect capacitor, whereas $n_Q = 0$ would lead to a pure resistive behavior (R).

Gerischer Element (G):

Several studies showed that with the utilization of a porous MIEC as LSCF, larger contributions from O^{2-}-ion diffusion and O_2 surface exchange kinetics to the overall cell impedance can be detected [12,58]. For the coupling of both processes the Gerischer impedance $Z_G(\omega)$ has been derived (28) [12,59,60].

Gerischer Impedance: $$Z_G(\omega) = \frac{R_{chem}}{\sqrt{1 + j\omega t_{chem}}}, \quad (28)$$

with R_{chem} and t_{chem} representing resistance and time constants that are related to the individual properties of MIECs (eq. porosity, active surface area, concentration of oxygen vacancies etc.).

Finite Warburg Element (Ws)

The last mentionable complex circuit element helping to understand the complex electrochemistry of SOFCs is the finite Warburg element. This element is used to describe finite-length diffusion and transmissive boundary conditions (e.g. gas diffusion losses). In SOFC technologies, these losses are often related to the thick anode substrate. In (29), the finite Warburg element and in (30) the Warburg coefficient are described as follows [12,56,57,61].

Finite Warburg Impedance: $$Z_{W_s}(\omega) = R_W \frac{\tanh[(j\omega T_w)^{n_W}]}{(j\omega T_w)^{n_W}}, \quad (29)$$

Warburg Coefficient: $$T_w = \frac{L_d^2}{D_L^{eff}} \quad (30)$$

where, ideally, n_W goes to 0.5, R_W is the diffusion resistance and T_w is related to L_d^2/D_L^{eff} (L_d is the effective diffusion thickness; D_L^{eff} is the effective diffusion coefficient).

Initial EC-Model

Figure 3.5 shows the experimentally determined equivalent circuit model for the description of the related physico-chemical processes of an anode-supported SOFC. Apart from a serial resistor (ohmic resistance), the model, first developed by the group of Ivers-Tiffée, describes three anode and two cathode processes [60,62,63].

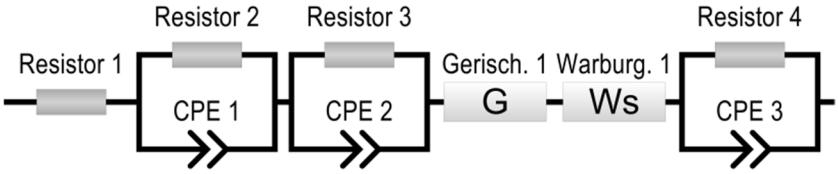

Figure 3.5: Starting point for the adjustment of an adequate EC-model for the description of the physico-chemical processes in an anode-supported SOFC with a LSCF-cathode [60,62,63].

The high-frequency processes denoted as R2/CPE1 and R3/CPE2 can be assigned to the reaction at the triple-phase boundary and to the charge transfer reaction (activation polarization) [62,63] By varying the oxygen partial pressure at the cathode (21 % - 1 %), cathodic contributions were pronounced and the group showed an evolving process (here denoted as R4/CPE3) at very low oxygen partial pressures in the low frequency range (< 10 Hz). Simultaneously, they observed the appearance of a second process between 100 Hz – 10 Hz (G1) that strongly overlaps the process described with Ws1. However, the processes R2/CPE1, R3/CPE2 and Ws1 are not directly affected by the oxygen content at the cathode. Thus, these processes can be mainly related to the anode whereas G1 and R4/CPE3 are assigned to the cathode.

The group associated the process G1 with the oxygen surface exchange kinetics as well as the oxygen diffusivity through the bulk of LSCF-cathode materials and R4/CPE3 with the mass-transfer resistance (caused by gas diffusion within the LSCF pores) [59,62]. Furthermore, a strong dependence of the anodic water partial pressure together with a negligible thermal activation energy could be related to the process Ws1 [53,62]. As a result, the group related anode-sided gas diffusion processes with Ws1 (Table 1).

Table 1: ***Physicochemical processes identification in an anode-supported SOFC with LSCF cathodes*** [60,62,63]

Element	Frequency, ASR	Parameters	Physicochemical Process
R4/CPE3	0.3 – 10 Hz 2 -100 mΩcm^2	pO_2 (low) Temperature	Gas diffusion in the cathode structure
Ws1	4 – 20 Hz 30 – 150 mΩcm^2	pH_2, pH_2O Temperature (low)	Gas diffusion in the anode structure
G1	10 – 500 Hz 8 – 50 mΩcm^2	pO_2 Temperature	Oxygen surface exchange kinetics O^{2-}-diffusivity in the cathode bulk
R3/CPE2	2 – 8 kHz 10 – 50 mΩcm^2	pH_2, pH_2O Temperature	Gas diffusion Charge transfer reaction Ionic transport in the anode functional layer
R2/CPE1	12 – 25 kHz 10 – 130 mΩcm^2	pH_2, pH_2O Temperature	

4. Experimental Methods

Within the next chapters, several different experimental methods ranging from the production of appropriate electrolyte supported half cells, over the setup installation and electrochemical characterization of all cell types in presence/absence of a Cr-Source, up to various pre-and post-test characterization methods, are presented.

4.1. Powder Synthesis

In a first step, various cathode powders are synthesized to investigate the influence of different B-site stoichiometries on the electrochemical behavior of ESCs in presence/absence of a Cr-source. Since LSCF ($La_{0.58}Sr_{0.6}Co_{0.2}Fe_{0.8}O_{3-\delta}$) currently serves as the benchmark and standard cathode material in SOFC-applications, knowledge of B-site variations should be expanded by additional investigation of LSF ($La_{0.58}Sr_{0.6}FeO_{3-\delta}$) and LSC ($La_{0.58}Sr_{0.6}CoO_{3-\delta}$) cathode materials.

In order to use the solid-state synthesis procedure, the precursor powders La_2O_3, $SrCO_3$ a mixture of CoO/Co_2O_3 and Fe_2O_3 (Sigma-Aldrich and VWR International) are used. In an initial step, the powders are mixed (together with isopropanol) in desired stoichiometric ratios and transferred into a milling container. Additionally, spherical ZrO_2 milling balls with diameters of 2 mm and 10 mm are added to serve as milling agents. The filled milling containers are then placed inside a planetary ball mill, and the rotation speed is set to 4000 rpm for a time period of 4 h. Subsequent to the milling procedure, the respective powders are separated from any ZrO_2 balls, transferred into a flask and mounted into a rotary evaporator for further removal of isopropanol residuals. This procedure is followed by a 48 h drying period of all mixed powders under ambient conditions. In a final step, the dried powders are placed into a commercially available furnace and calcinated for 3 h at 1080 °C.

To reach an adequate cathode particle size distribution (PSD) of the synthesized materials, further milling steps are implemented. Therefore, the calcinated cathode powders are processed again with help of the planetary ball mill (incl. isopropanol and 2 mm ZrO_2 milling balls) until a size distribution of about 2 µm is reached.

4.2. Paste Production

The production of suitable pastes is of great importance to enable the screen printing procedure and thus guarantee an optimal and cost-efficient deposition of the synthesized cathode materials. In a first step, the respective LSF, LSCF and LSC cathode powders are mixed with a binder which comprises of 94 % terpineol and 6 % ethyl-cellulose, in a 1:1 weight ratio. By subsequent use of a vacuum high energy planetary mill, it is possible to ensure a homogenous distribution of the cathode material within the complete paste. Furthermore, to prevent the formation of larger agglomerates and thus an increase of the PSD, all pastes are post-treated with a three-roll mill. The distance of the inner and outer rolls is gradually reduced from 1 µm down to 0.1 µm, resulting in pastes that are suitable for screen printing.

4.3. Cathode Deposition

By using the low-cost and semi-automatic screen printing procedure, it is possible to deposit highly reproducible smooth and homogenously distributed cathode films in the order of several micrometers. It is known as a reproducible procedure to produce thick layers and, thus, is preferred within industrial applications as well as the production of SOFC single-cells [64]. A typical screen printer, such as the EKRA E-1 (EKRA Automatisierungssysteme GmbH), consists of three main components, namely: an adjustable table (sample holder), a printing chamber and a suitable printing screen. The latter is fixed within the sample chamber. First, a custom-tailored sample mask is placed on top of the adjustable table to ensure a consistent orientation of each cell during the printing procedure, enabling the reproducible production of symmetric cells. By moving the sample holder close to the printing screen, sample and print area can be aligned with each other. As the cathode paste is printed through the printing area using vertically moving squeegees that apply a defined pressure onto the screen, a rebound height between screen and adjustable table is set to a value of 1.5 mm. Furthermore, the height of both squeegees is set to a value of 2.5 mm below the installed screen, thus defining the applied pressure. In a last step, the synthesized pastes are applied on top of the printing screen, directly above the printing area, and the semi-automated print program is started (Table 2).

Table 2: ***Screen printing parameters***

Screen	Material	Polyester (Pol)
	Screen Size (Open-size)	0.7854 cm² (39 %)
	Mesh size	417 µm
	Fabric thickness	425 µm
	Threat diameter	250 µm
	Threats per cm	15
	Wet layer thickness	165 $cm^3 \cdot m^{-2}$
Printing process (Device specific units)	Velocity (squeegees)	110
	Pressure (squeegee, back)	460
	Pressure (squeegee, front)	140
	Pressure option	3A
	Separation velocity	0.4

4.4. Cell Portfolio

Several research groups in the field of electrochemical characterization of SOFCs state minor contributions of cathode processes to the overall cell electrochemistry/impedance as compared to those of the anode. In order to completely understand the cathode attributed Cr-poisoning procedure, anode-supported full-cells as well as symmetrical electrolyte-supported half-cells are used. Here, full-cells help to describe the influence of Cr-deposition on the complete system whereas symmetrical half-cells identify cathode contributions and their behavior towards Cr-poisoning.

For this purpose, commercially available ASCs (Co.: CeramTec GmbH) with multilayered $La_{0.58}Sr_{0.4}Co_{0.2}Fe_{0.8}O_{3-\delta}$-cathode (LSCF), a CGO-diffusion barrier, an 8YSZ-electrolyte and a multilayered Ni/8YSZ anode serve as state-of-the-art standard cells (Figure 4.1A). On the other hand, electrolyte supported half-cell substrates (8YSZ electrolyte incl. CGO-diffusion barrier on both sides, Co.: Kerafol GmbH) are symmetrically equipped with various cathode materials (Figure 4.1B, additional information about the procedure are given in 5.2.1).

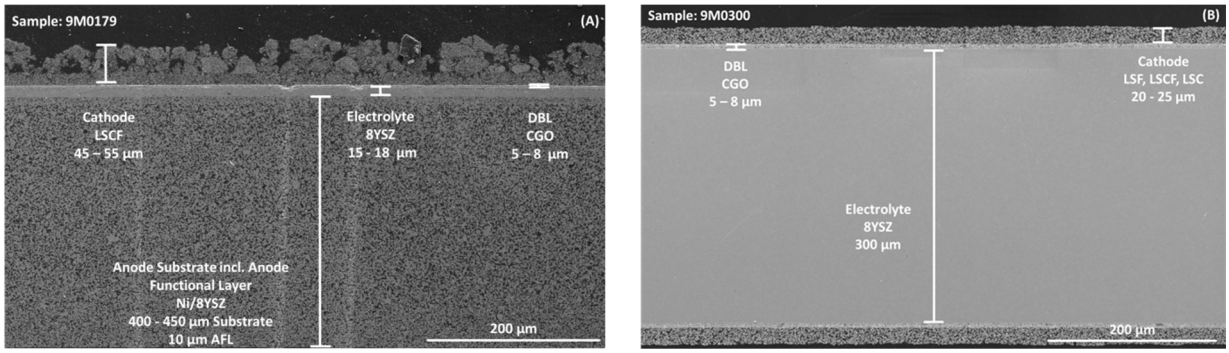

Figure 4.1: Cross-sections auf (A) anode-supported SOFCs (full-cells) and (B) symmetrical, electrolyte supported SOFCs (half-cells).

4.5. Electrochemical Measuring Setups

The most important characterization procedures to analyze the electrochemical behavior of SOFCs in presence/absence of suitable Cr-sources are DC and AC related methods, such as current/voltage characteristics or impedance spectroscopy. Both, commercially available anode-supported SOFCs (ASCs, single-cells) and customized electrolyte supported SOFCs (ESCs, half-cells), can be characterized by their electrochemical performances using 2-/3-electrode measuring setups.

4.5.1. 2-Electrode Setup

The used 2-electrode measuring technique enables the electrochemical performance characterization of anode-supported single-cells (full-cells) by means of current/voltage-characteristics (I/V-, DC-method) and resistance/capacitance analysis (impedance spectroscopy, AC method). For DC methods, a specific current is applied to receive a voltage-based response from the system. For AC methods, a sinusoidal signal with a defined excitation amplitude over a wide range of frequencies is applied and the corresponding, phase-shifted response of the whole system is obtained. Therefore, working and sense electrodes (WE & S) are connected to the cathode whereas the counter and reference electrode (CE & R) are attached to the anode (Figure 4.2). It is measured with and without Cr-sources (uncoated and preoxidized Crofer 22 H metal sheets) to ensure a clear identification of chrome related and other degradation processes. If a Cr-source is utilized, it is placed beneath the inner/lower current collector to avoid any contact to the cathode material and ensure realistic gas-phase reactions. Furthermore, the incoming air is led through small holes within the Cr-source to provide a steady Cr-partial pressure inside the sample chamber.

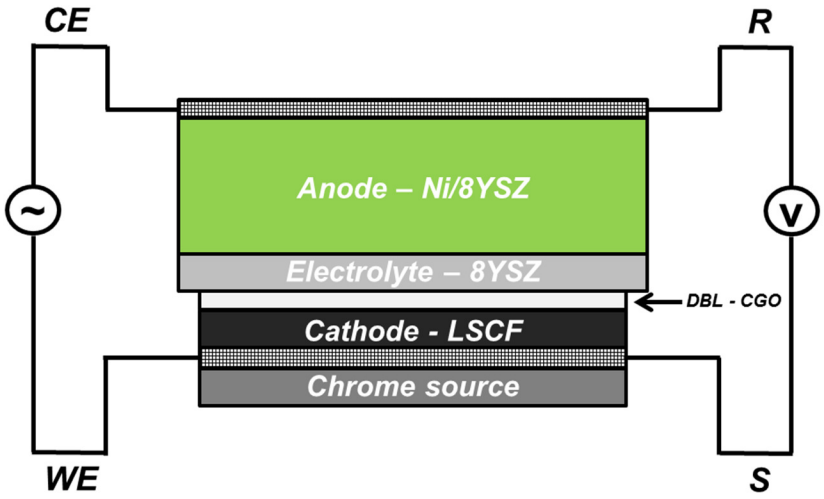

Figure 4.2: 2-electrode setup: Contact scheme of an ASC (full-cell).

The schematic in Figure 4.3 shows the sample chamber inside of the ceramic housing (left) and a profile of the sample holder (right). The ASC including a gold sealing (3) is mounted on top of a Pt-current collector (inner collector, 4) which is either placed on the Cr-source (5) or directly located above the air inlet (6). The ASC, is connected with a Ni/Pt-current collector (2), which connects the anode substrate to the external circuit. Furthermore, an inner thermocouple is placed in close proximity to the cell in the cathode chamber. The complete sample holder is fixed by a spring-loaded lock (1 and 7), which simultaneously prevents a contact loss between the components. Additionally, two outer thermocouples as well as the combustion gas inlet (glass tube) are installed.

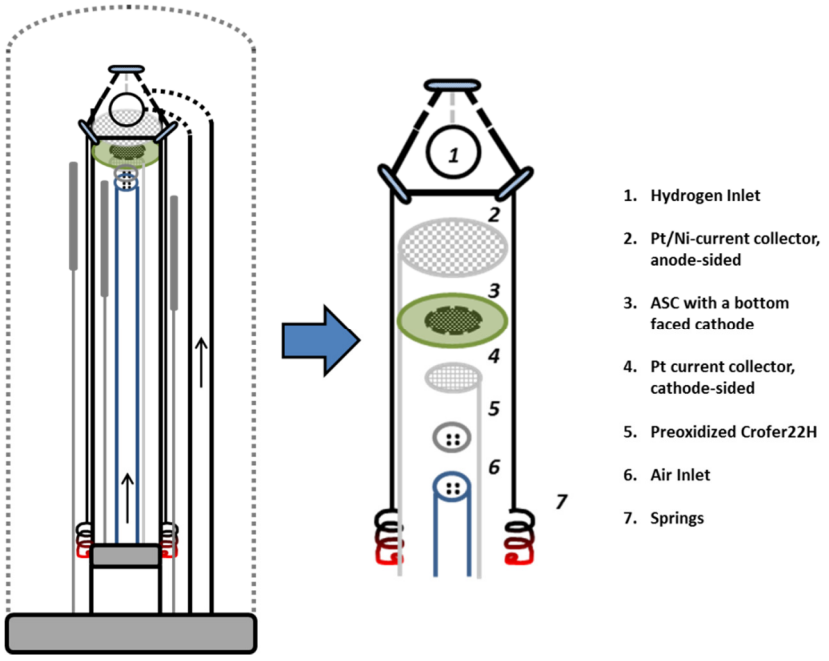

Figure 4.3: 2-electrode setup: Sample holder scheme incl. Crofer 22 H Cr-source.

The complete setup (incl. ceramic housing and all electronic ports, namely Probostat) is transferred into a semi-automatic test-rig (Co.: EBZ GmbH) and a tube furnace

(Co.: Carbolite GmbH), respectively. The test-rig can be supplied with hydrogen, safety-gas (4 % H_2 in N_2) and nitrogen at the anode side as well as air and pure oxygen at the cathode side (all from externally stored gas-bottles). Here, the gas-flow is controlled with mass-flow controllers (Co.: Burkert GmbH). Furthermore, both sides (incl. all gases) can be humidified with help of an electrically heated gas-humidifier (Co.: EBZ GmbH). Before closing the furnace, the ceramic housing is equipped with a metal grid (faradaic cage) to shield the measurement signals from electrochemical disturbances induced by external sources.
Table 3 gives an overview of the most important method parameters.

Table 3: ***2-electrode setup: Measuring parameters***

Cell type	Anode-supported SOFC, full-cell (Ø 20 mm, CeramTec)
Cathode	LSCF (Ø 10 mm)
Cr-source	Crofer 22 H (uncoated and preoxidized)
Temperature	950 °C-650 °C (Steps: 50 °C)
Anode-gas	H_2 (9 Nl/h)
Cathode-gas	Air (14 Nl/h)
Frequencies	110 kHz-1 mHz
Excitation amplitude	20 mA·cm^{-2}

To ensure reliable and reproducible results of anode-supported SOFCs (full-cells), each of the measurements is conducted according to a previously defined measuring schedule (Figure 4.4). In a first step after installation, the samples are heated up to 900 °C (955 °C furnace temperature) only provided with compressed air (cathode) and nitrogen (anode). Afterwards, with stepwise introduction of H_2 into the reaction chamber, it is possible to reduce the NiO-anode to elemental Ni. This is followed by 48 h periods at, either, open cell conditions (I), or under continuous loads of 0.5 A.cm^{-2} (II), 0.75 A.cm^{-2} (III) and 1 A.cm^{-2} (IV). Beside initial DC and AC tests, potentiostatic impedance measurements (1.0 V and 0.7 V) are conducted, each 24 h (0 h, 24 h and 48 h), within the individual periods (I-IV). At the end of each period, additional I/V-characterizations as well as impedance potential scans are performed. Here, for each potential between OCV and 0.6 V (Steps: 50 mV) an impedance curve is measured. In order to investigate the influence of humidity on the cell-degradation, all measurements are repeated with an air humidity of 3.5 %. As a next step, a new structurally identical cell is installed together with a Crofer 22 H Cr-Source, followed by a repetition of all conducted measurements. This procedure is performed for temperatures ranging from 900 °C to 650 °C in steps of 50 °C.

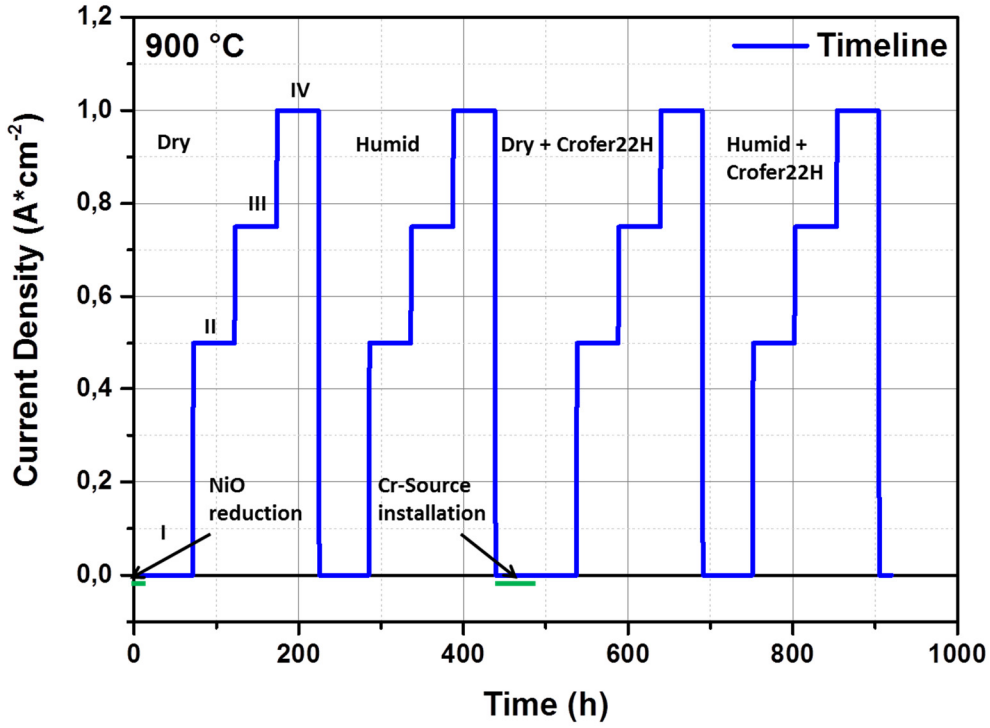

Figure 4.4: Measurement schedule for anode-supported SOFCs (full-cells) in presence and absence of a Crofer 22 H Cr-source.

4.5.2. 3-Electrode Setup

Both of the utilized 3-electrode setups are completely custom-built electrochemical measuring devices that differ from the commercially available 2-electrode setups in terms of housing, ceramic inlay, utilized cells, gas atmosphere, measuring technique and measuring method. The main advantage of using a 3-electrode setup and thus measuring the potential between the working electrode (WE) and a reference electrode (R) of a symmetrical cell is the exclusion of any physicochemical contribution of the counter electrode (CE) to the overall cell impedance. This is a strong advantage as applied overpotentials within a symmetrical setup would lead to an undesired anodic behavior of the LSCF counter electrode and, thus, to indefinable contributions. As the goal of this thesis is to identify chrome related cathode degradation processes and separate those from any anode processes, solely symmetrical, electrolyte-supported half-cells are measured (against a Pt-reference, Figure 4.5).

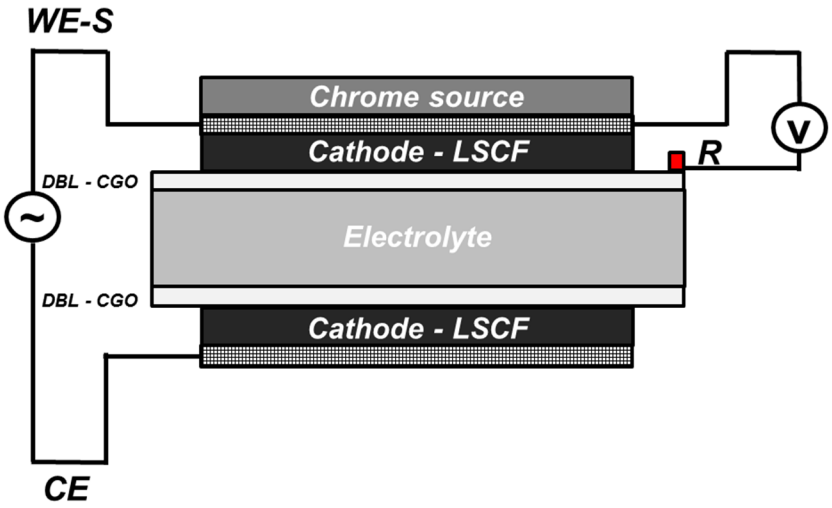

Figure 4.5: 3-electrode setup: Contact scheme of a symmetrical ESC (half-cell).

Figure 4.6 represents a schematic drawing of both identic measuring devices (MP09 and MP10). Both setups can be supplied with either dry or humid air. The air humidity level can be freely adjusted by passing air through a heated water filled round-bottom flask, as the water uptake (or gas-phase saturation pressure) is defined by the temperature of the cooler which is mounted on top of the flask. The gases can be transferred into the sample chamber to provide a consistent gas atmosphere. With help of a ceramic housing, the inner sample room and the furnace can be separated, leading to a reduced volume. Additionally, a ceramic housing can lead to more consistent gas atmospheres including a sufficient control of their humidity level. The sample chamber of each measuring device is equipped with two sample holders. This offers the possibility to install and measure two different, electronically completely separated samples at the same time (e.g. equipped with different cathodes). As shown in Figure 4.6, each sample holder consists of a ceramic base plate, the cell to be measured, another ceramic plate on top of the sample as well as a heavy single metal plate. The high weight of the metal plate and, thus, a strong applied vertical pressure, allows for an ideal contact between both current collectors and the adjacent functional cathode layers. In order to investigate the chrome related degradation behavior of those cells, an additional preoxidized Crofer 22 H Cr-source is embedded between the upper ceramic base plate and current collector (MP09). No Cr-sources are installed for the setups in MP10 such that appearing degradation tendencies cannot be related to any Cr-poisoning mechanism.
Further important measurement parameters are shown in Table 4.

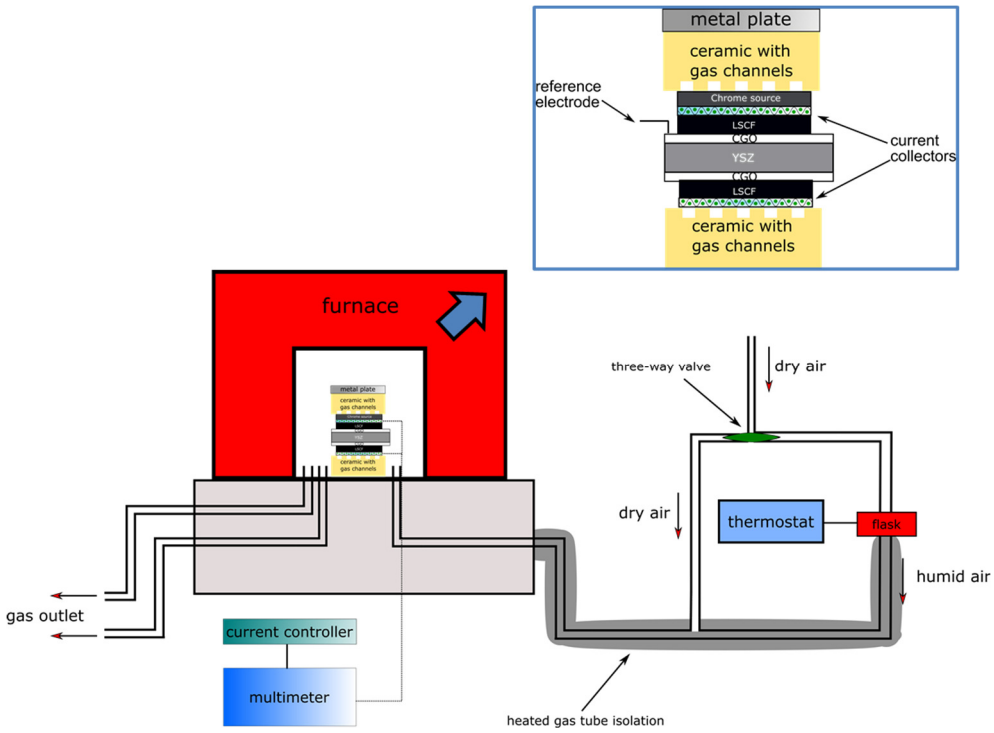

Figure 4.6: 3-electrode setup: Custom-built test-rig scheme incl. Crofer 22 H Cr-source.

Table 4: ***3-electrode setup: Measuring parameters***

Cell type	Symmetrical, electrolyte supported SOFC, half-cell (Ø 20 mm, Kerafol)
Cathode	LSCF, LSC, LSF (Ø 10 mm, FZJ)
Cr-source	Crofer 22 H (uncoated and preoxidized)
Temperature	900 °C
Anode gas	--
Cathode gas	Air (14 Nl/h)
Frequencies	110 kHz-1 mHz
Excitation amplitude	20 mA·cm^{-2}

The measurements for symmetrical electrolyte-supported SOFCs (half-cells) are conducted in accordance to the measurement schedule for anode-supported SOFCs (full-cells). In contrast to the measurement schedule for ASCs, no initial reduction step has to be performed since no NiO containing anodes are being utilized. Furthermore, the measurements are conducted at OCV, 0.75 A.cm^{-2}, 1 A.cm^{-2} and 2 A.cm^{-2} (no measurements at 0.5 A.cm^{-2}). Higher current densities (i.e. higher cathodic overpotentials) are assumed to lead to stronger Cr-poisoning effects which is advantageous during identification of these processes. However, all measurements are exclusively performed at 900 °C to ensure sufficient CrO_3 and/or $CrO_2(OH)_2$ partial pressures.

4.6. Pre- and Post-Test Characterization Methods

4.6.1. X-Ray Diffraction (XRD)

In order to identify the phase-purity and crystal structure of the synthesized powder materials, the X-ray diffractometer Empyrean (Co.: PANalytical) is used. Therefore, the powders are pressed into a sample holder, so that a homogenously distributed sample surface can be established. The sample-holder is then transferred into the diffractometer and measurements are performed in a range of 10 °-80 °.
The method uses X-rays, that are focused on the sample surface, so that, according to Bragg´s Law, the intensity of the scattered beam can be measured as a function of the incident angle and the wavelength (energy) [8,65]. The obtained pattern contains specific information of the crystal structure which can be compared to reference measurements from the ICSD-database [66]. As individual materials possess unique structures, a clear identification of each material is possible. Furthermore, also phase impurities can be interpreted, as they often lead to peak broadening effects, shoulder formations or simply to unidentifiable patterns.
The adjusted parameters for the XRD-measurements are shown in Table 5

Table 5: ***XRD parameters***

Radiation source	Cu Kα
Radiation wavelength	K_1 = 1540593 Å K_2 = 1544412 Å
Measuring range (2θ)	10 °– 80 °
Detector	Si-based detector (X_0Celerator)

4.6.2. Particle Size Distribution (PSD)

The particle size of the synthesized powders and pastes is determined to guarantee high porosities of the cathode materials and, thus, enable sufficient gas transport towards the electrodes as well as provide large electrochemically active areas. Therefore, the laser-scattering particle size distribution analyzer (Device: Partica-LA960, Co.: Horiba Scientific) is used. Small amounts (several mg) of the respective powders or pastes are suspended in either isopropanol or water and led through a laser beam. Thereby, the laser light is scattered in different angles towards a lens and focused onto a sensor. According to Fraunhofer diffraction theory, the particle size is directly proportional to the intensity of the scattered beam light but indirectly proportional to its angle. With this knowledge, it is possible to determine the median particle size and the overall particle size distribution of the analyzed powders and pastes.
The operational parameters are listed in Table 6.

Table 6: ***PSD parameters***

Laser source	LED (blue)
Measuring period	< 1 min
Measuring range	0.01 µm – 5000 µm
Measuring atmosphere	Liquid (wet)
Detector	5 x 4-channel detectors
Accuracy (relative standard deviation)	d_{10}-value: 3 % d_{50}-value 2.5 % d_{90}-value: 4 %
Reproducibility (relative standard deviation)	d_{10}-value: 5 % d_{50}-value 3 % d_{90}-value 5 %

4.6.3. Scanning Electron Microscopy (SEM)

The scanning electron microscope Quanta FEG 650 (Co.: FEI) is used for analysis of the synthesized cathode powders and pre-/post-test characterization of ASCs as well as ESCs. Within this work, the SEM procedure helps to understand the individual cathode composition/structure before operation, and the influence of Cr-deposition after operation. In order to analyze specimen cross-sections for pre-test characterization, the samples are cut, embedded into a resin, polished and sputtered with platinum. Furthermore, additionally attached Cu-tape helps to prevent charging of the sample surface. In case of top-views for post-test-characterization, the specimens are not embedded and simply equipped with a Cu-tape as they show sufficient electronic conductivities. By means of a heated Cu-Kα electron source, an electron beam is emitted, accelerated and focused (by magnetic coils) at the sample surface in ultra-high vacuum [67]. Here, the primary electrons from the focused electron beam can either backscatter (backscattered electrons, BSE) or react with the surface atoms under production of secondary electrons (SE). Whilst backscattering of highly energetic primary electrons (keV) strongly depends on the atomic number of the surface elements and thus represents the material contrast, less energetic secondary electrons (eV), originating from the first few nm of the sample surface, describe the topography [68]. Using both, SE and BSE for top-views and cross-sectional views of the specimen, helps to understand structural changes caused by electrocatalytic activity during cell operation as well as degradation due to Cr-poisoning.
A detailed description of the adjusted instrument parameters for SEM-analysis is shown in Table 7.

4.6.4. Energy-Dispersive X-Ray Spectroscopy (EDX)

Alongside the topographic analysis of the individual specimen, the EDX-detector "EDAX-Octan /Super SDD" is implemented inside the electron microscope. This procedure enables the analysis of the cathode composition and the distribution of each individual element within the microstructure. The removal of an electron from the inner electron shells of an atom, caused by the penetrating electron beam, leads to padding of these shells with electrons from higher orbitals. As electrons from higher orbitals possess more energy than

needed to refill these inner shells, excess energy in terms of characteristic X-rays is released [68]. These X-rays can be detected to perform a qualitative element analysis. Furthermore, the comparison of elemental peaks also allows for quantitative analysis of the sample composition [8]. A problem of the EDX-method to identify/quantify chrome deposits is presented by the overlap of the K_α X-ray peak of chrome with the L_β peak of lanthanum. Here, the ratio between the L_α and L_β of lanthanum can be compared to that of pure LSCF to confirm the presence of chrome deposits [21,27,28]. Since it is assumed that electrochemical and chemical Cr-poisoning mechanisms lead to the appearance of Cr-species at different locations within the cathode material (cathode surface and triple-phase boundary), an element mapping of the entirely imaged cathode layer is performed.
Table 7 shows the most important EDX-parameters.

Table 7: ***SEM- & EDX parameters***

SEM	Electron source	Cu_Kα
	Acceleration voltage	5 kV
	Working distance	10 mm
	Measuring atmosphere	$< 10^{-11}$ bar (UHV)
	Detector	ETD
EDX	Detector	SDD
	Dector-size	60 mm²

4.6.5. Inductively Coupled Plasma Optical Emission Spectrometry (ICP-OES)

The inductively coupled plasma optical emission spectrometry is a sub-genre of the group of optical emission spectrometry and enables the qualitative and quantitative detection of chrome within the system. In a first step to determine the Cr-content, the SOFC-sample to be measured is dissolved in 3 ml concentrated $HClO_4$ [69], heated until the solution starts to smoke and hold at the respective temperature for 1 h. This procedure is repeated twice. Afterwards, both residuals are combined and mixed with $HClO_4$ to a volume of 50 ml. In order to perform a double determination, two aliquots are taken from the solution and once again diluted to a mixture of 1:20 (Solution: $HClO_4$). In a last step, both solutions are transferred into an argon plasma (Device: iCAP6500 and 7600 Duo; Co.: Thermofisher Scientific) (~ 10000 K) and the resulting characteristic electromagnetic radiation is analyzed regarding the elements lanthanum (La), strontium (Sr), cobalt (Co), iron (Fe) and chrome (Cr).
Further information can be found in Table 8

Table 8: ***ICP-OES parameters***

Atomizer	Burgener Peek MiraMist Nebulizer
Spray Chamber	Cyclone spray-chamber
Measurement wavelengths (nm)	
Iron (Fe)	259.940, 238.204, 239.562, 261.187, 259.837, 240.488
Lanthanum (La)	412.323, 333.749, 379.478, 419.655, 261.034, 469.250
Strontium (Sr)	407.771, 421.552, 346.446, 216.596, 215.284, 228.200
Chrome (Cr)	283.563, 284.325, 267.716, 357.869, 359.349, 360.533
Cobalt (Co)	238.892, 228.616, 237.862, 230.786, 231.160, 235.342

4.6.6. X-Ray Photoelectron Spectroscopy (XPS)

The X-Ray photoelectron spectroscopy enables the precise qualification/quantification of Cr-species and their oxidation states present within the first nm of a solid specimen. By focussing a beam of X-rays onto the sample surface, photoelectrons from the cathode material are emitted [70]. Since these photoelectrons own characteristic binding energies, representing their original electronic configuration, it is possible to determine their exact electronic states and thus receive information about the in-situ composition of the measured cathode surface. Therefore, the XPS-device "Phi5000 VersaProbe II" provided by "ULVAC-Phi, Inc." is utilized. The measurements are performed with an Al k-alpha source, emitting monochromatic X-rays with energies of 1.486 keV. During the measurements, a range of 200 µm is analyzed with the adjusted settings of 50 W and 15 kV. All binding energies are normalized to the value of 285 eV for the C-C sp^3-orbital.
Detailed information about the measured spectra are shown in Table 9.

Table 9: ***XPS parameters***

Overview spectra	
Passing energy	187.5 eV
Step size	0.8 eV
Time/step	100 ms
Detailed spectra	
Passing energy	23.5 eV
Step size	0.1 eV
Time/step	100 ms

To guarantee reliable and reproducible high-quality results, all ICP-OES and XPS measurements are performed at our partner institute ZEA-3 which is part of the Forschungszentrum Jülich GmbH and belongs to the Helmholtz Association.

5. Results & Discussion

In order to investigate the chrome related degradation behavior of SOFCs, standard anode-supported full-cells as well as symmetrical electrolyte-supported half-cells are investigated. Here, symmetrical half-cells (equipped with two cathodes/air electrodes) enable the exclusion of any anode contribution which facilitates the evaluation of cathode related degradation processes such as Cr-poisoning.

5.1. Anode-Supported SOFC Characterization

In a first step, commercially available anode-supported SOFCs (Co. CeramTec) are analyzed with help of several different pre-/post-test and in-operando characterization methods. As LSCF-cathodes represent the state-of-the-art materials in anode-supported SOFC-technology, the focus is drawn to their degradation behavior in relation to the operating temperature, air-humidity and applied current densities (i.e. overpotentials) in absence/presence of a Crofer 22 H Cr-source.

5.1.1. ASC Pre-Test-Characterization

Since all cells were produced within the same batches of an optimized industrial process, pre-test measurements of anode-supported SOFCs are only performed by scanning electron microscopy (Figure 5.1). Within the measurements at magnifications of 3000x (A) and 5000x (B) a highly porous cathode structure is shown.
Here, particle sizes of below 1 µm up to agglomerated particle sizes of above 20 µm are depicted. This highly porous structure provides a high internal surface area and thus various electrochemically active reaction sites and, furthermore, enables efficient cathode-gas (air) diffusion within the electrode.

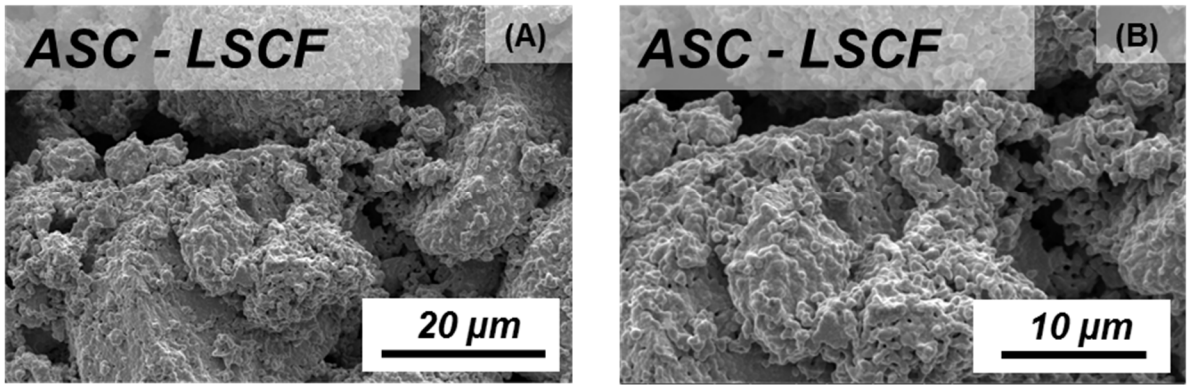

Figure 5.1: SEM pictures with a magnification of 3000x (A) and 5000x (B) of an anode-supported SOFC sample (equipped with a LSCF-cathode) before electrochemical treatment.

5.1.2. Electrochemical In-Operando Analysis of ASCs: DC & AC Characterization

For an in-depth analysis of the electrochemical cell response of anode-supported SOFCs (full-cells), in-operando measurements are performed for various temperatures, current densities, under dry and humid cathode-gas conditions as well as in absence/presence of a Crofer 22 H

Cr-source (see chapter 4.5.1). In order to interpret the influences of these variable operating conditions on the Cr-poisoning behavior, detailed DC and AC measurements are evaluated.
In Figure 5.2 current/voltage characteristics (A/B) and impedance potential scans (A1/A2 and B1/B2) of two ASCs, operated at 900 °C under open-cell conditions in absence and presence of Crofer 22 H (top and bottom), are exemplarily shown.
The I/V characteristics represent the individual cell potentials as a function of the current density and thus the overall cell performance. In (A), a strong decrease of the cell performance between the initial (Start: 48 h OCV, dry) and the final measurement (End: 48 h 1 $A.cm^{-2}$, humid) is shown. As the corresponding time period in between the measurements amounts to 400 h (see measuring schedule for ASCs, Figure 4.4) it can be stated that even small periods induce cell degradation. The potential scan in (A1) represents individual cell impedance scans with respect to its open cell voltage, after 48 h under dry air conditions in absence of a Cr-source. Here, the polarization resistance (R_{pol}) decreases from a value of 650 $mOhm.cm^2$ (OCV) to a value of 40 $mOhm.cm^2$ at 0.6 V. However, after final measurements at 1 $A.cm^{-2}$ under humid conditions (A2), increased R_{pol}-values of 750 $mOhm.cm^2$ (OCV) and 50 $mOhm.cm^2$ (0.6 V) are revealed. This increase in resistance again indicates a clear degradation tendency.
In (B), I/V characteristics for a structurally identical anode-supported SOFC (full-cell) in presence of a Cr-source also reveal strong degradation tendencies between initial and final measurements. Here, the potential scans in (B1) indicate a reduction of R_{pol} from 1550 $mOhm.cm^2$ (OCV) to 30 $mOhm.cm^2$ (0.6 V) after 48 h at OCV and dry air conditions. After the final measurement period at 1 $A.cm^{-2}$ (B2) the polarization resistance decreases from a value of 1725 $mOhm.cm^2$ to 30 $mOhm.cm^2$.
By comparison of initial and final potential scans either in presence or absence of Crofer 22 H, increasing resistances and thus reduced cell performances can be stated. Even though only slight shifts of the ohmic resistance (R_{ohm}, first intercept of the X-axis) can be observed for each cell, an increase of the polarization resistance is detected. The total resistance (R_{total}, second intercept of the X-axis) of each impedance potential scan represents the slope of a specific point on the respective I/V curve at the given potential (e.g. OCV, OCV-50 mV etc.). As an increase of R_{total} can be detected together with an increase of the slope of the respective I/V curve, a consistent behavior between DC and AC measurements can be assumed.
However, the majority of the impedance evaluation within the next chapters is conducted at a steady potential of 0.7 V. This enables a valid comparison between different samples and operating conditions. Furthermore, it simplifies the correlation between impedance and I/V characteristics as the resistances can be correlated to the cell performance at a specific point in the I/V curves.

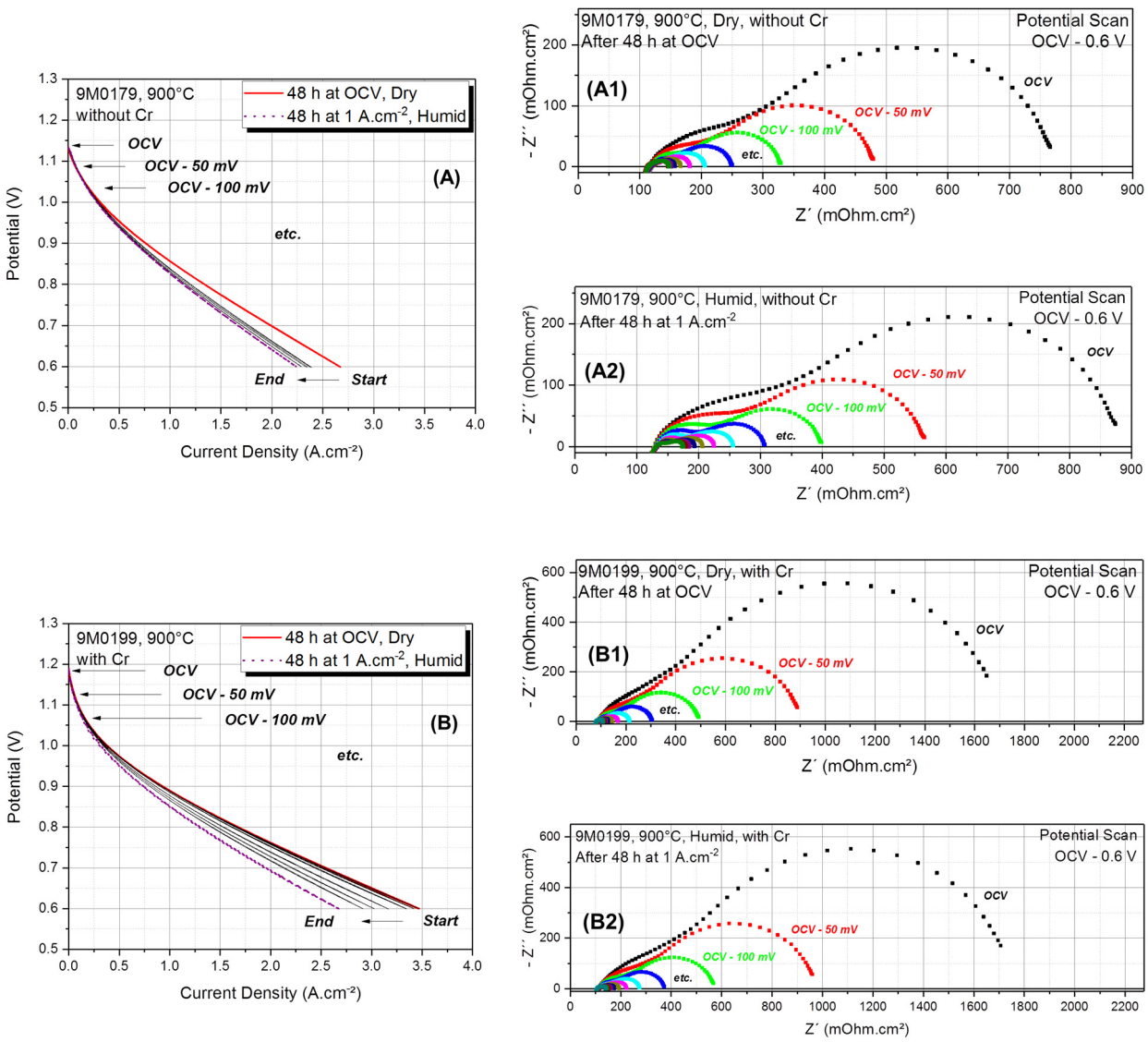

Figure 5.2: Electrochemical I/V (A/B) and related impedance characterizations (A1/A2 and B1/B2) for two different samples operated at 900 °C in absence (top) and presence of a Cr-source (bottom). The colored I/V-curves are represented by the initial/final impedance potential scans (48h at OCV / 48h at 1 A.cm^{-2}).

In addition to the impedance potential scans at 900 °C, Figure 5.3 depicts all respective I/V-curves of a measurement cycle incl. an initial and final performance identification at 0.7 V (e.g. Initial: 1.98 A.cm^{-2}; Final: 1.65 A.cm^{-2}). Furthermore, potentiostatic impedance characterizations (0.7 V) after 48h periods of galvanostatic applied overpotentials (OCV, 0.5 A.cm^{-2}, 0.75 A.cm^{-2} and 1 A.cm^{-2}) for dry and humid cathode-gas atmospheres are shown. In (A), a strong decrease of the cell performance of sample 9M0179 (absence of a Cr-Source) can be detected between the initial measurement (48 h at OCV, dry) and all following measurements. Regarding the impedance scans at 0.7 V in (A1) the initial curve shows a strong shift of the ohmic resistance (R_{ohm}: 115 mOhm.cm²) as well as strong deviations in its total (R_{total}: 149 mOhm.cm²) and polarization resistance (R_{pol}: 34 mOhm.cm²) in comparison to the other measurements. Alongside these changes, also the curve progression differs, indicating an alternating contribution of individual physicochemical processes. No such

strong shift of the ohmic and polarization resistance can be observed for any following measurement of an ASC at 900 °C in the absence of chrome. Here, the R_{ohm} ranges from 122-126 mOhm.cm² and the R_{pol} amounts to 50 mOhm.cm².
Also for sample 9M0199 which is measured in presence of Crofer 22 H, strong performance losses between the initial and final measurements (Initial: 2.55 A.cm^{-2}, Final: 1.95 A.cm^{-2}) can be confirmed (B). In this case, stronger losses are detected between the individual measurement in humid air as compared to dry air conditions. This can be also confirmed by the impedance scans in (B1) as they reveal stronger ohmic shifts and slight increases of the polarization resistances solely for humid air conditions ($R_{ohm,\ humid}$: 88-105 mOhm.cm^2, $R_{pol,\ humid}$: 30-40 mOhm.cm^2).
In contrast to measurements at 900 °C in absence of chrome, no strong initial shifts/increases of the R_{ohm} and R_{pol} can be determined for experiments in presence of a Cr-source. Here, the occurrence of stronger degradation tendencies can be related to air humidity. In general, sample 9M0199 shows better performances than its counterpart in the absence of chrome (Initial: 2.55 A.cm^{-2} > 1.98 A.cm^{-2}; Final: 1.95 A.cm^{-2} > 1.65 A.cm^{-2}). These findings match the impedance results since ohmic, polarization and total resistances tend to smaller values. As measurement procedures are identical for both samples and no issues in the execution of the measuring schedule are expected nor variations in the cell compositions are assumed, insufficient contacting of both electrodes should be the main reason for observable performance drops. For this reason, an adjustment factor for all utilized samples of a certain temperature level within the detailed EC-related analysis, has been established (see chapter 5.1.4).

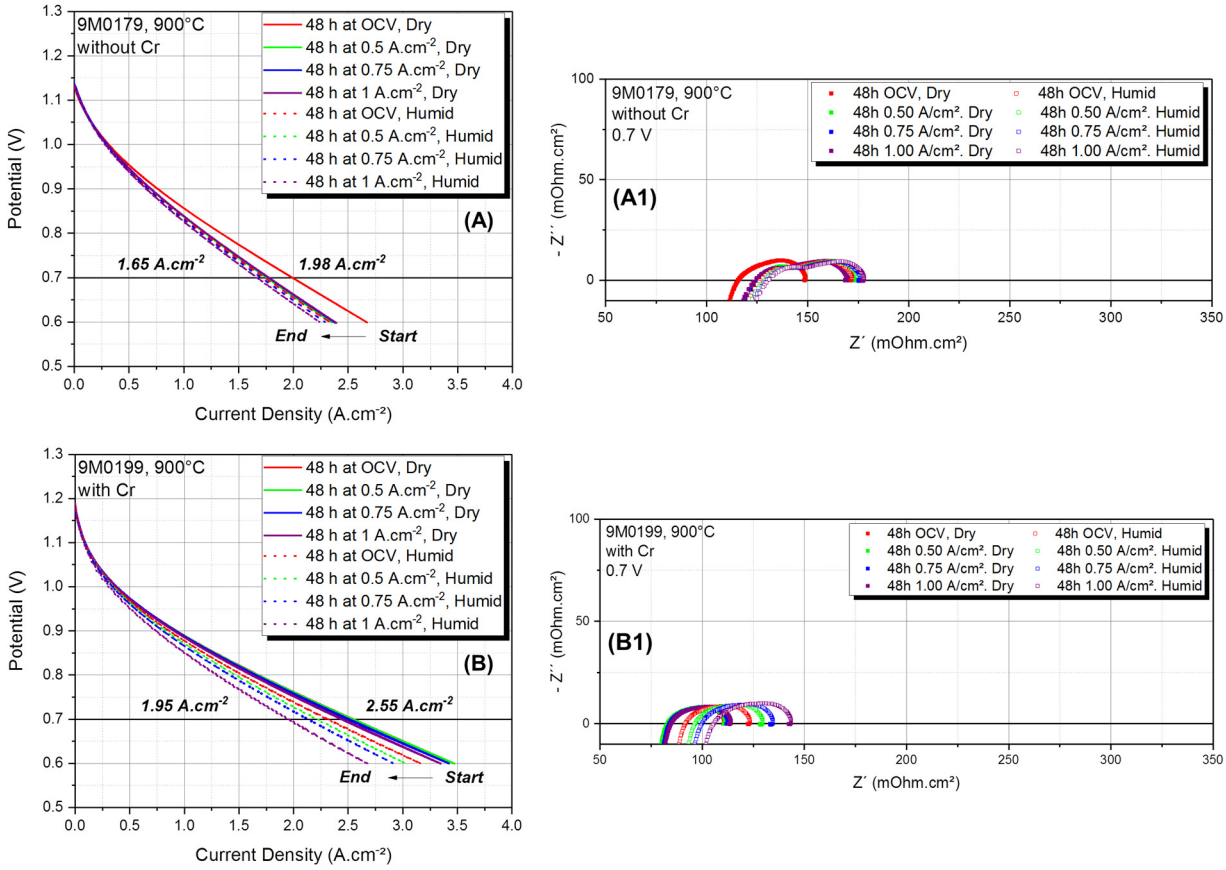

Figure 5.3: Electrochemical I/V characterization incl. cell performances of the initial and final measurements at 0.7 V (A/B) as well as impedance scans at 0.7 V after 48 h of various operating conditions (A1/B1) for two different samples operated at 900 °C in absence (top) and presence of a Cr-source (bottom).

Unlike previous measurements, Figure 5.4 describes the physicochemical behavior of two samples at 800 °C in presence and absence of chrome, respectively. In (A) sample 9M0285 indicates a performance drop from an initial value of 1.65 A.cm^{-2} to 1.26 A.cm^{-2} at the end of the measuring cycle. Also in this case, a stronger performance drop between the first (48 h at OCV, dry) and all following measurements can be stated. With exception of the initial curve, no increased performance drops are detected (even with increasing the air humidity). The respective impedance curves at 0.7 V (A1) indicate an exceptional strong increase of the ohmic resistance within the first measurements (148-170 mOhm.cm^2) and, thus, confirm the trend of the I/V-characterization. However, neither an increase of the polarization resistance nor an observable change in the curve progression can be detected between those measurements. All further curves show continuously increasing ohmic and polarization resistances. The latter show slightly stronger increases under humid air conditions.
In presence of chrome (sample 9M0349, B), a performance decrease from 1.36-0.92 A.cm^{-2} is depicted. Here, no exceptional strong performance loss can be detected between the first two measurements. Nevertheless, stronger degradation tendencies, as observed for dry conditions, can be stated by utilization of humid air. This trend is also confirmed within the impedance analysis (B1), as measurements in humid atmospheres reveal stronger shifts of the ohmic resistances ($R_{ohm, dry}$: 155-162 mOhm.cm^2, $R_{ohm, humid}$: 175-215 mOhm.cm^2) as well as strongly increased polarization resistances ($R_{pol, dry}$: 70-78 mOhm.cm^2, $R_{pol, humid}$: 77-125 mOhm.cm^2).

Besides increasing ohmic and polarization resistances in presence of a Cr-source, also the curve progressions change in the mid-frequency regime for periods of high overpotentials (> 0.5 A.cm^{-2}). This, however, is not observed in the absence of Crofer 22 H and, thus, points on a change of the cell electrochemistry.

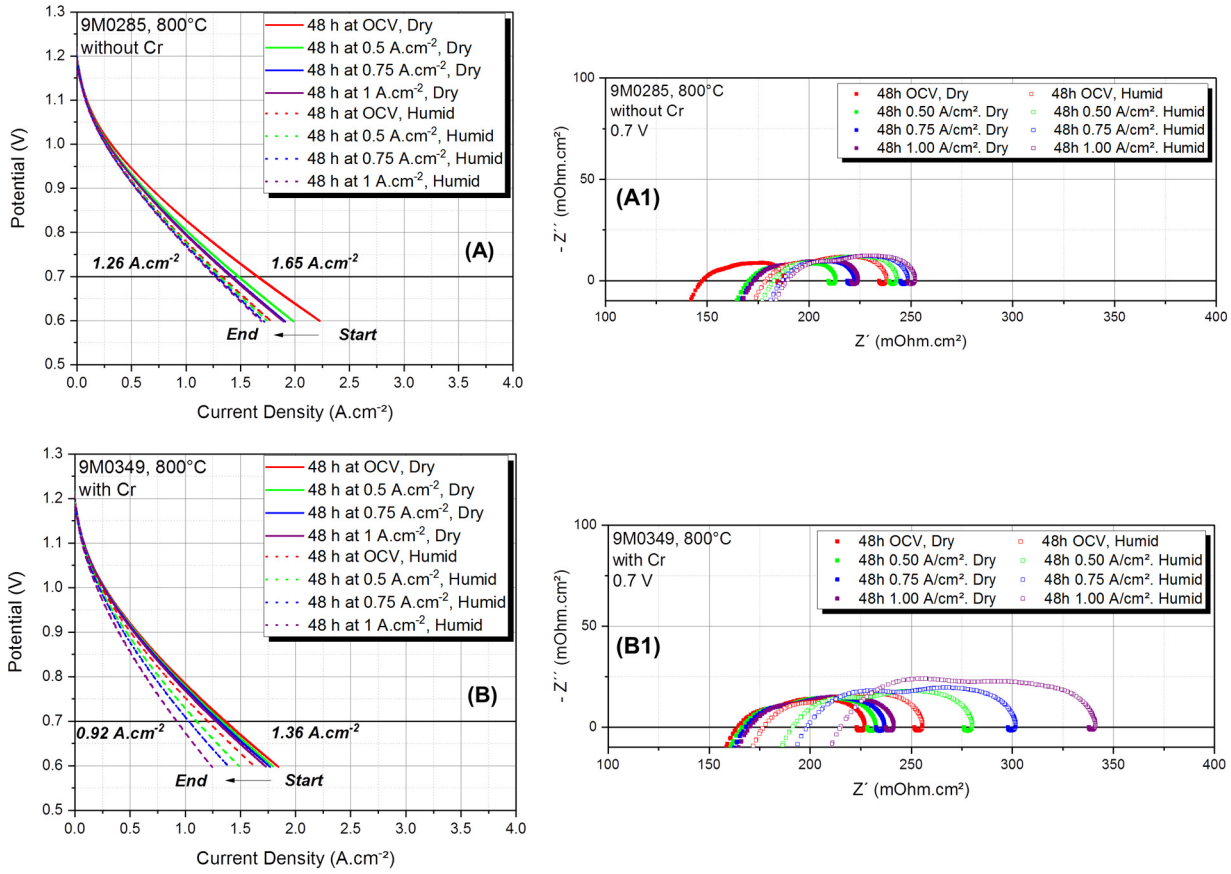

Figure 5.4: Electrochemical I/V characterization incl. cell performances of the initial and final measurements at 0.7 V (A/B) as well as impedance scans at 0.7 V after 48 h of various operating conditions (A1/B1) for two different samples operated at 800 °C in absence (top) and presence of a Cr-source (bottom).

Figure 5.5 depicts DC and AC characterizations of two anode-supported SOFCs at an operating temperature of 700 °C in presence and absence of a Cr-source. In this case, the low cell performances decrease from 1.21 A.cm^{-2} to 0.74 A.cm^{-2} for sample 9M0275 in the absence of chrome (A). Here, no increased performance drop between the measurement after 48 h of operation at OCV in dry atmospheres and all following measurements, can be observed. For the first time, measurements in the absence of chrome show noticeably stronger degradation tendencies for humid conditions than observed within dry measurements. Both trends can be supported with help of the impedance characterization in (A1). Additionally, they indicate an increase of the R_{ohm} from 205 mOhm.cm^2 to 280 mOhm.cm^2 and the R_{pol} from 60 mOhm.cm^2 to 155 mOhm.cm^2 (Initial to final measurement).
In the presence of Crofer 22 H (B), a performance loss from 0.66 A.cm^{-2} to 0.52 A.cm^{-2} is described. In this case solely a slight humidity related degradation trend can be observed. In (B1), large ohmic and polarization resistances are detected (R_{ohm}: 265-325 mOhm.cm^2, R_{pol}: 220-287 mOhm.cm^2) that help to understand the very low cell performances in (B). It should

be stated, that for both samples it was not possible to perform measurements after 48 h of operation at 1 A.cm^{-2} and humid air conditions, since anode-sided Ni-reoxidation could not be completely excluded.

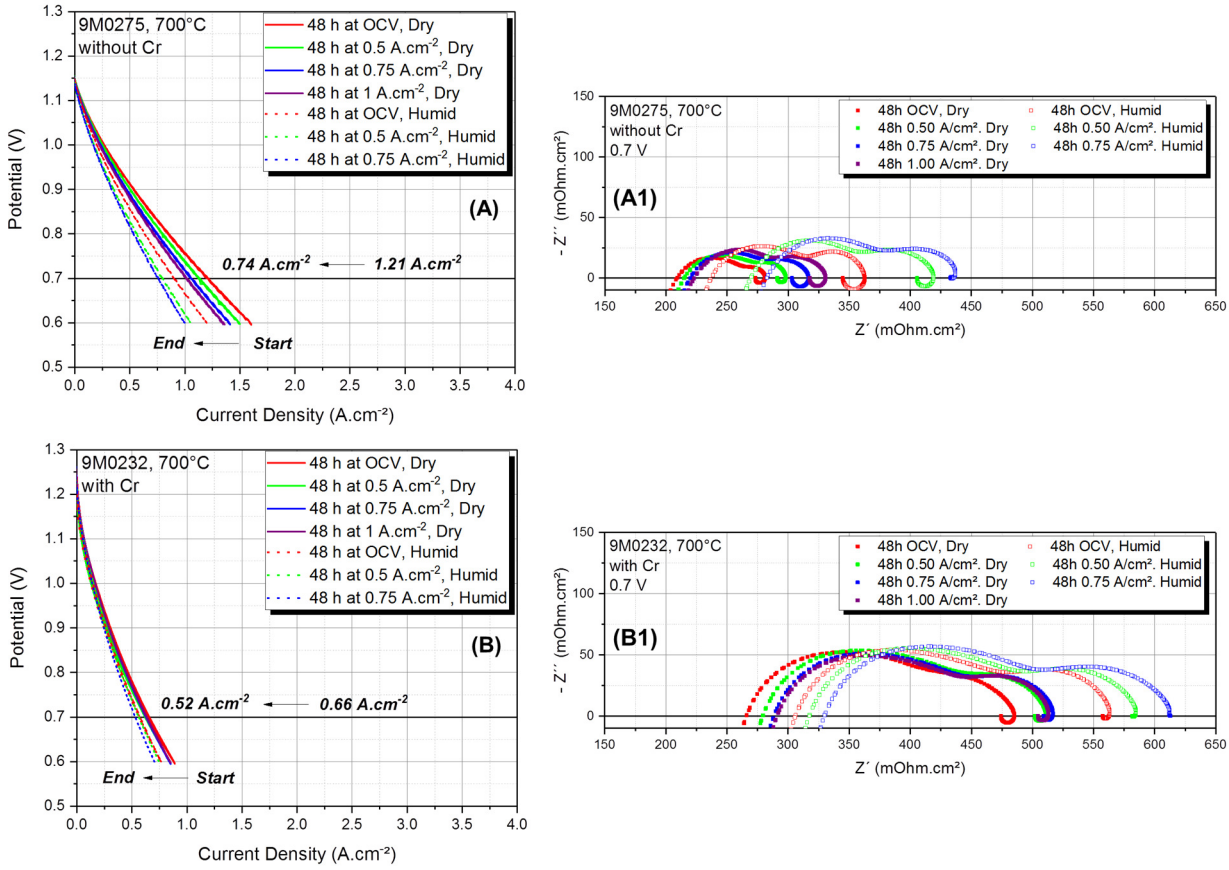

Figure 5.5: Electrochemical I/V characterization incl. cell performances of the initial and final measurements at 0.7 V (A/B) as well as impedance scans at 0.7 V after 48 h of various operating conditions (A1/B1) for two different samples operated at 700 °C in absence (top) and presence of a Cr-source (bottom).

By comparison of all I/V-characterizations and impedance scans at operating temperatures of 900 °C, 800 °C and 700 °C in presence/absence of a Cr-source, higher ohmic, polarization and total resistances can be detected for lower temperatures. This leads to lower overall cell performances which, according to fundamental thermodynamics and kinetics, is no surprise. Furthermore, measurements at all temperatures show an increased cell degradation with increasing the air humidity in presence of chrome. Additionally, for measurements at 900 °C and 800 °C, initial performance drops between the first measurements in absence of chrome, can be stated. This trend is not observed for an operating temperature of 700 °C.
However, all measurements in presence/absence of chrome reveal the presence of inductive loops in the low-frequency regime. As these loops are unlikely to be interpreted as test-rig related artifacts, real processes are considered as their primary reason (see chapter 5.1.3).

In order to confirm the quality, stability and reproducibility of the experimentally determined data, the area specific resistance (ASR) for DC measurements and the total resistance (R_{total}) for AC measurements are determined. Whilst the R_{total} can be identified by the low-frequency interception value (interception with the X-axis) in the impedance plots at 0.7 V, the ASR is

determined by calculation of the slope of each individual I/V-curve between 0.75 V-0.65 V. To guarantee reliable and reproducible data, both values have to coincide. Table 10 represents the ASR and R_{total} for samples at temperatures between 900 °C-700 °C, in presence/absence of chrome, for dry and humid air as well as exemplarily after 48 h load periods at OCV and 1 $A.cm^{-2}$. In general, all three temperatures reveal sufficient conformities between the ASR and R_{total} even though stronger differences of both values can be detected for 700 °C. As already mentioned for the comparison of electrochemical cell performances of Cr-exposed and non-exposed samples at 900 °C, strong variations of the cells initial output values (marked in **blue**) can be confirmed. Since any experimental issues as well as strong degradation tendencies within the first operating hours can be excluded, insufficient contacting of the electrodes is assumed. To overcome this problem and establish an identical starting point for the in-depth analysis of individual resistances, the initial R1-resistances (ohmic resistances after 48 h periods at OCV, dry) are normalized to the lowest R1-value at a certain temperature (e.g. $R1_{900°C}$: 155 $mOhm.cm^2$ to $R1_{900°C,\ Crofer22H}$: 80 $mOhm.cm^2$). The determined factor is then used to adapt the remaining resistances.

Table 10: ***Cell performances and quality of the experimental data***

Temp. (°C)	*Cr-Source*	*Humidity (%)*	*Load-Period ($A.cm^{-2}$)*	*Output ($A.cm^{-2}$)*	*ASR ($mOhm.cm^2$)*	*R_{total} ($mOhm.cm^2$)*
900	x (9M0179)	Dry	OCV	**1.98**	149.5	148.6
			1	1.78	169.6	168.5
		3.5	OCV	1.74	172.8	171.4
			1	1.65	179.8	176.9
	Crofer 22 H (9M0199)	Dry	OCV	**2.55**	111.2	110.3
			1	2.43	115.6	114.0
		3.5	OCV	2.32	122.5	122.3
			1	1.95	144.8	142.4
800	x (9M0285)	Dry	OCV	**1.65**	183.6	184.3
			1	1.41	220.2	220.5
		3.5	OCV	1.34	234.0	234.4
			1	1.26	248.2	248.4
	Crofer 22 H (9M0349)	Dry	OCV	**1.36**	222.9	222.9
			1	1.27	236.9	237.3
		3.5	OCV	1.20	251.7	251.5
			1	0.92	336.3	337.9
700	x (9M0275)	Dry	OCV	**1.21**	268.9	273.1
			1	1.02	319.4	317.7
		3.5	OCV	0.90	356.3	344.7
			1	0.74	--	--
	Crofer 22 H (9M0232)	Dry	OCV	**0.66**	453.8	474.2
			1	0.63	503.9	504.5
		3.5	OCV	0.57	544.2	557.5
			1	0.52	--	--

5.1.3. Electrochemical In-Operando Analysis of ASCs: DRT-Analysis and EC-Development

Previous measurements represented a short overview of the complexity of electrochemical responses related to a change of operational parameters such as temperature, humidity and current density in presence and absence of a Cr-source. However, to understand the origin of these responses, their link to cell-degradation and whether it is related to Cr-deposition, individual processes have to be identified. Furthermore, their contribution to the overall cell impedance has to be determined.

As complex Nyquist plots often lead to misinterpretations of the number of polarization processes, the distribution of relaxation times (DRT) method is used. Here, the values for real and imaginary parts of the impedance are transformed into the frequency domain which helps to separate the individual time constants [71]. Figure 5.6 represents the 2-dimensional transformation of the respective impedance results at 750 °C and open cell conditions. Besides a better separation of the related time constants, the 2-dimensional DRT also allows for a better identification of the serial resistance as well as inductive effects as no non-negativity constraint is used. With the help of both plots, it is possible to clearly identify four separate time constants. Starting with (IV), a single symmetrically shaped peak at 0.07 Hz can be detected showing a less pronounced capacitive behavior than observed for the other time constants. The second peak (process III) at 10 Hz is represented with an asymmetric shape in both plots. This allows for the assumption that at least contributions of two time constants are strongly overlapping, leading to the asymmetric peak formation. Furthermore, also a strong overlapping of processes (II) and (I) can be detected. Here, a shoulder formation at 131 Hz of the main peak at 1 kHz can be observed. Additionally, the DRT-plot of the imaginary part of the impedance reveals the presence of a second shoulder at 10 kHz. As this observation cannot be confirmed within investigations for the real part of the impedance, the presence of an artifact which is induced by the adjacent inductive effect is assumed.

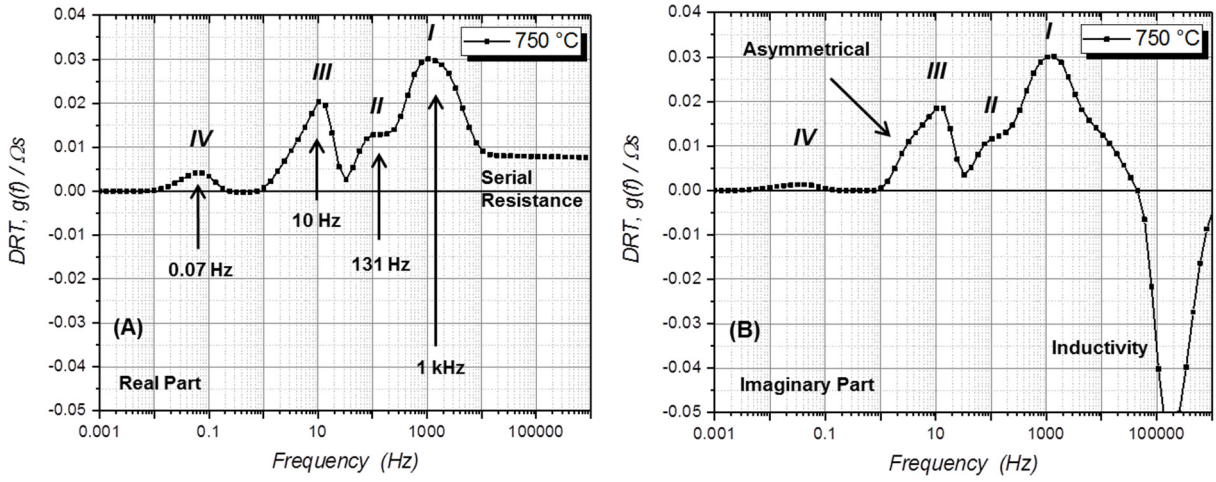

Figure 5.6: 2-D distribution of relaxation times (2-D DRT) of anode-supported SOFCs with a standard LSCF-cathode at 750°C. (A) represents the DRT for the real part whereas (B) depicts the imaginary part. 2-D DRT procedure conducted by Andreas Mertens (IEK-9).

Figure 5.7 represents a 3-dimensional plot of the relaxation time distributions for temperatures between 900 °C - 750 °C of the real and imaginary part, respectively. By rotating the plot about 180 °C, the 2-dimensional cross-sectional plot shown in Figure 5.6 would be visible. It can be observed that process (IV) is more pronounced at temperatures below 775 °C and at temperatures above 875 °C. However, this does not an absence of the process for temperatures ranging between 775 °C-875 °C as its contribution lies within the noise level of the measurement. The previously detected asymmetric curve shape of process (III) disappears with increasing temperatures. At 900 °C, a slightly broadened and almost symmetrical curve progression is shown. Even though the shoulder formation of the coupled processes (II and I) decreases with higher temperatures, the presence of the process is still detectable at 900 °C. In comparison to processes (IV) and (III), the coupled processes (II and I) show a decrease of their contributions to the overall cell impedance with increasing the operating temperature (accompanied with peak narrowing).

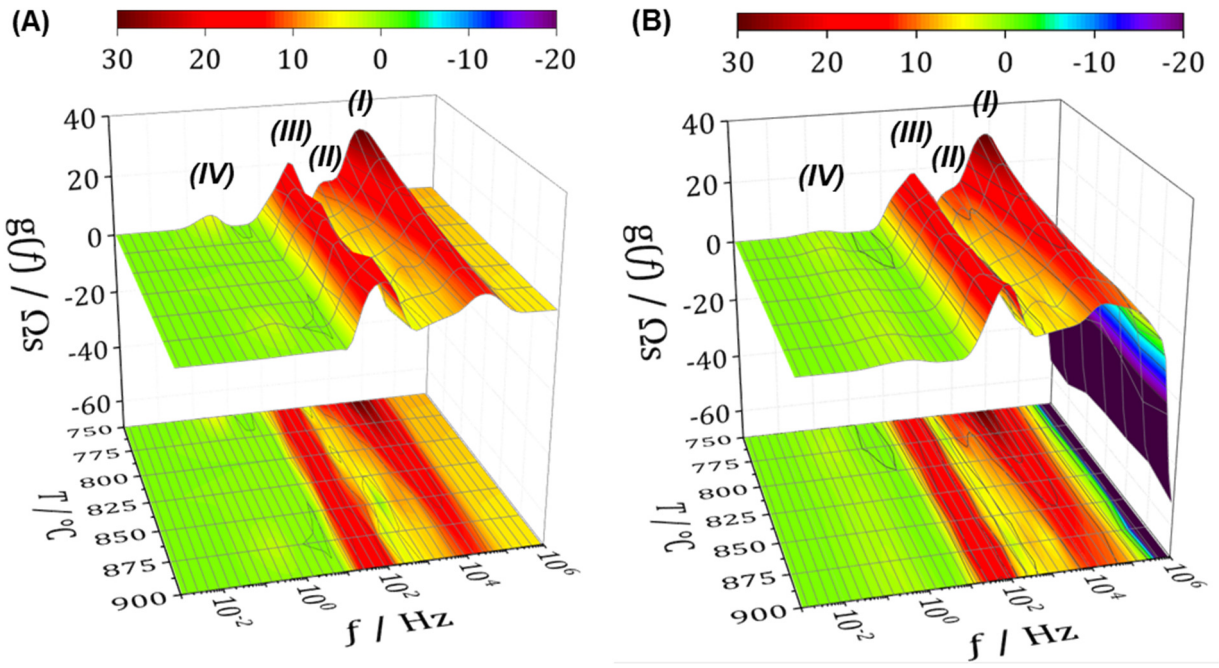

Figure 5.7: 2-D distribution of relaxation times of anode-supported SOFCs with a standard LSCF-cathode at temperatures between 900 °C-750 °C (steps: 25 °C) all depicted in a 3-D plot. (A) represents the DRT for the real part whereas (B) depicts the imaginary part. 2-D DRT procedure conducted by Andreas Mertens (IEK-9).

To prove the reliability of the DRT-spectra, the results are transformed back from the frequency domain into the original representation. By comparison of the residual spectra of original and back-transformed data it can be stated that the transformation does not cause systematic errors within the data, thus proving the reliability of the DRT-method.

All of these results mark a strong temperature dependence on each of the underlying physicochemical processes. A comparison of the literature [60,62,63] (see chapter 3.4.3) and experimental data confirms the strong temperature dependency. Furthermore, comparing the process related frequencies allows for an adjustment of the related equivalent circuit model (Table 11). In contrast to the model developed by Ivers-Tiffée et al. (referred to as KIT-model [60,62,63]), an insufficient separation of the relaxation times of the processes of

oxygen surface exchange kinetics and O^{2-}-ion diffusivity in the bulk (cathode) as well as the gas diffusion inside the anode structure (within the experimental data) is assumed. The literature model describes the occurrence of both elements within frequencies of 4-20 Hz for Ws1 and 10-500 Hz for G1 [72,73] (already indicating a strong overlap of both elements), whereas the experimental data only describes one signal at frequencies of 10-100 Hz. Due to the asymmetrical nature of the signal related to process (III) as well as frequencies ranging between the literature values, one can assume a far more complex physicochemical behavior than the one that can possibly be separated with the DRT-method. However, the other peaks show a good correlation between literature and experimentally determined data-values. Slight frequency shifts can be attributed to small variations in the operating temperatures, the humidity values and general test-rig related differences.

Table 11: ***Signal comparison of literature and experimentally determined data***

Element	*Frequency*	*Physicochemical Process*
R4/CPE3, Literature Process (IV), R4/I2, Exp.	0.3-10 Hz [60,62,63] 0.07-1 Hz	Gas diffusion in the cathode structure
Ws1, Literature **Process (III), Ws1, Exp.**	4-20 Hz [60,62,63] 10 -100 Hz	Gas diffusion in the anode substrate
G1, Literature **Process (III), Ws1, Exp.**	10-500 Hz [60,62,63] 10 -100 Hz	Oxygen surface exchange kinetics O^{2-}-diffusivity in the cathode bulk
R3/CPE2, Literature Process (II), R3/CPE2, Exp.	2-8 kHz [60,62,63] 130 Hz-3 kHz	Gas diffusion Charge transfer reaction Ionic transport in the anode functional layer
R2/CPE1, Literature Process (I), R2/CPE1, Exp.	12-25 kHz [60,62,63] 1-25 kHz	

Together with the previous results it is possible to develop a suitable equivalent circuit model, based on the KIT-model, to describe the physicochemical behavior of the utilized anode-supported SOFCs in presence and absence of chrome. As an inadequate separation between the literature processes Ws1 and G1 has been observed, a single Warburg-type element (Warburg-short, W_s) is considered as the best description for these coupled processes. The derived EC-models are depicted in Figure 5.8. Both represent the same theoretical description of the related processes, but differ in their description of the high-frequency, test-rig related inductive behavior (A, MP03; B, MP04). Furthermore, process (IV) is coupled with an inductor (inductor 2) since the low-frequency regime of most Nyquist-plots shows an inductive semicircle. This finding is often assigned to adsorption/desorption processes which is an extension of the KIT-model. However, an in-depth analysis of all processes has to either prove or disprove literature values and experimental findings.

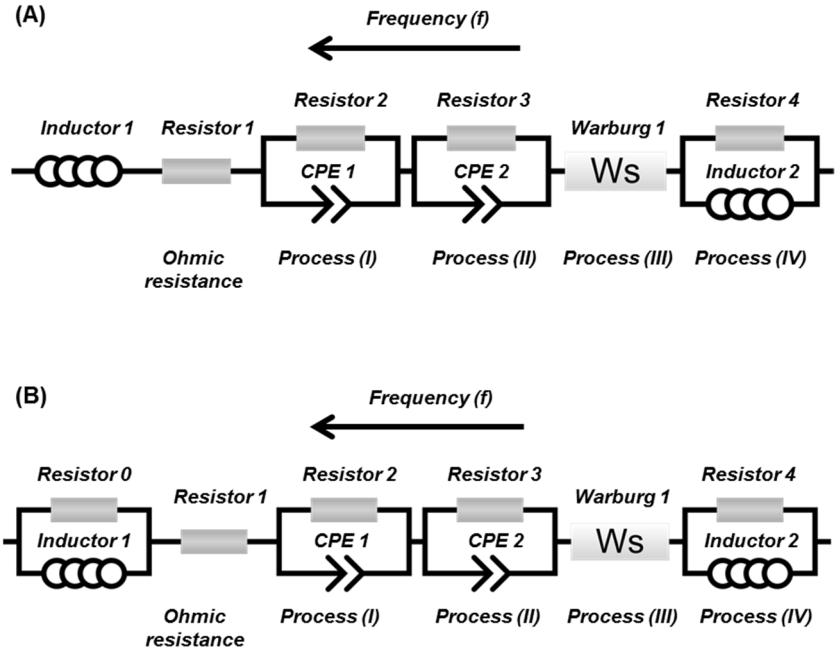

Figure 5.8: Utilized EC-model for the description of physicochemical process in anode-supported SOFCs with a standard LSCf cathode. Variations in the high frequency-regime are ascribed to the individual test-rig, (A) MP03 and (B) MP04.

Figure 5.9 depicts exemplary curves measured at 900 °C, 800 °C and 700 °C in the presence of chrome (A/B/C). Here, measured data (symbols) and the calculated fit (straight line), lie exactly on top of each other. To determine the quality of the conducted fits, residual plots have to be analyzed (A1/B1/C1). It is shown that the absolute residuals for both real and imaginary part of the impedances, range around a value of ± 0.5 mOhm.cm² for 900 °C and 800 °C as well as of ± 2.5 mOhm.cm² for 700 °C (in average). A sinusoidal behavior of the residual can be assigned to the already mentioned far more complex physicochemical nature of the processes. This also shows that the developed and utilized EC-model does not completely describe all system relevant processes. However, measurements at 700 °C reveal a less adequate coverage of the experimental data by the model. Taking the DRT-analysis into account, these findings are most probably accompanied by an asymmetrical peak of process (III) (as shown for 750 °C). As already mentioned, this can be explained by the occurrence of an additional process due to a better separation of the individual time constants. Since it is not possible to resolve the convolute of these contributions with the addition of a Gerischer Element (according to the KIT-model) nor with other elements, a better but still insufficient separation of the time constants at lower temperatures has to be considered. As various tested additional EC-element do not improve the goodness of the fit, the utilized models can be seen as the most adequate description of the cells electrochemistry.

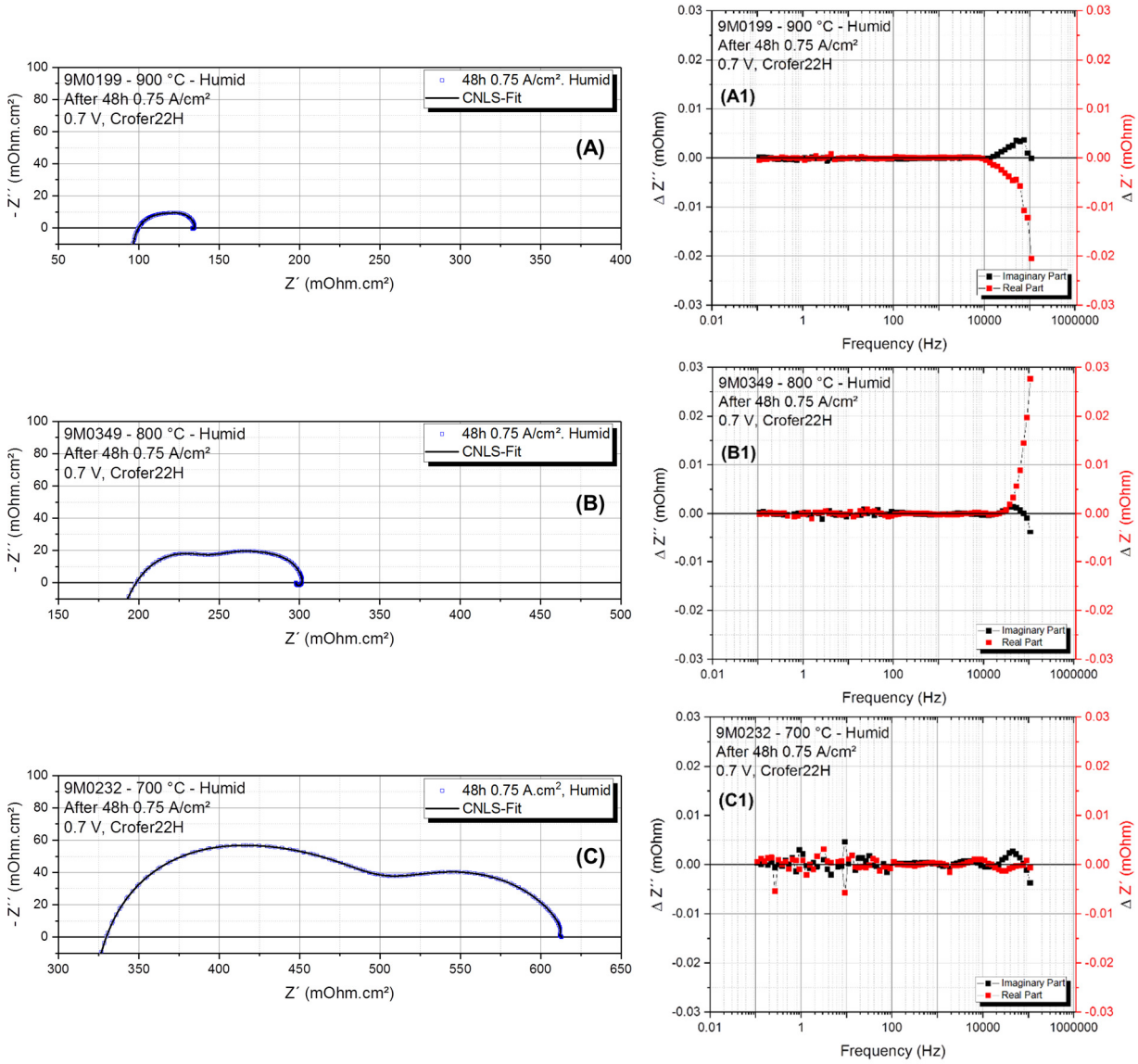

Figure 5.9: (A/B/C) Measured data incl. CNLS-fit, together with (A1/B1/C1) the corresponding residual-plots at 900 °C, 800 °C and 700 °C.

In order to further confirm the model and the assumed physicochemical processes, variations of the cathode-gas humidity and the applied overpotentials (current-densities), all in relation to the operating temperatures, are evaluated within the following chapters. Based on these results, it is possible to analyze the electrochemical cell response in absence/presence of a chrome source.

5.1.4. Electrochemical In-Operando Analysis of ASCs: In-Depth Analysis

As contact problems induced by the experimental setup are experienced, already mentioned correction factors for each temperature level have to be established. Therefore, samples with higher contact resistances at a certain temperature and thus lower electrochemical performances are normalized to the ohmic resistance (R1) of the initial measurement of the best contacted cell. This guarantees an equal starting point for all measurements at the respective temperature and facilitates investigations of the individual development of each element. As recently performed short-stack tests at current densities of 0.5 $A.cm^{-2}$ and

0.75 A.cm^{-2} revealed the presence of Cr-species on the cathode surface and close to the TPB, it can be assumed that the deposition of chrome occurs preferably at high cathodic overpotentials [3]. In a first step to prove these findings, 48 h periods of OCV and constant loads, such as 0.5 A.cm^{-2}, 0.75 A.cm^{-2} and 1 A.cm^{-2}, are applied for all anode-supported cells.
Figure 5.10 represents the development of the resistances R1, R2, R3 and R4 related to the applied current densities (0 equals OCV) under dry/humid conditions (A1/A2 and B1/B2) in absence (top, 9M0179) as well as presence (bottom, 9M0199) of chrome at 900 °C. In this particular example, all resistance-values of sample 9M0179 have been adjusted by a correction factor of 0.96. For this reason, the reference value R1 at OCV (solely for dry conditions) cannot be considered for comparison of samples 9M0179 and 9M0199.
In (A1), it is shown that the ohmic resistance R1 as well as R2 of sample 9M0179 remain constant. However, a negligible increase of R4 can be detected at current densities above 0.5 A.cm^{-2} (> 1 mOhm.cm^2). Besides an unexpected decrease of R3, no further degradation tendencies can be stated for dry air conditions in the absence of a Cr-source. Contrary to measurements in dry atmospheres, humid atmospheres (A2) reveal slight increases of both, the ohmic resistance R1 and R2 (6 mOhm.cm^2 and 3 mOhm.cm^2). Furthermore, analogously as observed in (A1), a negligable increase of R4 above 0.5 A.cm^{-2} can also be detected in humid atmospheres. In this case, R3 reveals an inconsistent trend which can be caused by larger errors within the fit.
In plot (B1) most of the resistances remain constant, independent on the applied current densities. Solely slight degradation tendencies are detected for resistances R1 and R4 at current densities above 0.75 A.cm^{-2}. Under humid conditions (B2), a steady increase of R1 as well as stronger increase of R2 for high current densities (> 0.75 A.cm^{-2}) can be observed. Here, no noticeable increase or decrease of the resistances R3 and R4 can be stated.
In comparison to sample 9M0179 measured in the absence of chrome, sample 9M0199 (presence of chrome) shows a stronger increase of the ohmic resistance R1 by 12 mOhm.cm² in humid air (OCV: 79 mOhm.cm²; 1 A.cm^{-2}: 91 mOhm.cm²) which equals an increase of 100 %. On the other hand, R2 displays an initial value of 6 mOhm.cm² being 32 mOhm.cm² smaller than in the absence of chrome. Except an increase of R2 at 1 A.cm^{-2} for humid conditions as well as no relevant degradation tendencies of other resistances can be detected.
It can be stated that, besides minor alterations of R4, the main difference of both samples can be attributed to the initial value of R2 and the development of both, R2 and the ohmic resistance.

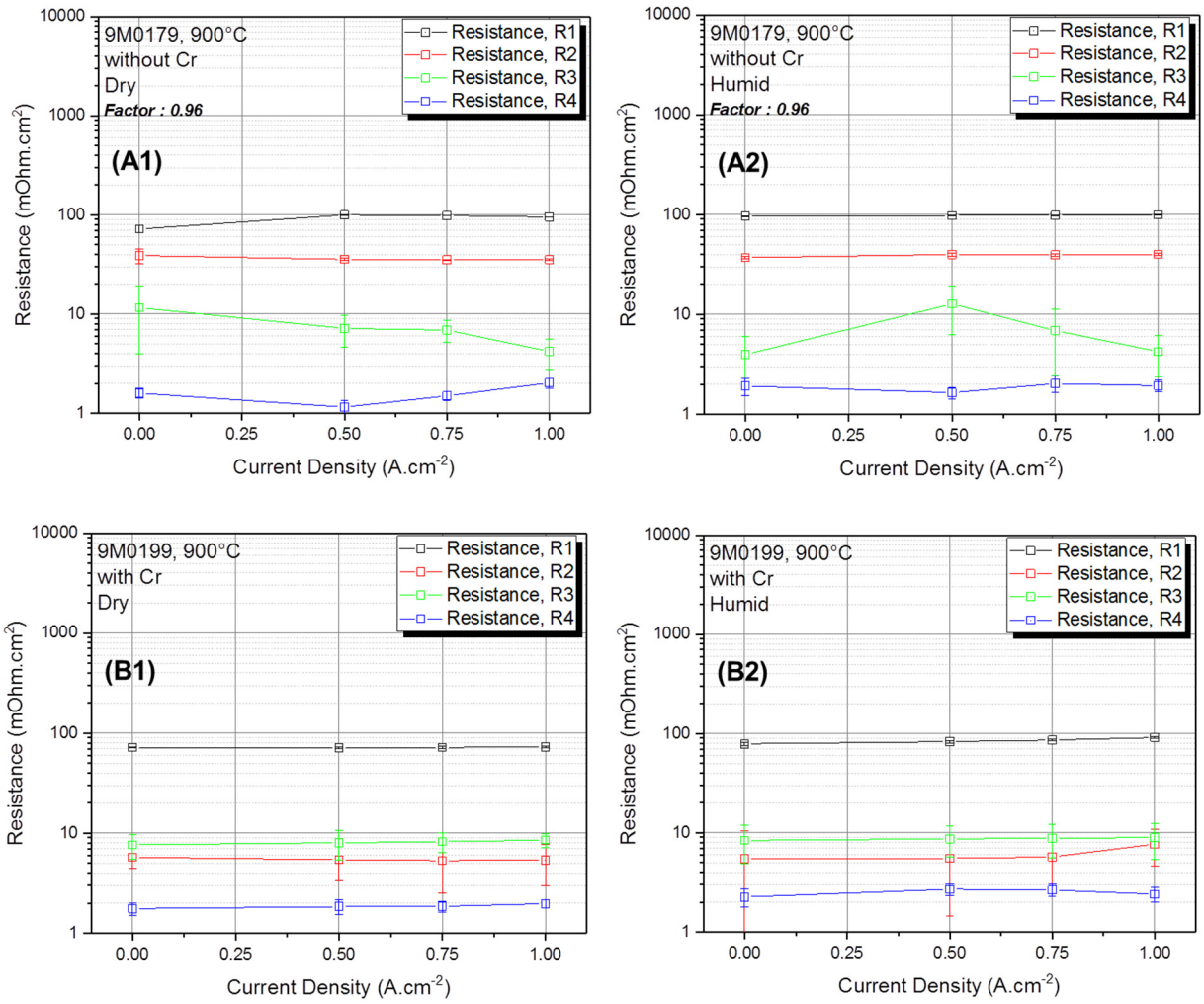

Figure 5.10: ASC-LSCF: Current density dependent development of R1, R2, R3 and R4 for 900 °C, dry (A1 and B1) and humid (A2 and B2) cathode-gas atmospheres as well as in absence (top) and presence (bottom) of chrome. The adjustment factor is depicted within the normalized plots.

In figure 5.11 the R-value development of resistances R1-R4 at an operating temperature of 800 °C is illustrated. Here, a correction factor of 0.90 has been established for the sample 9M0349.

For sample 9M0285, measured in the absence of a Cr-source, increasing values of the resistances R1 and R2 can be detected for both, dry and humid air conditions (A1 and A2).

It is shown that between the initial measurement and the first measurement under load (A1) the ohmic resistance as well as resistance R2 increase rapidly. However, only R1 shows a continuous growth, especially for higher current densities (> 0.5 $A.cm^{-2}$). Besides a small increase of R3 (> 0.75 A/cm^{-2}, A1) which is instantly followed by a decrease around the same amount (> OCV, A2), no further degradation trends can be observed in the absence of a Cr-source.

A continuous increase of both, R1 and R2, is detected in the presence of chrome (B1 and B2). Here, especially for humid air-conditions (B2), a strong development of both resistances is illustrated (R1: 28 $mOhm.cm^{-2}$, R2: 32 $mOhm.cm^{2}$). Also for sample 9M0285 no clear degradation tendencies can be observed for resistances R3 and R4.

By comparison of samples 9M0285 and 9M0349, it can be stated that both show developing resistance values for R1 and R2, respectively. This development, however, is far more pronounced for sample 9M0349 in presence of Crofer 22 H and humid air conditions. In consideration of the fitting errors (especially for R3), no degradation trend can be observed for R3 and R4 in absence/presence of chrome.

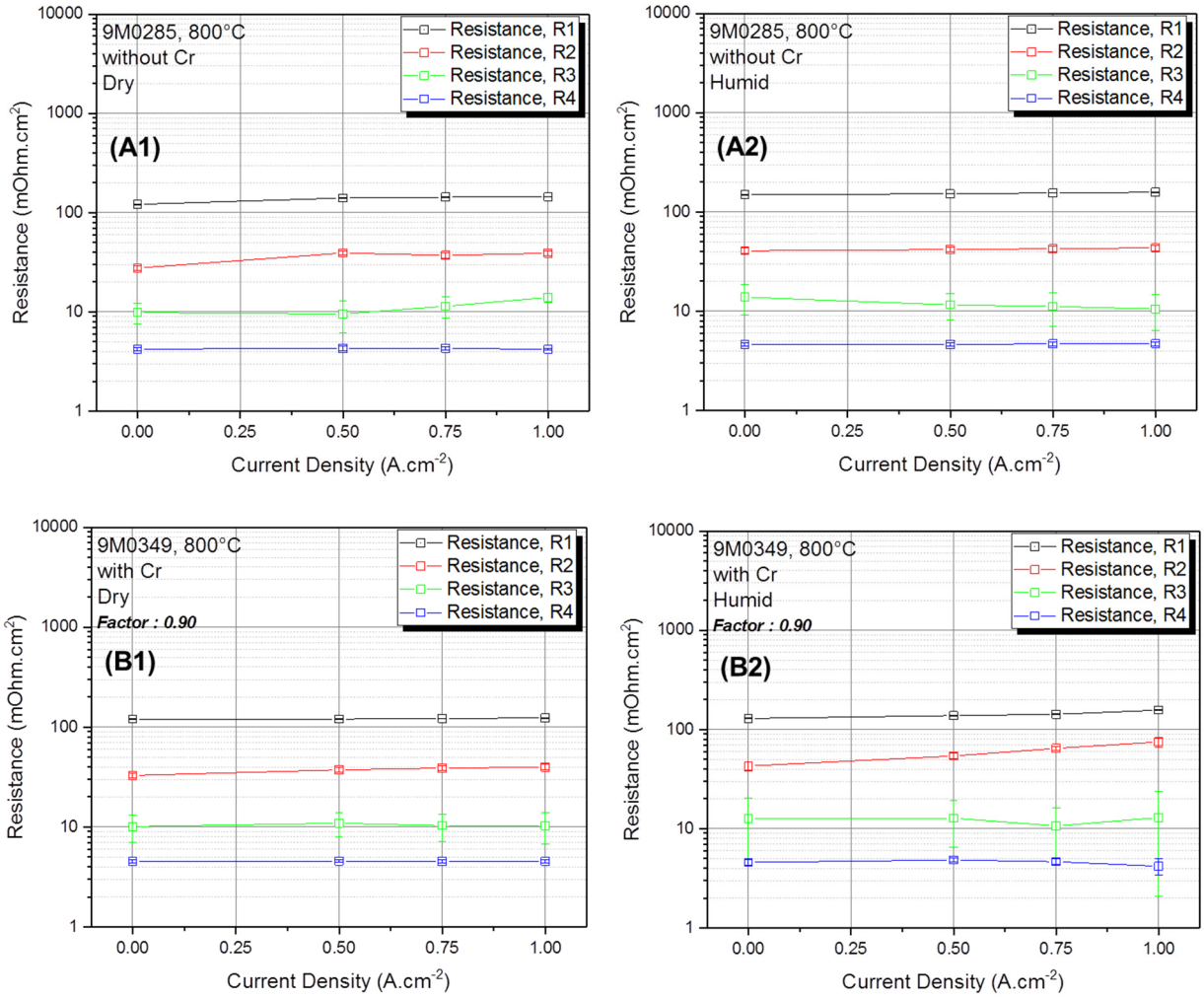

Figure 5.11: ASC-LSCF: Current density dependent development of R1, R2, R3 and R4 for 800 °C, dry (A1 and B1) and humid (A2 and B2) cathode-gas atmospheres as well as in absence (top) and presence (bottom) of chrome. The adjustment factor is depicted within the normalized plots.

Figure 5.12 represents the experimental findings of the individual resistance development at 700 °C. In this case, the correction factor of 0.79 is established for measurements of sample 9M0232 in presence of a Cr-source.

For sample 9M0275 (A1) a slight increase of R1 as well as a noticeable increase of R4 (8 mOhm.cm^2) can be stated. Contrary to these findings, no degradation trend can be observed for resistance R2. For R3, however, large fitting errors complicate its characterization. This trend is also shown for humid conditions (A2). Furthermore, for humid conditions a steady increase of the ohmic resistance, a noticeable increase of R2 at higher current densities as well as a decrease of R4 (both > 0.75 A.cm^{-2}) can be observed.

In the presence of chrome (sample 9M0232) a slight increase of R1 and an increase of R2 can be detected for dry air atmospheres (A1). Here, both, R3 and R4 show slightly decreasing degradation tendencies with applying a constant load of 0.5 A.cm^{-2}. In comparison, resistances R1, R2 and R3 show obvious degradation tendencies with the utilization of humid air (especially at current densities > 0.75 A.cm^{-2}).

In general, all resistances undergo a certain development which becomes pronounced under humid conditions. By comparison of samples 9M0275 and 9M0232 under humid cathode-gas conditions, higher absolute resistances can be confirmed for the process related resistances R2, R3 and R4 in the presence of a Cr-source. For all resistances, the absolute values most rapidly increase in combination with high current densities (> 0.75 A.cm^{-2}). Due to large fitting errors for R3 (sample 9M0275), a similar strong increase of its absolute values in the absence of chrome cannot be completely excluded. It is interesting that the absolute development of R1 under humid conditions is stronger in the absence of chrome (R1(9M0275): 109 mOhm.cm²; R1(9M0232): 70 mOhm.cm²). Furthermore, resistance R4 shows a contradictory behavior as it continuously increases, until a decrease at current densities of 1 A.cm^{-2} under humid conditions in the absence of a Cr-source, whereas in its presence, R4 shows a steady trend and even increases at 1 A.cm^{-2}, humid.

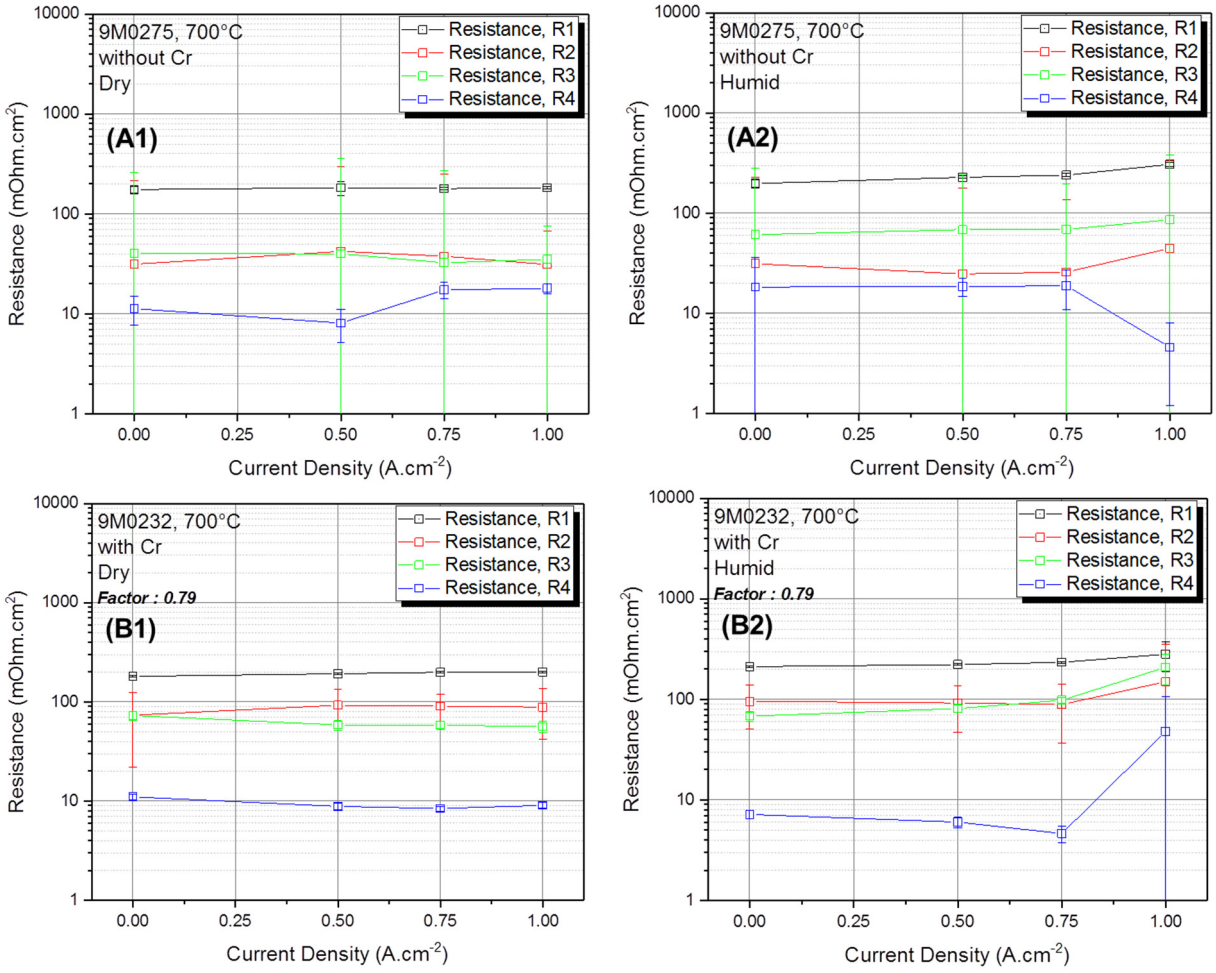

Figure 5.12: ASC-LSCF: Current density dependent development of R1, R2, R3 and R4 for 700 °C, dry (A1 and B1) and humid (A2 and B2) cathode-gas atmospheres as well as in absence (top) and presence (bottom) of chrome. The adjustment factor is depicted within the normalized plots.

According to the modified KIT-Model and the performed DRT-analysis, the Warburg-element should describe anode processes such as the gas diffusion in the anode substrate. In order to confirm this theory, the Warburg-development (Ws-Zw) is shown, analogously to R1-R4, as a function of the current density at temperatures of 900 °C, 800 °C and 700 °C for dry and humid conditions in absence/presence of chrome (Figure 5.13).
For an operating temperature of 900 °C increases of the Warburg-element can be stated for higher current densities for dry conditions in the absence of chrome (9M0179, A1) and for both, dry and humid conditions, if exposed to chrome (9M0199, A2).
At 800 °C, only in humid air atmospheres distinct degradation tendencies can be detected (B1 and B2). Here, especially in the presence of chrome (9M0349, B2), increased values are recognized at overpotentials above 0.5 $A.cm^{-2}$.
Contrary to the measurements at 900 °C and 800 °C, measurements at 700 °C (9M0275, C1 and 9M0232, C2) show large errors that complicate their evaluation. This was already explained by a certain inaccuracy of the utilized model at lower temperatures in relation to the Warburg-element (asymmetric peak formation).
However, it can be stated that stronger degradation tendencies are shown for samples operated at higher temperatures (> 750 °C) in the presence of a Cr-source. Additional measurements at 850 °C, 750 °C and 650 °C confirmed this trend.

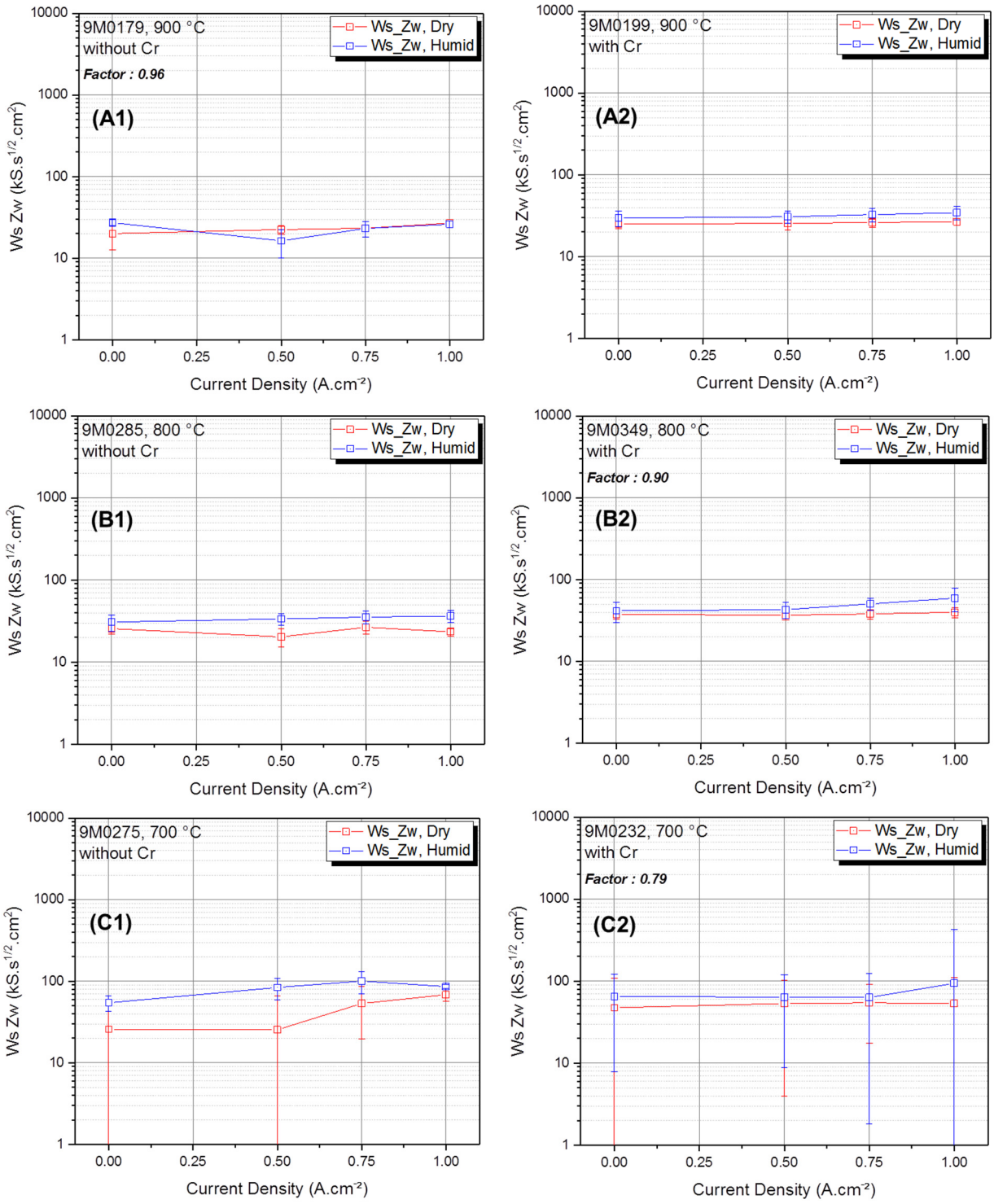

Figure 5.13: ASC-LSCF: Current density dependent development of the Warburg-element Ws_Zw in dry and humid atmospheres for 900 °C (top), 800 °C (middle) and 700 °C (bottom) in the absence (A1/B1/C1) and presence of chrome (A2/B2/C2). The adjustment factor is depicted within the normalized plots.

In summary, the electrochemical in-depth characterization reveals strong temperature dependencies of all resistances as well as the Warburg-element. Furthermore, by increasing the air humidity also the resistances (incl. Warburg) increase slightly. The results also show higher fitting errors at temperatures below 750 °C especially for the Warburg element. This fact confirms the results of the DRT-analysis as the occurrence of an asymmetric peak can be

detected at lower operating temperatures. In this case, a stronger overlapping of the individual process related time constants is assumed. With the introduction of load periods, the resistances show distinguishable differences in the presence of a Cr-source. Especially at temperatures above 800 °C, the ohmic resistance as well as the Warburg-element increase. With regard to the temperature, the highest increases of the resistance values in presence of chrome can be detected for humid conditions and high current densities (> 0.5 $A.cm^{-2}$). Focusing on the Warburg-element, a stronger and steady increase can be detected at higher current densities for humid/dry conditions (900 °C and 800 °C) in the presence of chrome than in its absence.

For the analysis of anode-supported SOFCs (equipped with a LSCF cathode) Cr-related degradation trends can be solely confirmed on a small scale. This fact can be ascribed to dominating anode contributions to the overall cell impedance and much smaller contributions of the cathode (also referred to the KIT-model and the adjusted model). As the anode provides major contributions to the respective impedance curves, applied current densities do not necessarily lead to sufficient cathodic overpotentials. One can assume that for anode-supported full-cells even higher current densities have to be applied to induce stronger cathodic overpotentials which would lead to larger amounts of Cr-deposits during identical operation times.

In a first attempt to prove this assumption, a standard anode-supported SOFC (sample 9M0231) is operated for a period of 336 h at a constant current density of 2 $A.cm^{-2}$ in presence of a Cr-source. Furthermore, the evaluation is performed in a humid environment as regular measurements showed stronger degradation tendencies with the utilization of humidified air. The individual resistance and Warburg developments of sample 9M0231 are represented in Figure 5.14. Contrary to previous measurements, resistances as well as the Warburg element are plotted in dependence of the operation time after the initial measurement, 168 h (7 days) and 336 h (14 days), respectively. Here, no process development related to the EC-model R4/I2 (see chapter 5.1.3) is illustrated as no inductive behavior in the low frequency regime has been detected. The plots reveal stronger degradation tendencies for resistance R2 and the Warburg element. By comparison of these values with the measurements at 900 °C (according to the ASC measuring scheme), percentual increases of 49.6 % for R2 (9M0199: 35.1 %) and 77.5 % for Ws-Zw (9M0199: 38.6 %) can be observed. However, R3 shows decreasing resistance values compared to previous measurements. Since the development of R3 depicts larger errors, a stable behavior as observed in previous measurements cannot be completely excluded.

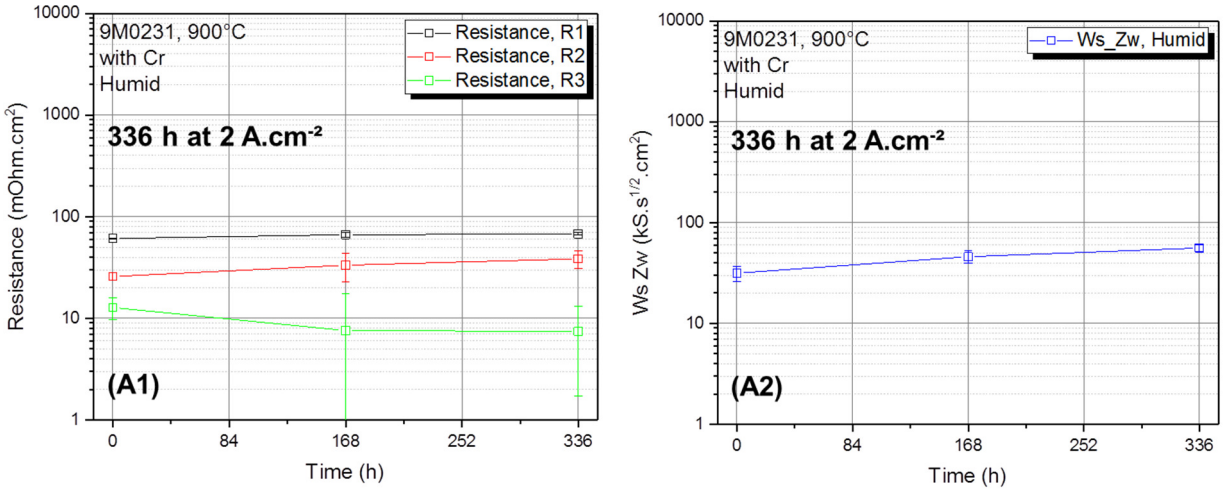

Figure 5.14: ASC-LSCF: Current density dependent development of the resistances R1, R2, R3 (A1) and the Warburg-element Ws_Zw (A2) at 900 °C in a humid atmosphere for a constant current density of 2 A.cm^{-2} in the presence of chrome. The measurements are performed for a time period of 336 h.

Since high overpotentials also induce stronger degradation tendencies of the anode layer, anode excluding cell-concepts need to be investigated. In a first approach, custom-built electrolyte-supported SOFC half-cells containing two layers of symmetrical arranged LSCF-cathodes, are investigated. Here, the driving force of the reaction can no longer be described as the oxygen partial pressure difference between the electrodes rather than by the applied overpotential. It should be mentioned that due to a 300 µm thick electrolyte, the absolute values of the ohmic resistances cannot be compared to the ASC measurements. However, to compare first relations between the individual polarization resistances of ESC and ASC measurements, the same test-rigs have been utilized. To prevent initial variations of the measurements caused by insufficient contacting, the initial R_{ohm} of sample 9M0409 is adjusted to its counterpart in the absence of chrome (9M0410) by a factor of 0.86 (Figure 5.15). As the setup does not allow for the installation of a reference, the measurements are performed at OCV after 48 h periods at the respective current densities. However, also at open cell conditions contributions of both electrodes are detected. Thus, these measurements serve as an initial test to investigate the Cr-deposition behavior of symmetrical ESC half-cells. The samples are investigated under dry conditions, since humid air lead to strong signal disturbances.

For sample 9M0410 (A1), a decrease of the ohmic resistance can be observed for higher overpotentials (OCV: 701 mOhm.cm²; 1 A.cm^{-2}: 598 mOhm.cm²; Relative decrease of 14.7 %). The polarization resistance R_{pol} shows a difference of 33 mOhm.cm² between the initial measurement and the measurement after 48 h at an overpotential of 1 A.cm^{-2} (OCV: 85 mohm.cm²; 1 A.cm^{-2}: 52 mOhm.cm²; Relative decrease of 38.8 %). Furthermore, the curve progression in the low-frequency regime changes with applying higher current densities. In the case of sample 9M0409 (B1), an inconsistent behavior of the ohmic resistance can be determined as it decreases when applying an overpotential of 0.5 A.cm^{-2}. Nevertheless, by further increase of the overpotential also the R_{ohm} increases up to a value of 826 mOhm.cm^2 (48 h 1 A.cm^{-2}), which equals a relative increase of 17.7 % compared to the initial measurement. As already observed for sample 9M0410, strong changes of the

electrochemical behavior can be detected in the low-frequency regime when applying first overpotentials. Analogously, also a decrease of the R_{pol} by 72.3 % is revealed (OCV: 47 mOhm.cm^2; 1 A.cm^{-2}: 13 mOhm.cm^2). Contrary to 9M0410, the initial measurement after 48 h at OCV (red line) shows a strong variation of the curve progression.
Compared to anode-supported cell measurements, symmetrical electrolyte-supported cells show stronger dependencies of the applied overpotential, which are assumed to be advantageous as previous measurements indicated Cr-degradation to be favored under these conditions. Nevertheless, both samples cannot be used for an in-depth evaluation of the individual process related contributions since no reference electrode could be implemented. With its implementation it is possible to exclude even smallest influences of the second electrode (counter electrode) to the cell impedance and guarantee solely contributions of the Cr-exposed working electrode. To accomplish this goal, symmetrical electrolyte-supported half-cells are investigated in custom-built setups (see chapter 4.5.2).

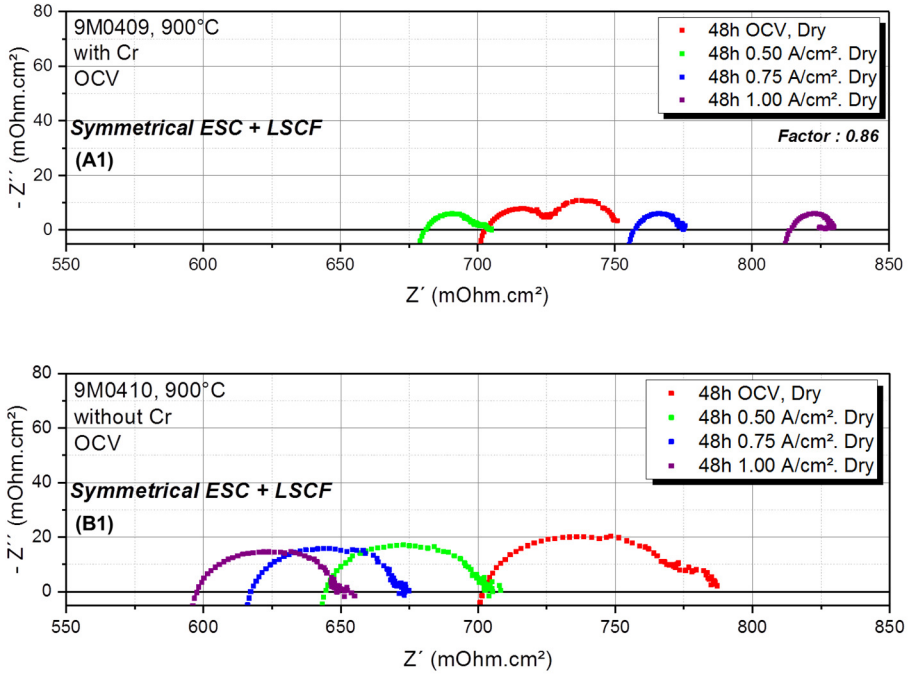

Figure 5.15: ESC-LSCF: Electrochemical impedance analysis of two different symmetrical electrolyte-supported samples (with an LSCF-cathode) operated at 900 °C for 48 h periods of various operating conditions (OCV, 0.75 A.cm^{-2}, 1 A.cm^{-2} and 2 A.cm^{-2}) in absence (A1) and presence of a Cr-source (B1) in dry atmospheres. The measurements are performed at OCV.

In order to prove whether observed electrochemical degradation trends can be attributed to the formation of Cr-species or simply to other degradation effects such as Ni-agglomeration, several post-test evaluation methods are established. These help to define the presence and oxidation states of deposited Cr-species as well as their influence on the cathode microstructure. Due to the large amount of samples, it has been mainly focused on the evaluation of Cr-exposed specimens.

5.1.5. ASC Post-Test Analysis

To confirm the presence of chrome and thus a successful poisoning of anode-supported SOFCs, all samples are investigated with help of XPS, ICP-OES and SEM. As only small amounts of Cr-deposits at the given operating conditions such as low gas-flow volumes and short operation times are presumed, less sensitive EDX and XRD-methods cannot be used. In Figure 5.16, the absolute Cr-content, which is measured with help of the ICP-OES method, is shown. As the Cr-content is determined in µg/g, it is normalized to the value of the actual sample and cathode-layer weight. A clear tendency towards a preferred poisoning at high temperatures (900 °C-800 °C) can be stated. At these temperatures, Cr-contents can be detected that are by a factor of 4-21 higher than observed for temperatures below 800 °C. As internal thermodynamic calculations revealed that the formation of any relevant Cr-species is related to an exergonic reaction [74], a far more decisive role can be attributed to the Cr-partial pressure difference between high and low operating temperatures. In this case, higher operating temperatures lead to stronger evaporation of gaseous Cr(VI)-species from the interconnect material into the gas chamber.

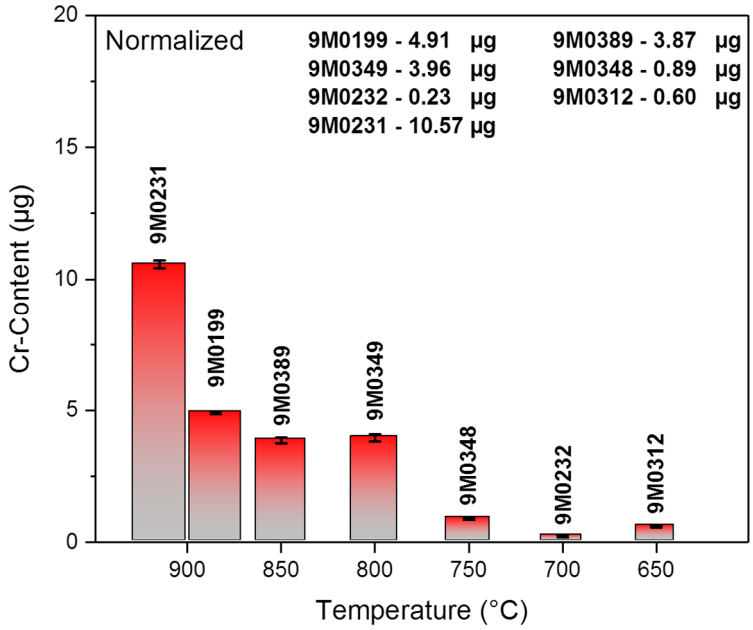

Figure 5.16: ICP-OES measurements of all Cr-exposed anode-supported SOFC samples. The values are normalized to the respective weight of the sample and cathode-layer.

Figure 5.17 shows the XPS focus points (number 1-4) of two different ASC-specimens operated at 900 °C. Sample (A) is measured in accordance with the established measurement schedule for ASCs with varying humidity and overpotentials (see chapter 4.5.1), whereas sample (B) is operated for 336 h (14 days) at a constant current density of 2 $A.cm^{-2}$. Furthermore, (A) shows strong cathode and barrier-layer delamination after operation. Only small fractions of the LSCF-cathode are left at the edges of the printing area (close to point 2). Due to this coincident, it is possible to detect the chemical composition at the former triple-phase boundary (dark grey colored area) with focus on the oxidation state of Cr-deposits in

this region. The rest of the former electrochemical active region can be identified as the 8YSZ electrolyte.

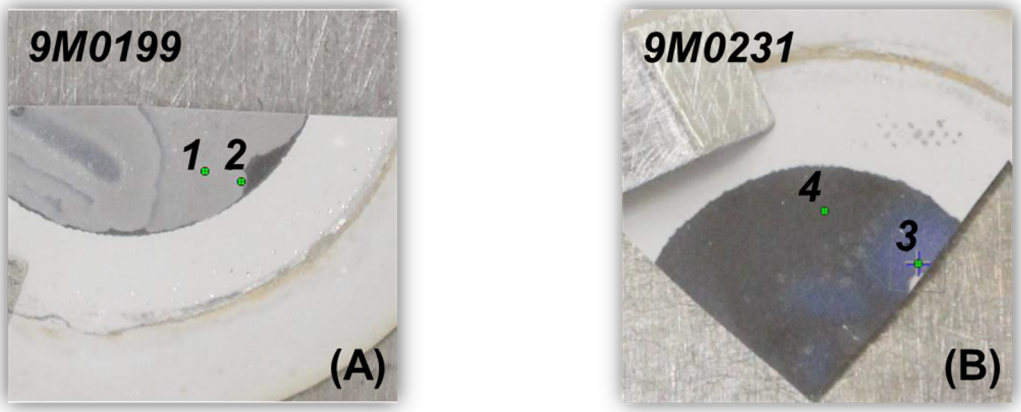

Figure 5.17: XPS focus points (1-4) of two ASC-specimen operated at 900 °C: (A) Sample operated in accordance with the ASC-measurement schedule; (B) Sample operated for 336 h (14 days) at a constant current density of 2 $A.cm^{-2}$.

The XPS-spectra, represented in Figure 5.18, reveal the chemical composition of samples (A) and (B) at the marked spots. Here, (1) describes the composition at the former triple-phase boundary or electrolyte. Even though most of the cathode and diffusion barrier layer delaminated, trace components of strontium (Sr), iron (Fe) and cerium (Ce) can be detected. However, the strongest signals within this scan can be clearly attributed to the elements yttrium (Y), zircon (Zr), oxygen (O) as well as carbon impurities (C). Besides, also the chrome Cr 2p3-peak at binding energies between 582-573 eV can be detected. In comparison to the other signals, the Cr-peak represents 0.7 At.% of the sum of all detected elements, indicating only small amounts of Cr-deposits. Nevertheless, more chrome than iron or cerium is detected. Also in (2), the presence of Cr-deposits can be confirmed. On the one hand, the chrome signal shows the lowest contribution to the cathode spectrum compared to other cathode-related detected elements. On the other hand, the quantity of the Cr-signal (1.4 At%) indicates a stronger deposition behavior on top of the LSCF-cathode than at the triple-phase boundary.

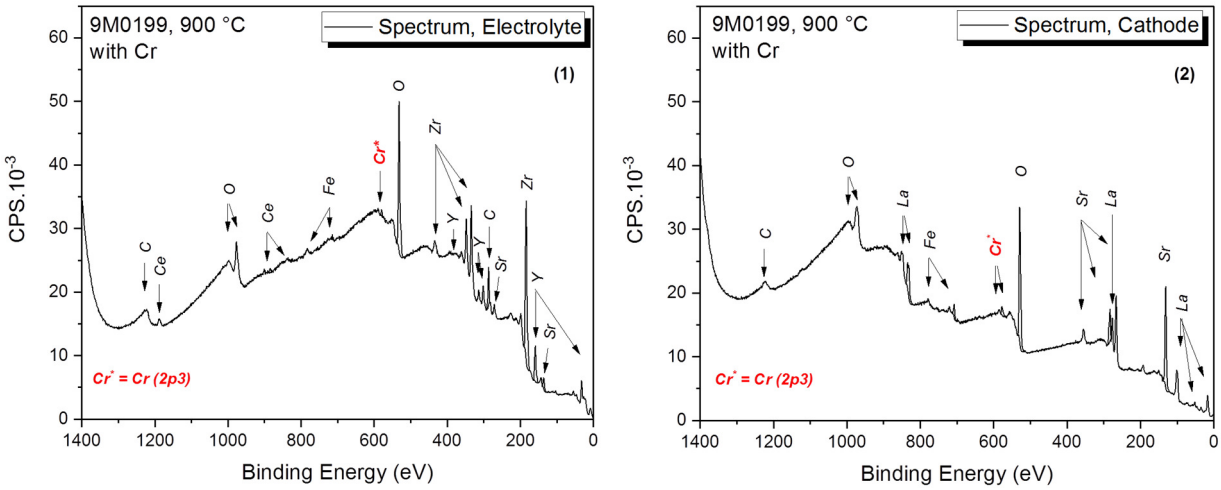

Figure 5.18: XPS-spectra of the elemental composition of an anode-supported SOFC operated at various current densities at (A) the former triple-phase boundary and (B) the LSCF-cathode surface.

An in-depth analysis of the Sr-signals (top) and Cr-signals (bottom) of both XPS-spectra (electrolyte and cathode) are illustrated in Figure 5.19. As it is known that mobile SrO-phases serve as precursors in the formation of $Sr_yCr_xO_z$-species, the identification of both signals is of great importance. The general Sr-peak at binding energies between 138-131 eV reveals the presence of three different Sr-species. Two of the three species are clearly identified as Sr-related signals (marked in dark blue and light blue). The third species that has been solely measured on top of the LSCF-cathode with binding energies of 131.7 eV and 133.5 eV (marked in red) could not be identified with help of relevant XPS databases and/or literature values. Furthermore, Figure 5.19 also reveals the presence of two different Cr-signals. Here, Cr(III)-species are detected at the former triple-phase boundary as well as on the cathode surface. Additional to these findings, a Cr(VI)-signal is detected on the cathode surface representing 16.8 % of the overall Cr-peak (also marked in red). Together with the unknown Sr-signal, the formation of $SrCrO_4$ particles on the cathode surface is most likely.

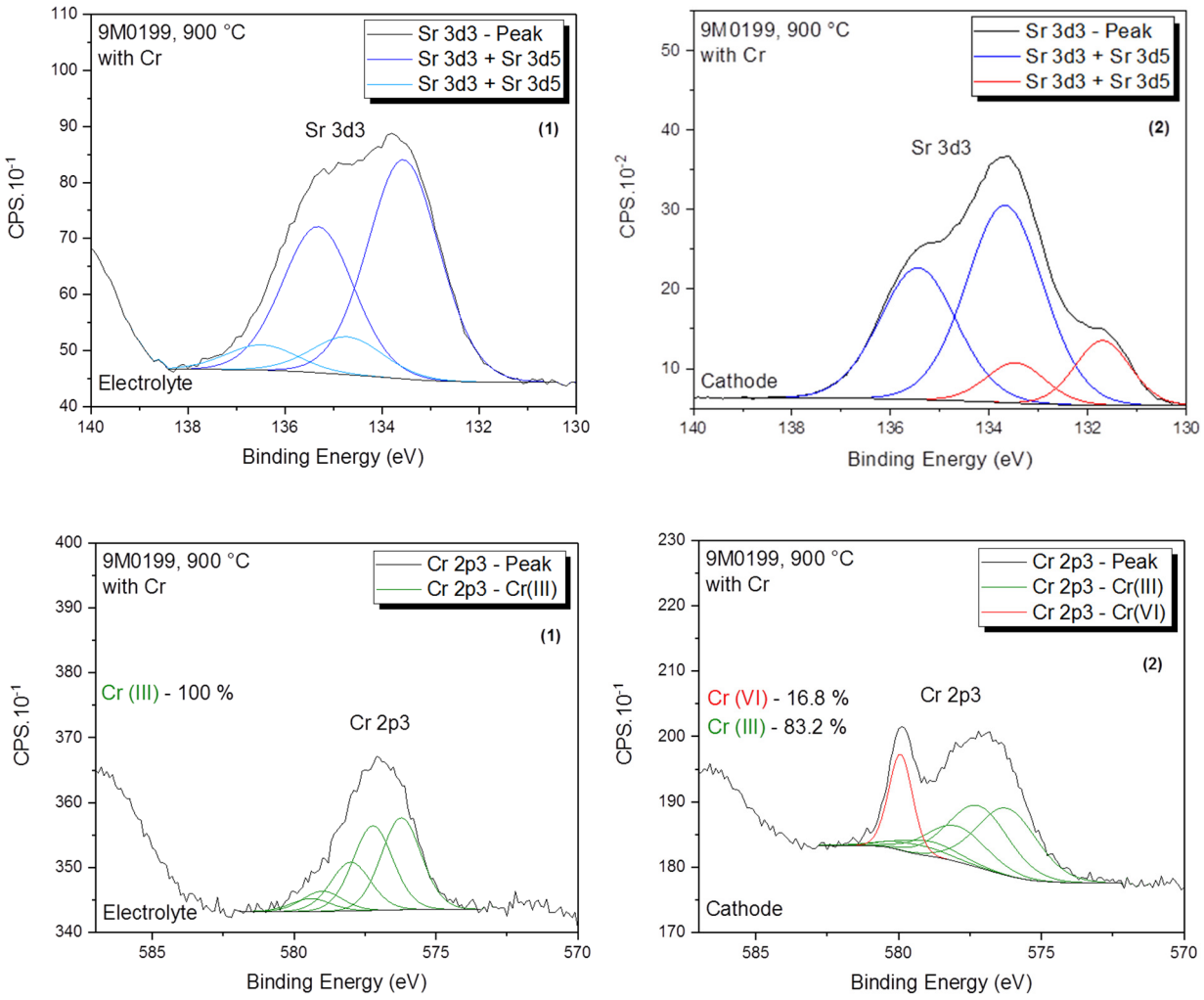

Figure 5.19: XPS in-depth analysis of occurring Sr-signals (top) and Cr-signals (bottom) of both electrolyte (former TPB) and cathode surface.

To confirm the presence of Cr(III) and Cr(VI)-species and exclude possible influences caused by cathode delamination, the measurements are repeated at a constant high current density of 2 A.cm^{-2} for 336 h (14 days). Figure 5.17 (B) already depicted the respective ASC after operation. In this case, the two interesting focus points (3) and (4), referred to as cathode blue and cathode black, are investigated (see Figure 5.20). It can be stated that Cr-deposits can be exclusively detected for the "black" spectrum (4). However, in comparison to the completely delaminated cathode in (1), strong signals of cathode related elements as La, Sr, Co and Fe can be detected within the "blue" spectrum (3). For this reason, one can assume slight cathode surface delamination by removal of the current collector, causing these "blue" spots.

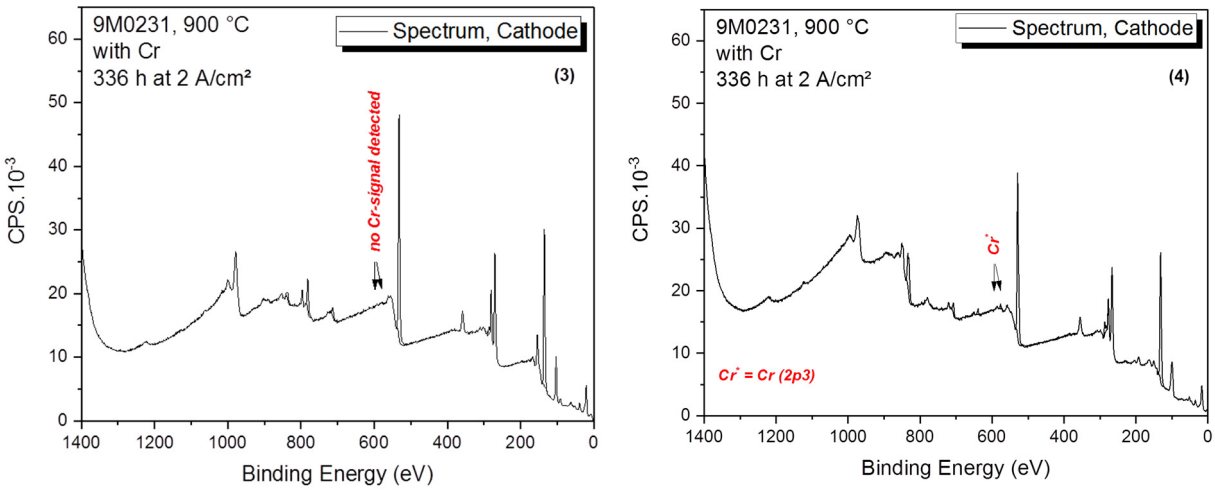

Figure 5.20: XPS-spectra of the elemental composition of an anode-supported SOFC operated at a constant current density of 2 A.cm^{-2} at two different spots on the LSCF-cathode surface.

Since no Cr-species could be detected by analyzing spot (3), in-depth evaluation of Sr and Cr-species is only performed for spot (4, cathode black). Also in this case, two different Cr as well as three different Sr-species are identified (see Figure 5.21). Apart from Cr(III), also the presence of a Cr(VI)-species and the unknown Sr-signal are detected. Here, the Cr(VI)-signal represents 34.5 % of the overall Cr-peak indicating an increase of 17.7 % in comparison to the respective signal detected for a sample operated at various lower current densities according to the measurement schedule. It is shown that the formation of $SrCrO_4$-species is highly affected by increasing the current density and, thus, also the cathodic overpotential. However, an influence of the accompanied rise of the local temperature at the electrochemically active area cannot be excluded.

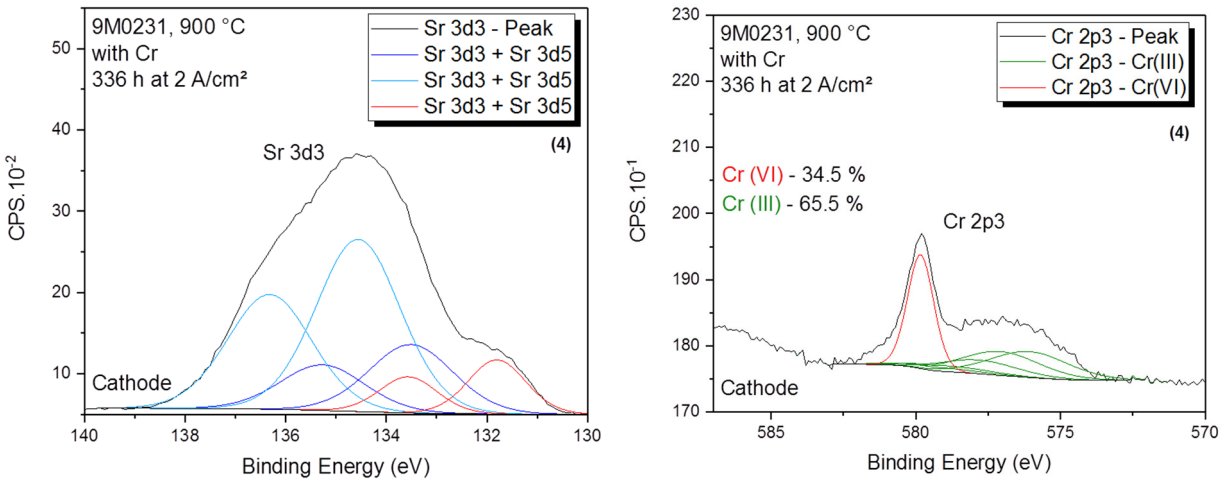

Figure 5.21: XPS in-depth analysis of occurring Cr-signals (left) and Sr-signals (right) of spectrum (4) which is assigned to the cathode surface "black".

The presence of Cr and Sr-species is also determined for operating temperatures from 850 °C-650 °C (steps: 50 °C). As the connection between both signals can be detected analogously to the findings at 900 °C, it has been mainly focused on the analysis of the

Cr-related signals (Figure 5.22). The results show the appearance of both, Cr(III) and Cr(VI)-signals, for operating temperatures of 850 °C, 750 °C and 650 °C. However, no Cr-signals have been detected for 800 °C and 700 °C. At least for a temperature of 800 °C, the XPS-results are contradictory to the outcome of the ICP-OES measurements as the second highest amount of Cr-deposits has been detected for these temperatures. On the other hand, since not the entire cathode surface is covered with Cr-species and the XPS method is related to a certain spot size, it is possible that measurements were performed on less poisoned surface regions. Due to a limited sensitivity of the XPS, these signals can hardly be detected. In contrast to the measurements at 900 °C (9M0199 and 9M0231), analysis of sample 9M0389 (850 °C) indicates a reduced Cr(VI)-signal. In this case, Cr(VI) only contributes with 2 % to the overall Cr-signal (16.8 % at 900 °C). This trend can also be confirmed for an operating temperature of 750 °C (9M0348) even though the general signal-to-noise ratio decreases. For measurements at 650 °C, the ratio between actual signal and background noise is strongly reduced such that a quantitative analysis of the Cr-species is no longer valid.

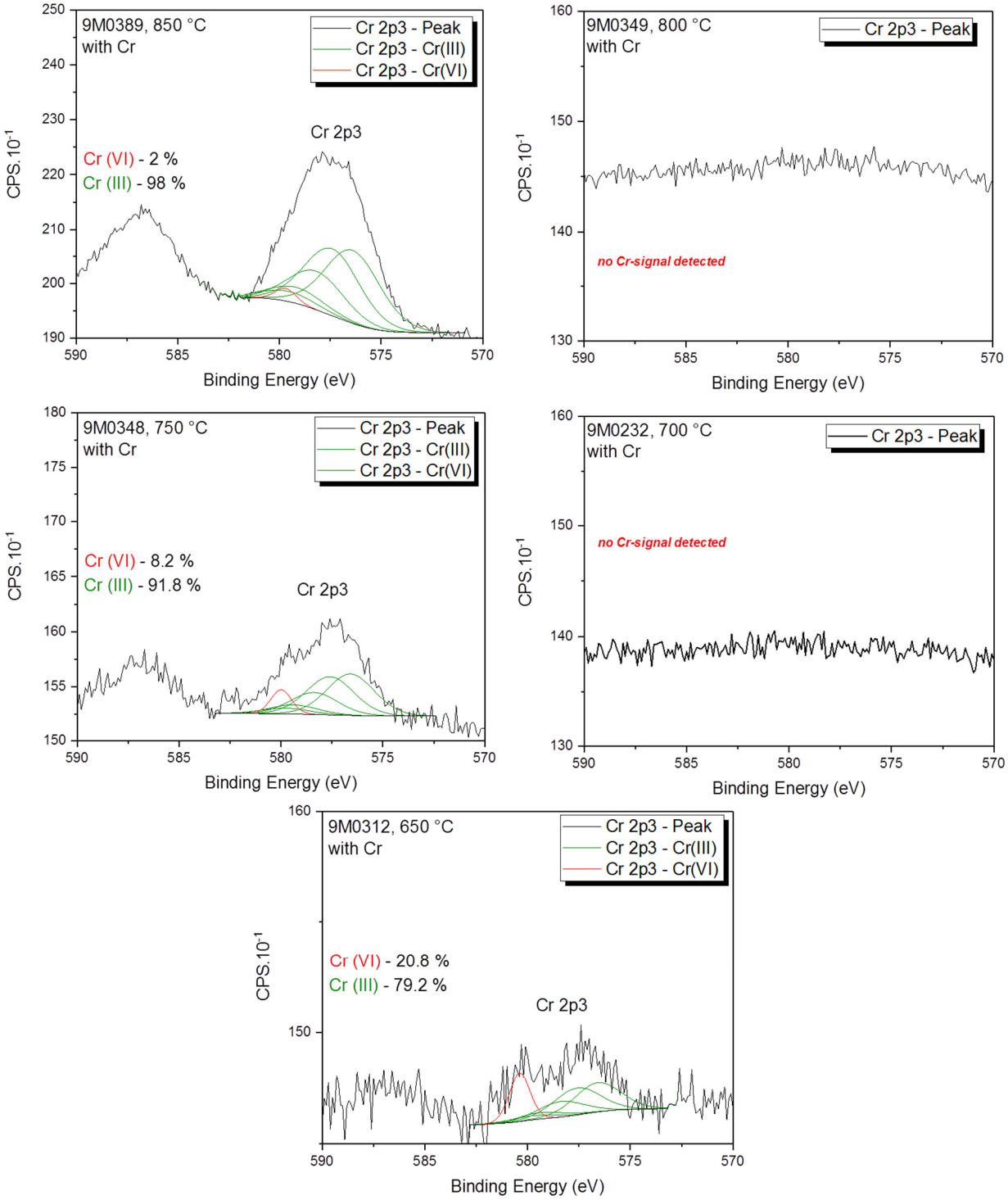

Figure 5.22: XPS in-depth analysis of occurring Cr-signals for operating temperatures of 850 °C-650 °C.

As already mentioned within the XPS-analysis, sample 9M0199 (900 °C) showed strong cathode delamination. Unfortunately, after XPS-treatment, no cathode traces could be detected, preventing further microscopic SEM measurements. For this reason, sample 9M0231, which has been exposed to chrome at 900 °C at a current density of 2 A.cm^{-2}, is utilized. As the XPS-procedure already revealed a similar Cr-deposition behavior, sample 9M0231 can be seen as an adequate alternative. Figure 5.23 reveals the microscopic nature of the sample by utilization of cathodic top-views and magnifications of 3000x (left) and

5000x (right). In contrast to previously characterized anode-supported SOFCs (before Cr-treatment), a strong densification of the formerly porous cell structure can be detected. Here, an almost dense layer on top of the cathode grains is illustrated. In synergy to the XPS-data, the layer is assumed to be $SrCrO_4$.

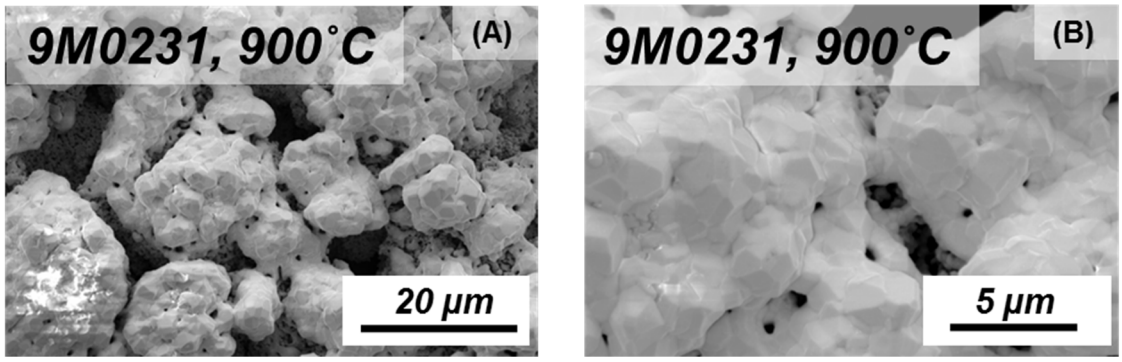

Figure 5.23: SEM tow-view images with a magnification of 3000x (A) and 10000x (B) of sample 9M0231 which is exposed to chrome for 336 h (14 days) at a current density of 2 $A.cm^{-2}$ under humid conditions.

Figure 5.24 illustrates a similar surface structure of samples measured at 850 °C (9M0389) and 800 °C (9M0349) according to the ASC measuring schedule. For both samples, less porous cathode surface structures as compared to the initial non-exposed samples are shown. Furthermore, a trend towards the formation of these phases with increasing the operating temperature can be confirmed. However, in contrast to cell 9M0231, no completely dense grain covering layers can be observed.

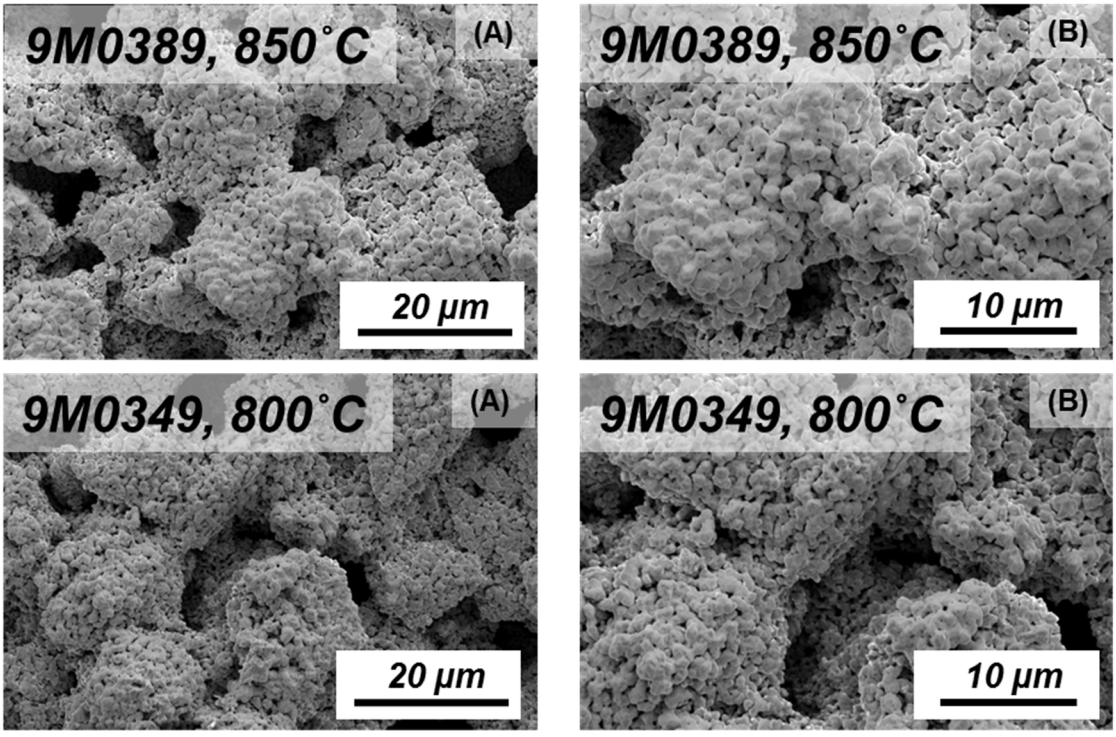

Figure 5.24: SEM top-view images with a magnification of 3000x (A) and 5000x (B) of samples 9M0389 and 9M0349 which are exposed to chrome at operating temperatures of 850 °C and 800 °C according to the ASC measuring schedule.

For samples operated at temperatures of 750 °C, 700 °C and 650 °C, the initial porous structure of the cathode material remains nearly unchanged (Figure 5.25). As already shown for the ICP-OES measurements, a considerably lower amount of Cr-species has been found for these cells. Even though their Cr-content differs, no content related structural changes of the cathode surface can be observed.

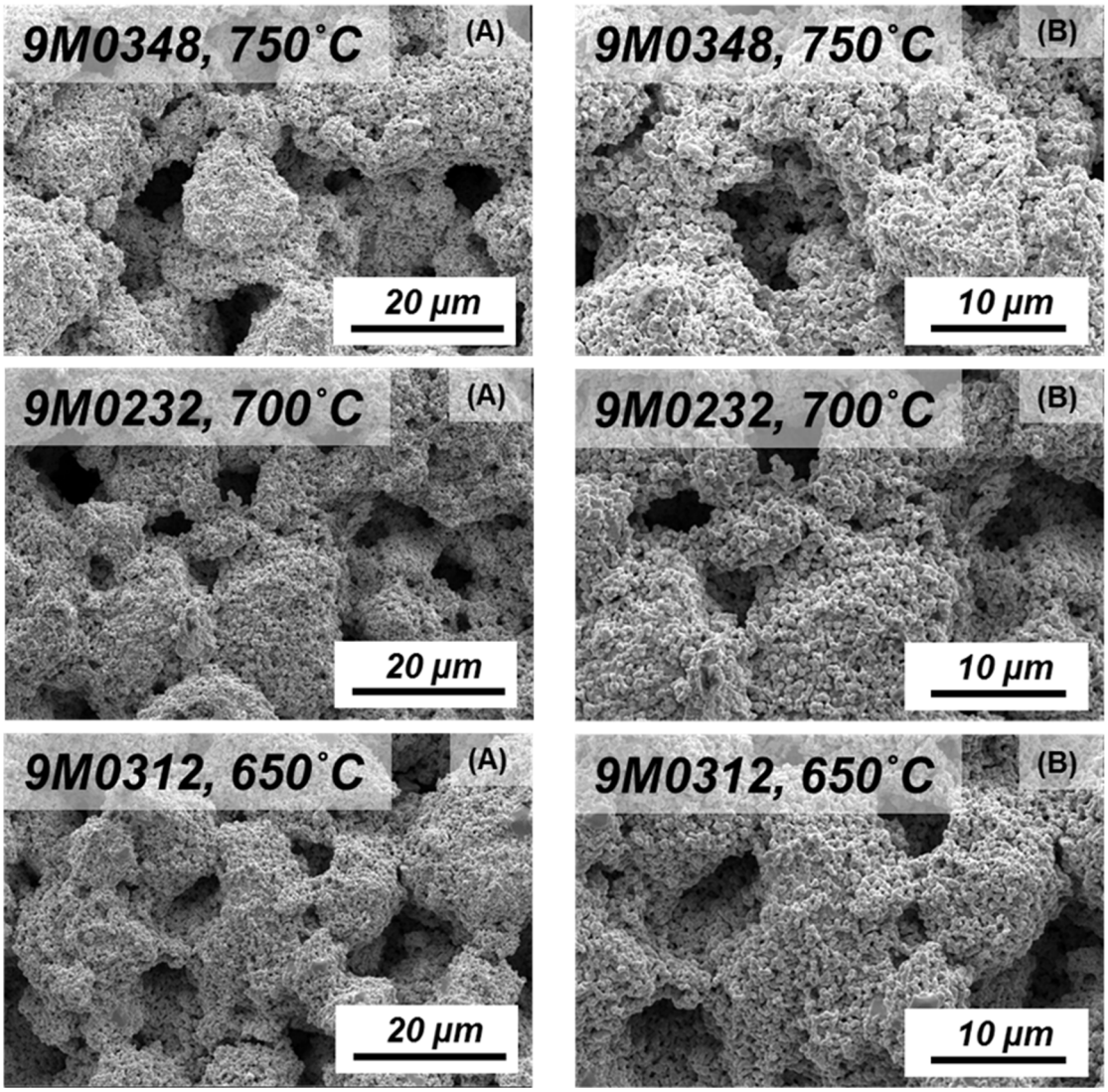

Figure 5.25: SEM top-view images with a magnification of 3000x (A) and 5000x (B) of samples 9M0348, 9M0232 and 9M0312 which are exposed to chrome at operating temperatures of 750 °C, 700 °C and 650 °C according to the ASC measuring schedule.

With the post-test analysis of Cr-exposed anode-supported SOFCs, the presence of Cr-species within the systems has been explicitly confirmed. In this regard, a clear tendency towards an enhanced Cr-deposition at operating temperatures above 750 °C is shown. Furthermore, the presence of both Cr(III) and Cr(VI)-species on the LSCF surface and solely Cr(III) at the TPB is observed. In correlation to the detected Sr-signals, the presence of $SrCrO_4$ on top of the electrode is proven. It can be also stated that measurements performed at high current densities (2 $A.cm^{-2}$) lead to a stronger appearance of that phase. Nevertheless, since the formation of $SrCrO_4$ on the LSCF-surface is assumed to follow a chemical mechanism, no current density related influences should be observed. For strongly poisoned cells, (preferably

at high operating temperatures) a padding of the initial porosity, leading to dense grain structures, is revealed.
With regard to the post-test analysis of anode-supported SOFCs with a LSCF cathode, one can assume process related resistance changes and degradation tendencies below operating temperatures of 800 °C most likely not to be influenced by the presence of Cr-species on top of the LSCF-surface. Also within the analysis of SEM cross-sections (not depicted in here) no Cr-species could have been detected close to the TPB. However, as the presence of Cr(III)-species at the TPB has been stated for 900 °C (see XPS-analysis of sample 9M0199), images of cross-sections might lead to misinterpretations. In this case embedding and polishing of the samples could have led to the removal of Cr-deposits.

To prove or disprove the experimental findings for anode-supported SOFCs, further information about cathode processes and their dependencies regarding chrome and other operational parameters are provided within the analysis of symmetrical electrolyte-supported SOFCs (half-cells) in the following chapters.

5.2. *Electrolyte-supported SOFC characterization*

Besides anode-supported SOFCs (full-cells) also electrolyte supported SOFCs (half-cells) with cathode variations are utilized. This allows for an in-depth investigation and separation of cathode related degradation processes which can be assigned to the presence of chrome. As these required cell compositions are not commercially available, a suitable production route has to be established.

5.2.1. ESC Cathode Development & Pre-Test Characterization

Within the following chapter the development of suitable LSF, LSCF and LSC cathode materials is presented. After each step in the production route, the synthesized powders are characterized to ensure consistent conditions such as the particle size distribution and the microscopic structure.

Cathode powders

In a first step, the cathode materials $La_{0.58}Sr_{0.4}FeO_{3-\delta}$ (LSF, A), $La_{0.58}Sr_{0.4}Co_{0.2}Fe_{0.8}O_{3-\delta}$ (LSCF, B) and $La_{0.58}Sr_{0.4}CoO_{3-\delta}$ (LSC, C) are synthesized by the solid state synthesis procedure (see chapter 4.1). Figure 5.26 represents the XRD-pattern of all three synthesized powder materials after calcination. With help of appropriate references from the ICSD-database it is possible to confirm successful synthesis of the desired powder stoichiometries. The XRD-pattern also reveals stronger shoulder formations and peak broadening effects for LSF than observed for LSCF and LSC-powders.

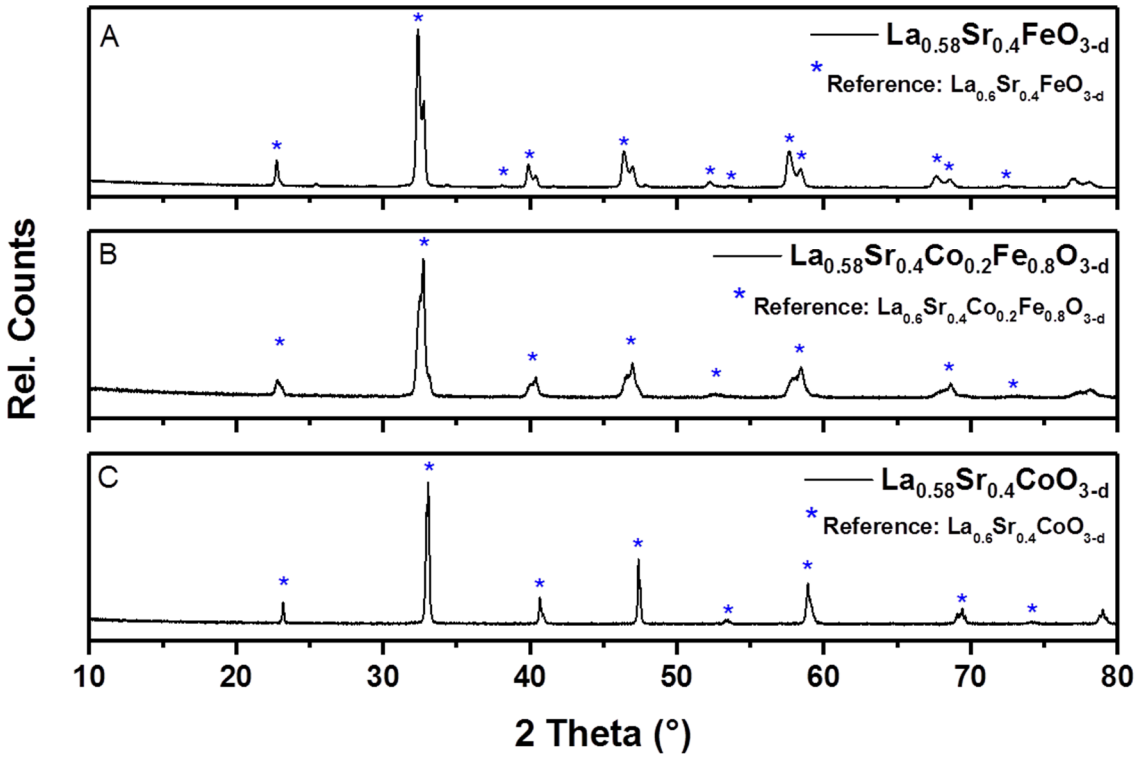

Figure 5.26: XRD-pattern of the synthesized materials LSF (A), LSCF (B) and LSC (C).

Figure 5.27 depicts the respective powder materials with magnifications of 1000x (A) and 10000x (B). By comparison of the powders at a magnification of 1000x a stronger agglomeration tendency with increasing Co-content can be observed. Increasing the magnification to a value of 10000x revealed a homogenous particle size distribution for LSC powders. However, additional particle size distribution measurements (in isopropanol after ultrasonic treatment) indicated a mean particle size (d_{50}) of 1.8–2.7 µm for all powders. Although best cathode performances are obtained at a d_{50} of 0.7-0.8 µm, an average distribution of 2.3 µm can be considered to be adequate to obtain a more localized Cr-poisoning due to higher local current densities (by consistent geometrical current densities).

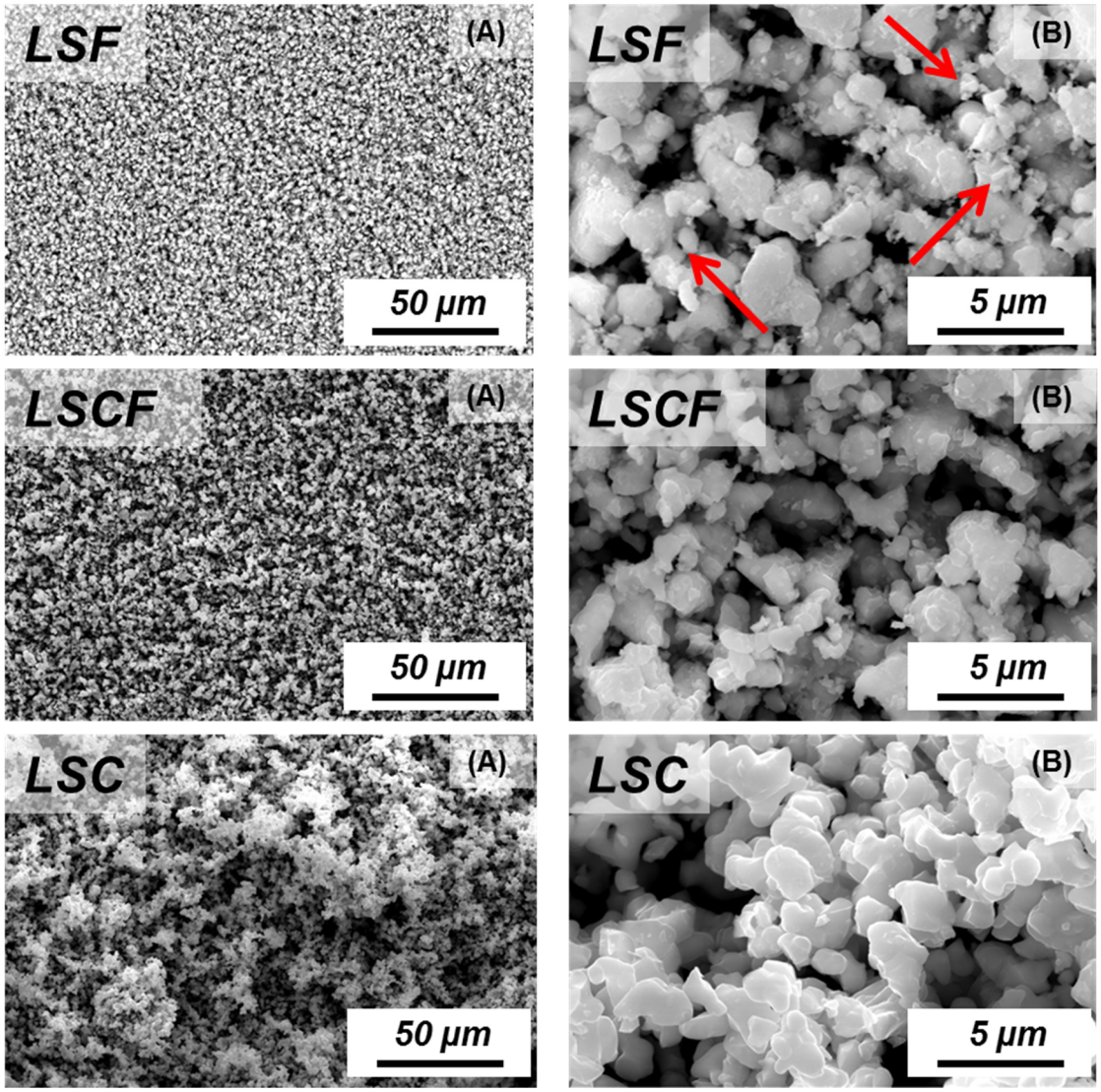

Figure 5.27: SEM top-view images of the synthesized, calcined and re-milled LSF, LSCF and LSF cathode powders at magnifications of (A) 1000x and (B) 10000x.

Even though the synthesized powders can be clearly identified by XRD (when combined with the ICSD-database), the spectra of LSF powders show features (marked with **red-arrows**) that induced the need to perform a Rietveld-refinement of the experimentally determined diffraction pattern (Figure 5.28). The refinement reveals the presence of a rhombohedral

(Pbnm crystal lattice) as well as an orthorhombic phase (R-3C crystal lattice). An exemplary peak-magnification at a phase angle of 33 ° shows the occurrence of both phases. As this trend can be observed for most of the identified signals, phase contributions of 66 % for the rhombohedral and 33 % of the orthorhombic phase have been calculated.

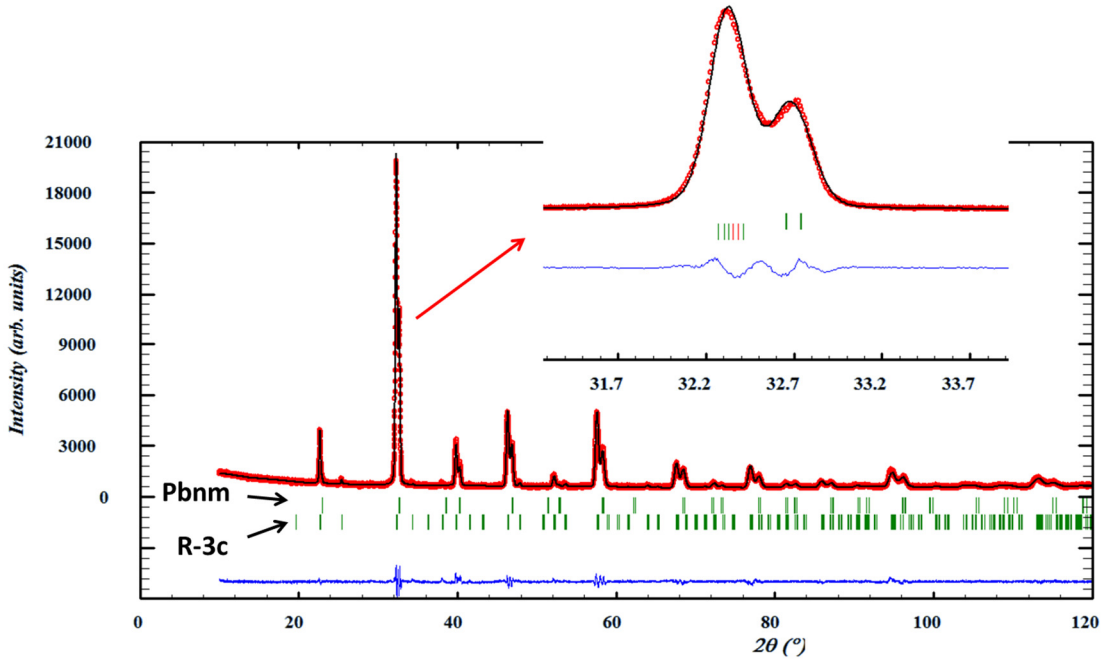

Figure 5.28: Fullprof-refinement (i.e. Rietveld-refinement) of $La_{0.58}Sr_{0.4}FeO_{3-\delta}$ (LSF), revealing the presence of a rhombohedral and an orthorhombic phase. Performed and plotted by Dr. Vaibhav Vibhu (IEK-9).

Cathode pastes

The second step in the production route of symmetrical electrolyte supported SOFCs is the production of suitable screen printing pastes (see chapter 4.2). Since the adapted powders are mixed with ethyl cellulose (incl. a binder), re-agglomeration of powder particles can occur. Figure 5.29 presents the final particle size distributions of all three pastes after an additional milling step. The results confirm a monomodal distribution of the particle sizes within each paste. A monomodal distribution is one of the key factors to guarantee a homogenous printing image during screen-printing and thus is essential for the production of suitable ESCs.
The d_{50}-values indicate an average particle size of 2.27 µm for LSF, 2.33 µm for LSCF and 2.38 µm for LSC. Furthermore, LSF-pastes show a less homogenous particle size distribution (LSF: 0.4-9 µm, LSCF and LSC: 0.6-7 µm). In comparison to the mean particle size distribution of the pure powders (1.8 µm for LSC, 2.3 µm for LSCF and 2.7 µm for LSF) only the particle size of LSCF remains constant within the paste production procedure. In contrast to LSCF, the particle size distribution of LSC increased (re-agglomeration) whereas it decreased for LSF. However, the pastes can be utilized for the deposition of comparable cathode layers as they show similar median particle sizes (~ 2.3 µm) and viscosities.

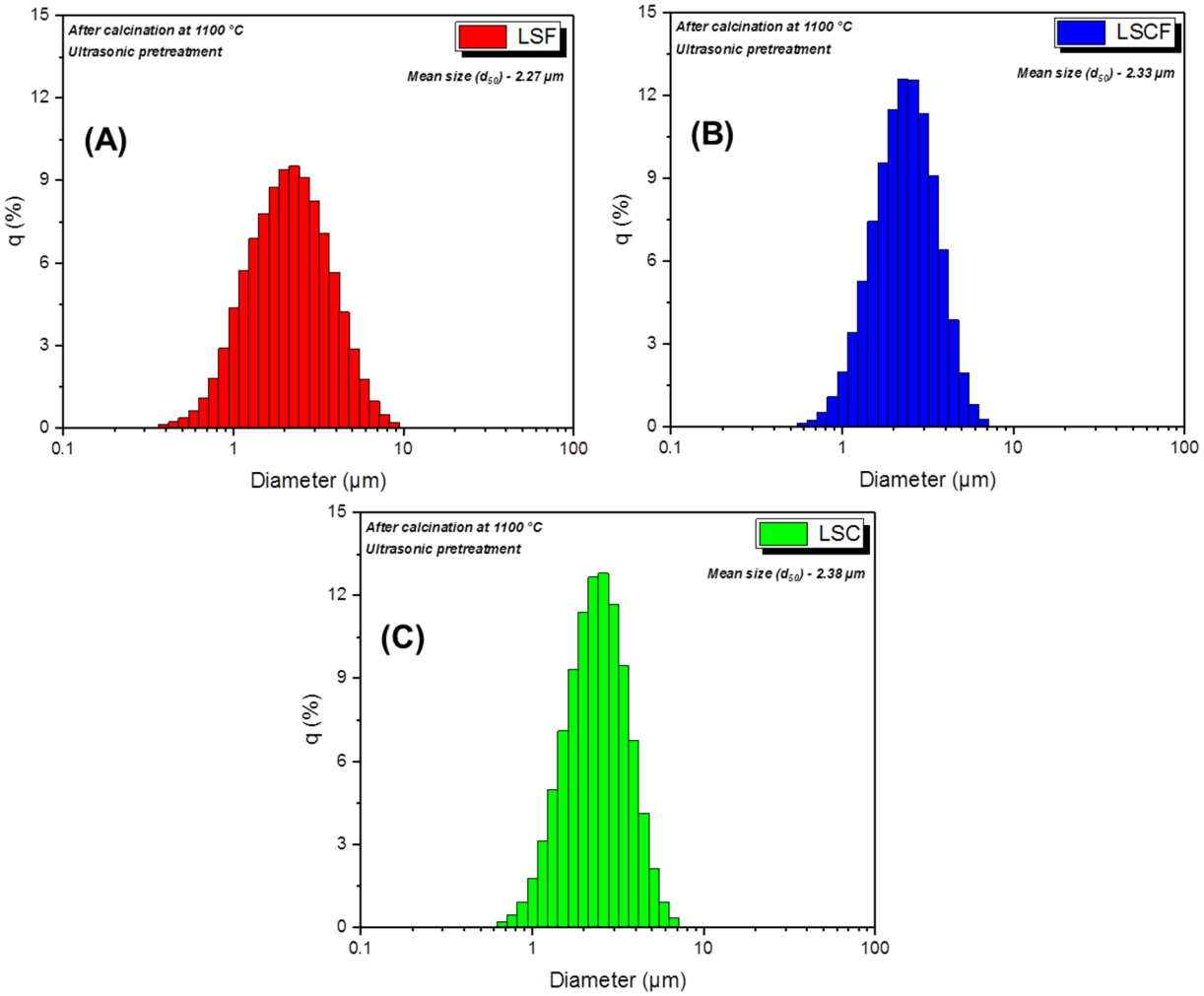

Figure 5.29: Particle size distribution (incl. d_{50}-value) after the production of LSF (A), LSCF (B) and LSC (C) pastes.

Screen-printed electrodes

After screen-printing of the individual cathode pastes onto both sides of the commercially available electrolyte/barrier layer substrates, the cells are sintered for 3 h at a temperature of 1080 °C. In Figure 5.30 electrolyte-supported half-cells equipped with LSF, LSCF or LSC-cathodes are shown (magnifications of (A) 3000x and (B) 5000x). It can be stated that the screen printing procedure leads to homogenously deposited cathode layers with an adequate thickness of 20-25 µm. Furthermore, all samples show sufficient adhesion towards the diffusion barrier layer over the entire printed area. Also, no formation of a dense layer of less conductive Sr_2ZrO_4 -phases at the interface between electrolyte and diffusion barrier layer could be observed. All electrodes show similar layer-structures after being sintered, which is advantageous as structural impacts on the individual cell-electrochemistry can be neglected.

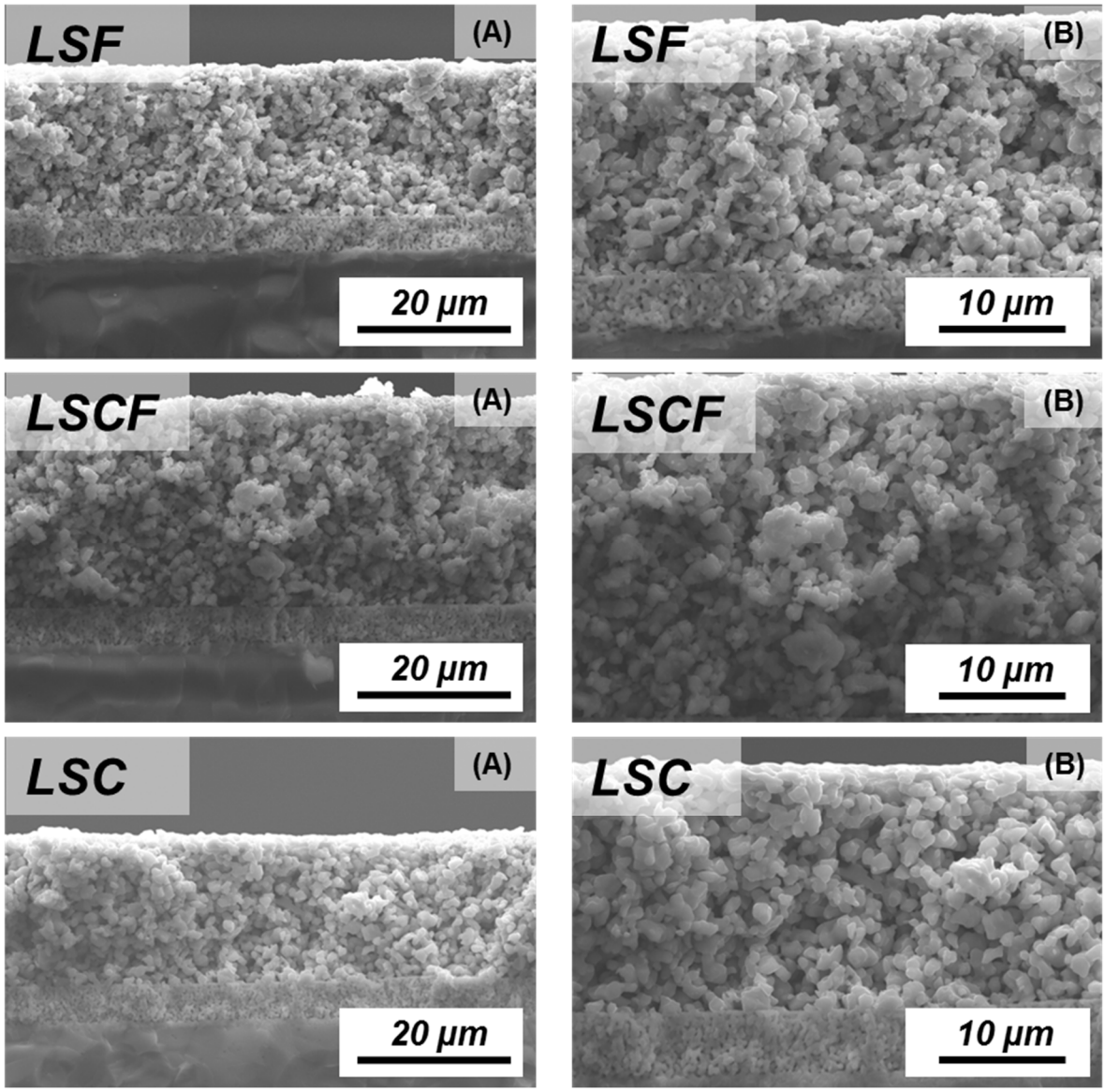

Figure 5.30: SEM cross-sections of symmetrical, electrolyte-supported SOFCs (half-cells) with screen printed LSF, LSCF and LSC-cathodes with magnifications of (A) 3000x and (B) 5000x.

An exemplary EDX-pattern of the LSCF cathode is shown in Figure 5.31. The pattern represents the elemental distribution of lanthanum (La), strontium (Sr), cobalt (Co) and iron (Fe) within the deposited cathode material. The presence of all four elements, which are homogenously distributed across the entire cathode, can be confirmed. Furthermore, no other elements such as cerium (Ce), gadolinium (Gd) from the diffusion barrier layer or chrome impurities (Cr) could be detected prior to the electrochemical characterization.

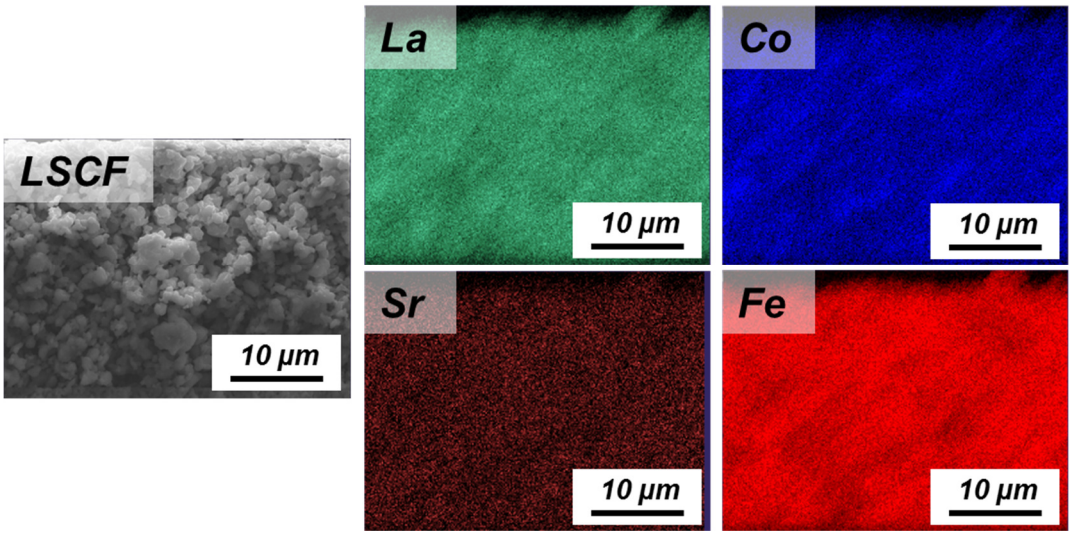

Figure 5.31: Exemplary EDX-pattern of a deposited LSCF-cathode incl. elemental distribution of lanthanum (La), strontium (Sr), cobalt (Co) and iron (Fe).

Since the produced symmetrical electrolyte-supported SOFC half-cells have been equipped with adequate LSCF, LSF and LSC cathodes, it is possible to proceed with their electrochemical in-operando analysis. Here, due to adapted larger particle size distributions and the exclusion of any anode contributions, detailed information about the Cr-poisoning procedure can be collected.

5.2.2. Electrochemical In-Operando Analysis of ESCs: AC-Characterization

Continuing with the analysis of LSCF-cathodes, Figure 5.32 illustrates the electrochemical response of a symmetrical ESC system for dry (A1/B1) and humid air conditions (A2/B2) in the absence (top) and presence of Crofer 22 H (bottom). Here, the already mentioned 3-electrode setup together with a Pt-reference electrode is utilized (see chapter 4.5.2). All measurements are performed in air (dry/humidified) at operating temperatures of 900 °C. As a symmetrical cell setup with two cathodes is utilized, no hydrogen has to be used. Analogously to ASC measurements, ESCs are measured after 48 h periods of constantly applied electrical loads (OCV, 0.75 $A.cm^{-2}$, 1 $A.cm^{-2}$and 2 $A.cm^{-2}$). Since no anode material is utilized, higher local cathodic overpotentials can be assumed. To guarantee comparable measuring conditions and a sufficient signal-to-noise ratio, all measurements are performed at a constant overpotential of 0.2 V vs. a Pt-reference (potentiostatic conditions). As measurements are conducted in the presence of a Pt-reference electrode, ohmic resistances cannot be considered for the in-depth evaluation. In fact, the R_{ohm}-values show strong variations between the measurements. This phenomenon can be explained due to current induced, varying potential lines that are measured between working and reference electrode. Furthermore, measurements in the absence of a Cr-source show strong capacitive effects for dry conditions in the high-frequency range. As these points cannot be calculated according to the Kramers-Kronig relations (KK-relations), making adequate evaluation or subtraction impossible, they are excluded from the analysis.
However, both, measurements in absence (sample 9M0216) and presence of a Cr-source (sample 9M0214), reveal uniform trends in their curve progression and thus also in their

electrochemical behavior. The polarization resistances for sample 9M0216 increase from a value of 55 mOhm.cm² for the initial measurement (48 h OCV, dry; A1), to a value of 80 mOhm.cm² after the final measurements (48 h 2 A.cm⁻², humid; A2). Here, the strongest increases are shown in humid cathode-gas atmospheres.
In case of sample 9M0214, which is exposed to chrome, the polarization resistances develop from an initial resistance value of 140 mOhm.cm² (B1) to a final value of 139 mOhm.cm² (B2) indicating no electrochemically observable degradation tendency of the total polarization resistance.

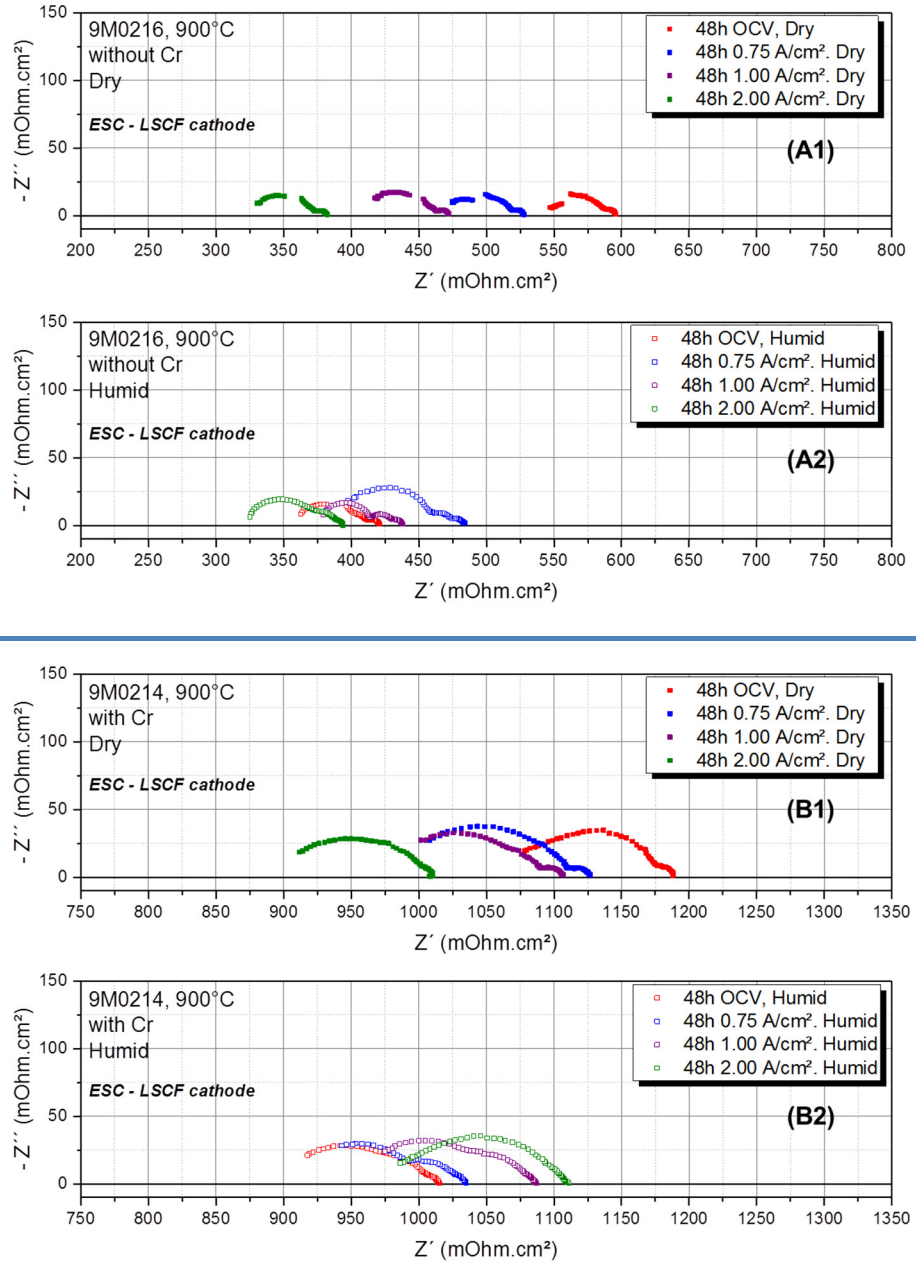

Figure 5.32: Electrochemical impedance characterization of symmetrical, electrolyte-supported SOFCs, equipped with a LSCF-cathode, at a fixed overpotential of 0.2 V after 48 h periods of various operating conditions for two different samples operated at 900 °C in absence (A1/A2) and presence of a Cr-source (B1/B2).

In order to investigate the Cr-deposition behavior on the B-site stoichiometry and thus the content of cobalt and iron within the specimen, samples equipped with LSF and

LSC-cathodes have been analyzed. Here, the cells are treated according to the measurements of ESC half-cells comprising LSCF-cathodes.
Within the measurements of sample 9M0217 (LSF), increased capacitances in the mid-frequency range (A1) as well as strong inductances in the low-frequency regime (B1) can be observed (Figure 5.33). The curves show equal tendencies in their electrochemical response, as seen for sample 9M0215 which is operated in the presence of a Cr-source. However, as the data quality is insufficient, these measurements in absence of chrome cannot be consulted for an in-depth process evaluation.
For sample 9M0215 (LSF), distinct degradation tendencies can be clearly stated. The R_{pol} increases from initial 52 mOhm.cm² (B1) to a final value of 165 mOhm.cm² (B2) after extrapolation. Here, also a change in the curve progression at higher overpotentials (> 0.75 $A.cm^{-2}$) for both, dry and humid conditions, is revealed. Furthermore, a strong increase of the capacity after a 48 h period at a constant overpotential of 2 $A.cm^{-2}$ is shown.

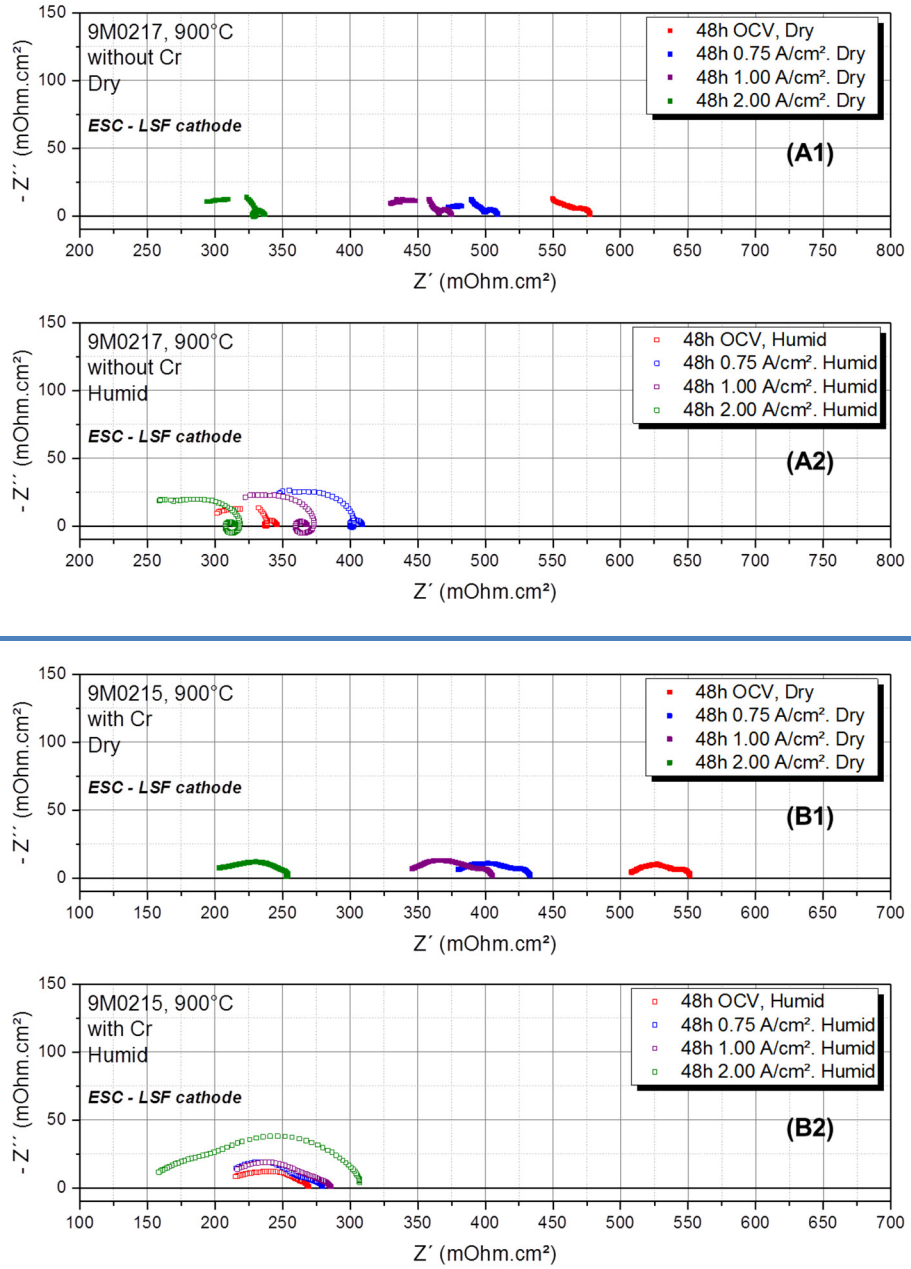

Figure 5.33: Electrochemical impedance characterization of symmetrical, electrolyte-supported SOFCs, equipped with a LSF-cathode, at a fixed overpotential of 0.2 V after 48 h periods of various operating conditions for two different samples operated at 900 °C in absence (A1/A2) and presence of a Cr-source (B1/B2).

As already shown for electrochemical impedance characterization of symmetrical ESCs with LSF-cathodes, also measurements of LSC-cells in the absence of Cr (sample 9M0000, A1 and A2) show strong inductivities in combination with data loops in the low-frequency regime (Figure 5.34). As only small parts of the curves and, thus, a small amount of data points can be calculated according to Kramers-Kronig, it cannot be focused on their analysis. Measurements of sample 9M0001, however, provide sufficient and reproducible data points which can be further analyzed. Here, again, a strong capacitive behavior of data in the high-frequency regime can be stated. By extrapolation of the experimental data, a decrease of the polarization resistance by a value of 24 mOhm.cm² is detected (Initial: 62 mOhm.cm², B1; Final: 38 mOhm.cm², B2). It should be pointed out that the R_{pol} trend is not continuous, as

with the introduction of humidity also the resistances increase up to a value of 73 mOhm.cm² (48 h at 0.75 A.cm^{-2}, humid).

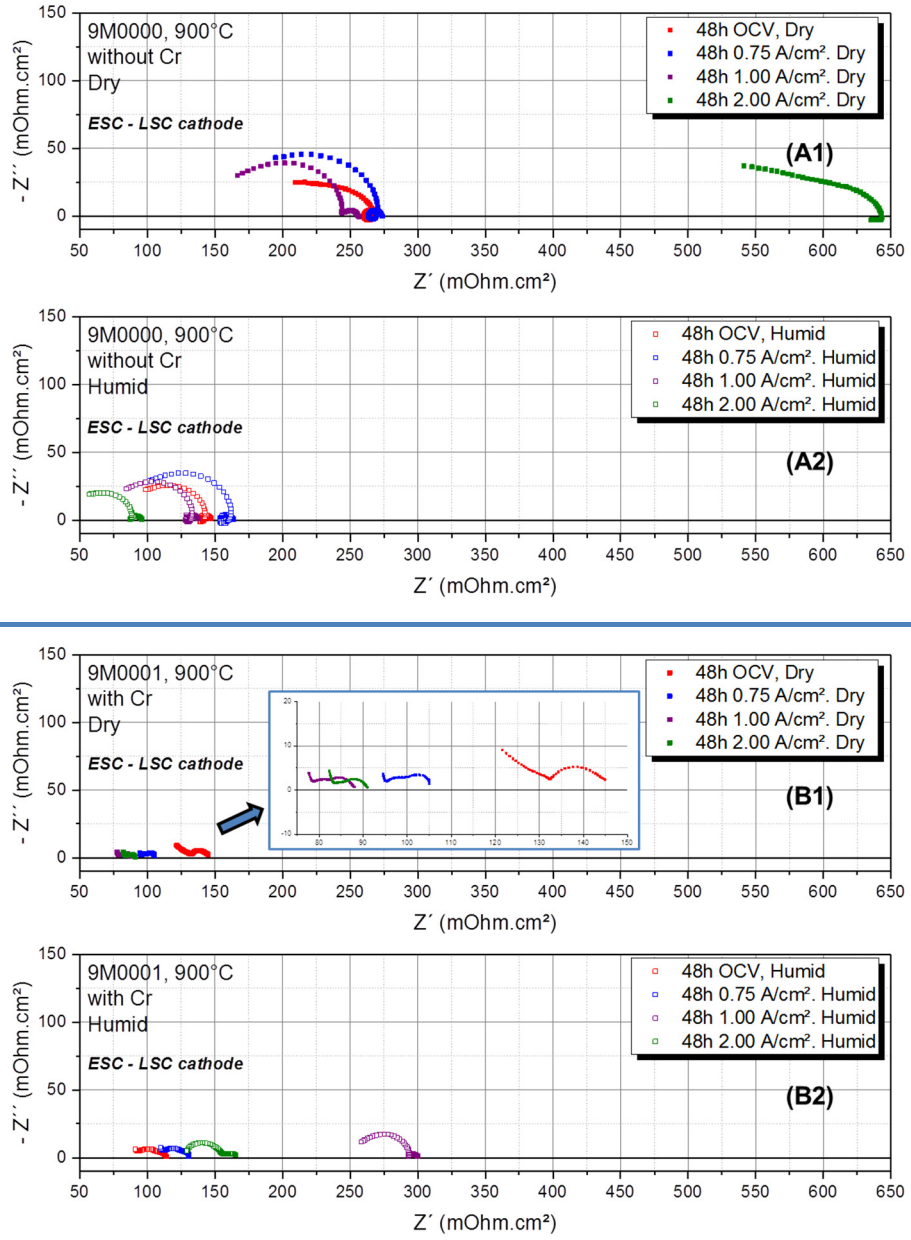

Figure 5.34: Electrochemical impedance characterization of symmetrical, electrolyte-supported SOFCs, equipped with a LSC-cathode, at a fixed overpotential of 0.2 V after 48 h periods of various operating conditions for two different samples operated at 900 °C in absence (A1/A2) and presence of a Cr-source (B1/B2).

The electrochemical raw-data of symmetrical electrolyte supported SOFCs does not reveal a clear and significant degradation trend for LSCF- and LSC-cathodes. Nevertheless, in case of LSCF and the absence of chrome, small increases of the polarization resistances can be observed (especially in humid air) whereas in its presence, neither in dry nor in humid atmospheres, degradation tendencies can be detected. Although the average particle size distribution of the printed LSCF-cathode has been increased to a value of 2.33 µm (standard 0.8 µm) and, thus, higher local current densities (i.e. higher overpotentials) are provided, no Cr-related degradation influences can be stated. For LSC-cathodes, the polarization

resistances even decrease with time and increasing cathode overpotentials. This finding is contradictory to what would be expected from a material with a high Co-content. Since cobalt is the electrochemically most active part in LSCF-cathodes, one would assume to find stronger degradation tendencies for pure LSC-cathodes in presence of chrome. Contrary to the experimental findings of LSCF- and LSC-materials, ESCs equipped with a LSF-cathode show explicit degradation tendencies in the presence of chrome.

5.2.3. Electrochemical In-Operando Analysis of ESCs: EC-Development

In order to fully understand the development of the general polarization resistances of those cells, the individual cathode process related contributions have to be identified and further quantified. Therefore, the equivalent circuit model shown in Figure 5.35 is developed. The model is based on the theoretical assumptions of the modified KIT-model for ASCs (see chapter 5.1.3) and is adapted for the description of cathode related processes in ESC systems. As the evaluated curves show no inductive effects in the low or high-frequency range (except for samples 9M0217 and 9M0000 which are not considered for in-depth characterization), test-rig related EC-elements do not have to be added. The model should describe the ohmic contribution (R1) and three cathode processes (G1, R2/CPE1 and R3/CPE2). As any contribution of anode related processes can be excluded and conducted measurements deny the presence of a Warburg-type element, it represents an inadequate description of the cell electrochemistry. For this reason and in accordance to the original KIT-model and the experimental data, the process of oxygen surface exchange kinetics can be assumed to be described by a Gerischer element. Furthermore, the exclusion of anode processes makes it possible to include two processes apart from the Gerischer element. In relation to the frequency range and the characteristic resistance-values, the processes can be identified as the oxygen-ion diffusivity in the cathode bulk as well as the gas diffusion process in the cathode structure (see Table 12).
Despite different B-site stoichiometries of the cathode materials and, thus, possible differences in the reaction mechanisms, the model is used to describe the electrochemistry of each individual cell.

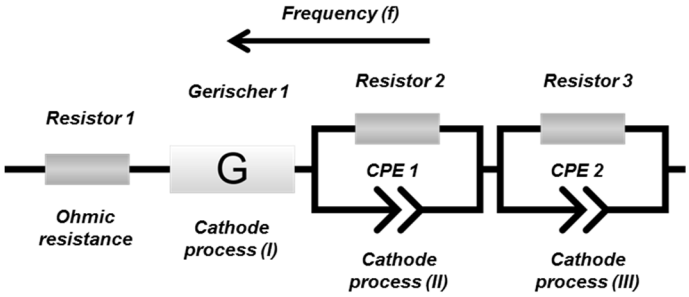

Figure 5.35: Utilized EC-model for the description of physicochemical process in symmetrical, electrolyte-supported SOFCs with a standard LSCF cathode (also expanded for the electrochemical description of LSF and LSC cathodes).

Table 12: ***Signal comparison of literature and experimental data of electrolyte-supported SOFCs with standard LSCF cathodes***

Element	*Frequency*	*Physicochemical Process*
Process (IV), R3/I2, ASC Process (III), R3/CPE2, ESC	0.07-1 Hz 1-5 Hz	Gas diffusion in the cathode structure
Process (III), Ws1, ASC Process (II), R2/CPE1, ESC	10-100 Hz 10-60 Hz	O^{2-}-diffusivity in the cathode bulk
Process (III), WS1, ASC Process (I), G1, ESC	10-100 Hz 100-500 Hz	Oxygen surface exchange kinetics

Figure 5.36 exemplarily depicts different fits of three ESCs equipped with LSCF- (A), LSF- (B) and LSC-cathodes (C), respectively. The experimental data is taken at an operating temperature of 900 °C, after 48 h periods at a current density of 0.75 $A.cm^{-2}$ and under humid air conditions. Additionally, all represented measurements are performed at a constant potential of 0.2 V vs. Pt-reference in the presence of a Crofer 22 H Cr-source.

The experimental data for ESCs with LSCF-cathodes shows a good correlation to the EC-fit. Here, the residual represents a sufficient distribution of the real and imaginary part of the impedance, respectively (A1). In the frequency range between 100-1000 Hz, a slight sinusoidal signal can be detected, referring to a small systematic error of the fit. In this case, the maximum deviation between experimental data and fit data has a value of 2 %.

However, for LSF- (B1) as well as LSC-cathodes (C1) stronger errors within the EC-model fit are shown. For LSF, a sinusoidal residual behavior is overlapping the complete frequency range which indicates an even more complex electrochemical behavior than expected and described by the utilized model.

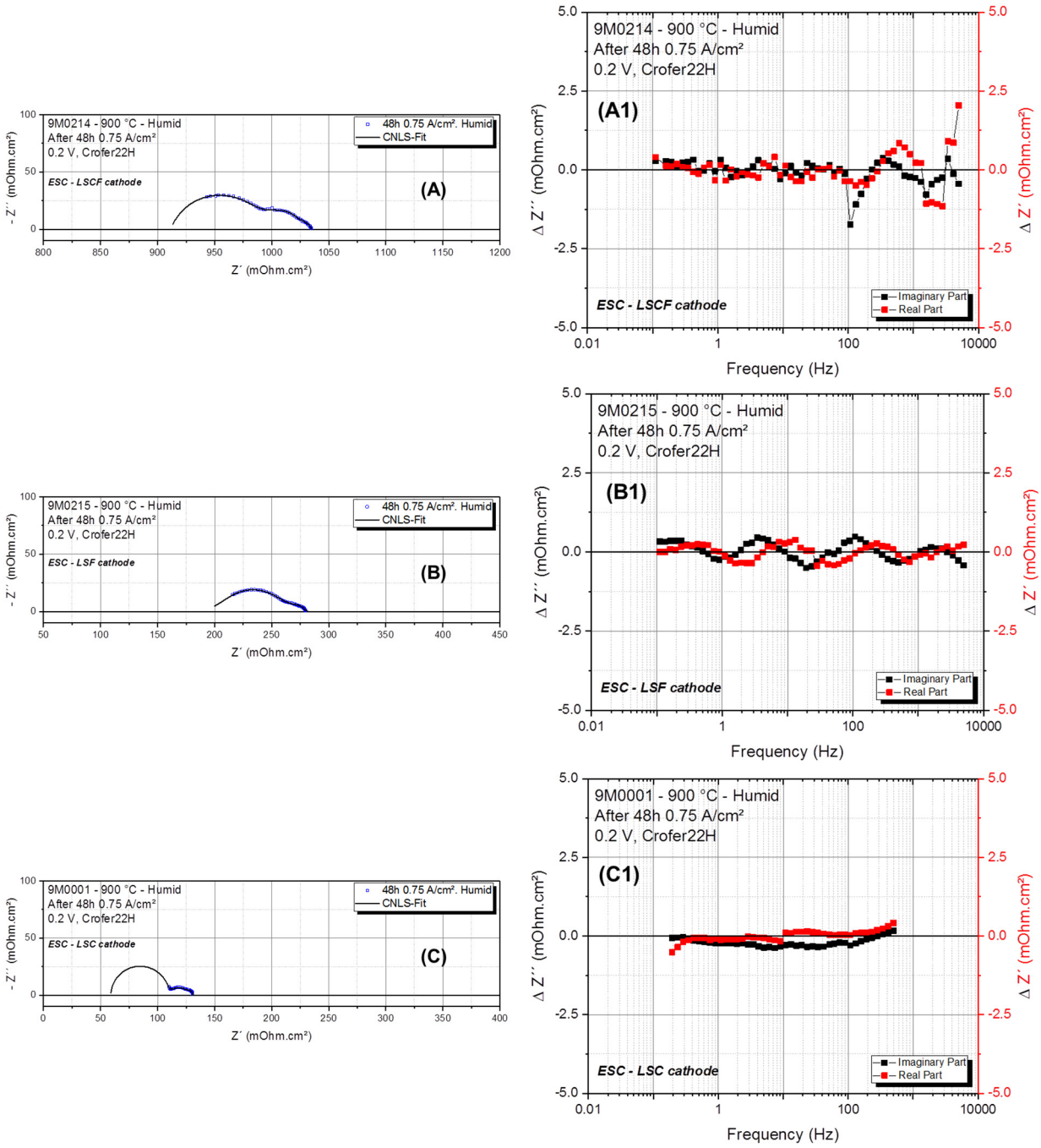

Figure 5.36: (A/B/C) Measured data incl. fit and process identification within the curves, together with (A1/B1/C1) the corresponding residual-plots for LSCF, LSF and LSC-cathodes.

5.2.4. Electrochemical In-Operando Analysis of ESCs: In-Depth Analysis

The current density (i.e. overpotential) related in-depth analysis of processes R2 and R3 for ESCs equipped with LSCF-cathodes in absence (A1/A2) and presence of chrome (B1/B2) is presented in Figure 5.37. It is shown that the values for both resistances, R2 and R3, are in accordance to the literature (R2, exp. 10 mOhm.cm²; R2, lit. 8-50 mOhm.cm² [60] and R3, exp. 25-100 mOhm.cm², R3, lit. 2-100 mOhm.cm² [60]).

Here, the absolute value of R3 shows variations of 70 mOhm.cm² in the absence and presence of chrome. By consideration that R3 can be related to the process of cathode-sided gas diffusion, the deposition of SrCrO4 could have caused this increase in resistance.
Additionally, R2 slightly increases with higher overpotentials in humid air and the presence of chrome. Such a phenomenon could be caused by Cr-deposition within the porous structure. It also has to be stated that even though anode contributions have been completely excluded, only small developments of the resistances can be observed.

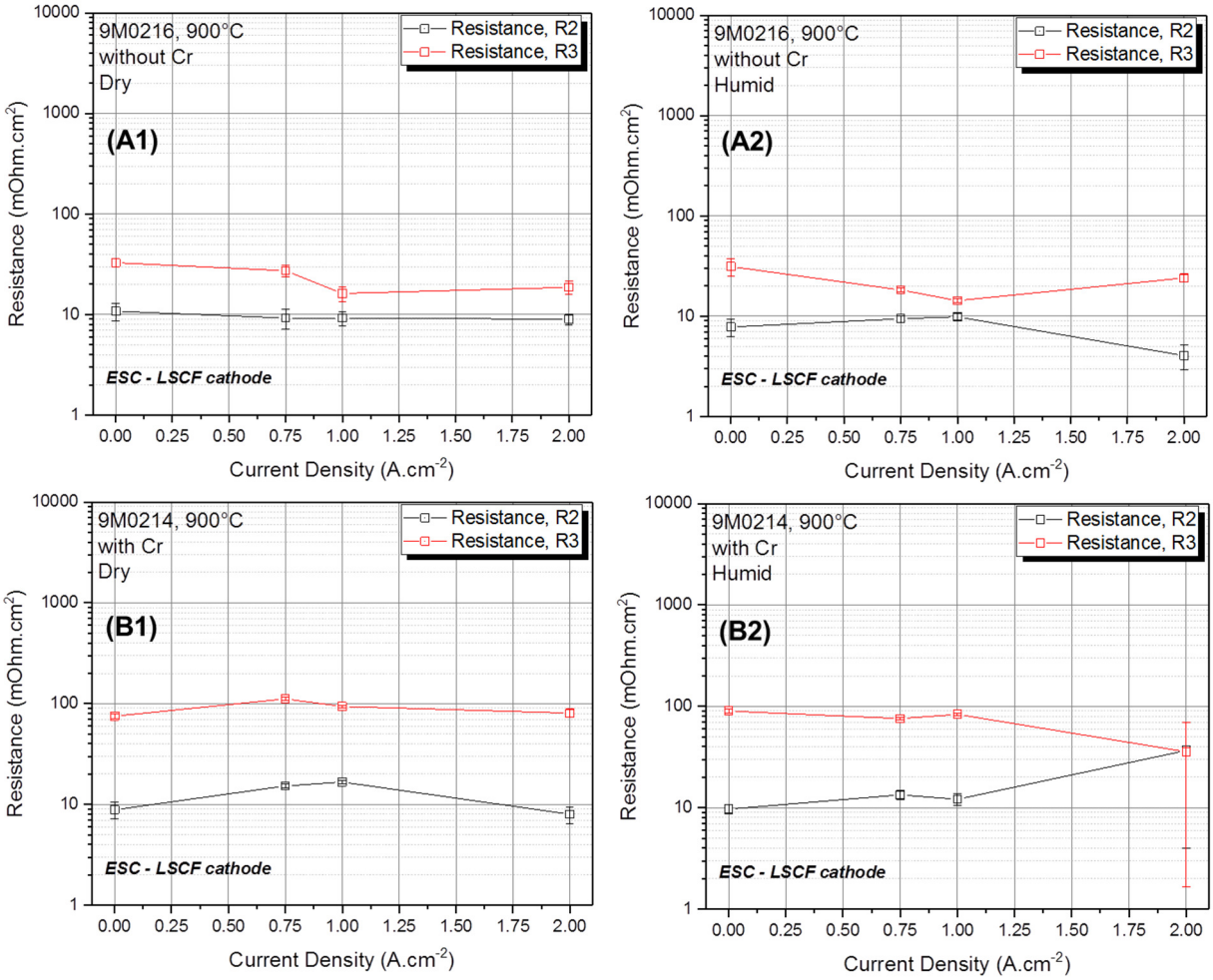

Figure 5.37: ESC-LSCF: Current density dependent development of R2 and R3 for 900 °C, dry (A1/B1) and humid (A2/B2) cathode-gas atmospheres as well as in absence (top) and presence (bottom) of chrome.

For further analysis of the cathode related processes with regard to chrome deposition, the development of the Gerischer-element is illustrated in Figure 5.38.
By comparison of both spectra a clear tendency towards higher resistive values of the Gerischer-element is revealed in the presence of chrome (B). Even though a decrease of the element is shown with increasing overpotentials in humid atmospheres, the final value is still 400 mOhm.cm² larger than in the absence of a Cr-source (A). Since the process of oxygen surface exchange kinetics is assumed to be described by the Gerischer-element, this process can be limited by the formation of Cr-species such as $SrCrO_4$ (in competition with the oxygen reduction reaction).

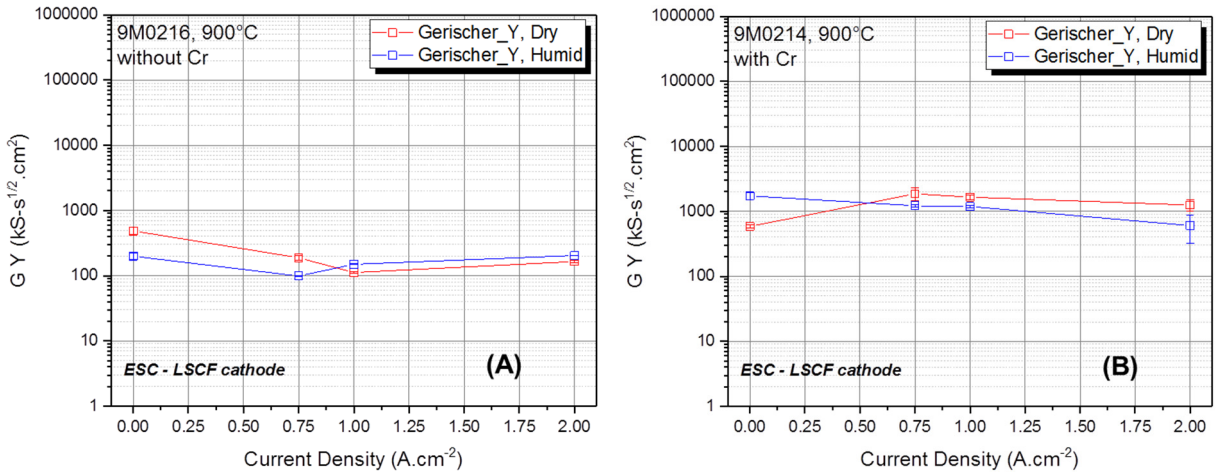

Figure 5.38: ESC-LSCF: Current density dependent development of the Gerischer-element G_Y in dry and humid atmospheres for 900 °C in the absence (A) and presence of chrome (B).

As already mentioned in chapter 5.2.2, the in-depth analysis of ESCs that are equipped with LSF- as well as LSC-cathodes and are not exposed to a Cr-source, cannot be realized as both measurements show strong errors within the experiments (mostly test-rig related). Nevertheless, it is possible to compare the electrochemical response of both materials in the presence of a Cr-source (Figure 5.39).

Here, sample 9M0215 (LSF-cathode) shows an increase of both resistances (A1). This behavior is pronounced especially in humid environments (A2). Compared to samples with LSCF-cathodes, the gas diffusion resistance R3 increases up to an almost identical value of 100 mOhm.cm² (after measurements at 2 A.cm^{-2} in humid air). However, also R2 increases with time and higher overpotentials to a value of 55 mOhm.cm² (LSCF: 38 mOhm.cm²).

In case of using LSC-cathodes, an interchange of both resistances is revealed. Weaker and almost continuous trends (for dry and humid air conditions, B1/B2) of the gas diffusion resistance R3 (8-10 mOhm.cm²) as well as the oxygen-ion diffusivity resistance R2 (32-40 mOhm.cm²) are revealed.

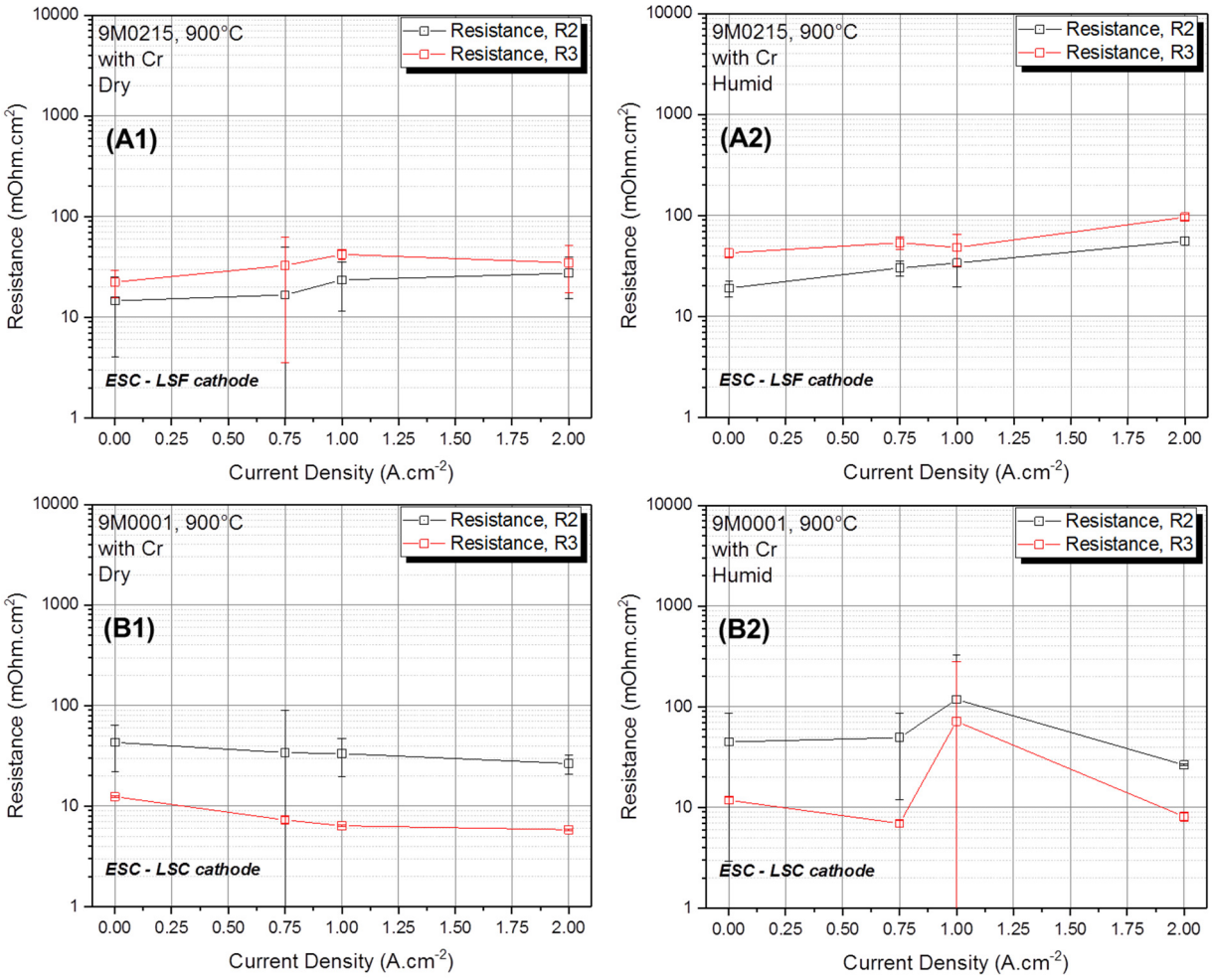

Figure 5.39: ESC-LSF and ESC-LSC: Current density dependent development of R2 and R3 for 900 °C, dry (A1/B1) and humid (A2/B2) cathode-gas atmospheres in the presence of chrome.

Comparing the development of the Gerischer element of LSF- and LSC-cathodes in Figure 5.40, it is shown that LSC (B) develops with time and increasing current whereas LSF (A) remains constant. Sample 9M0001 (LSC-cathode) starts from smaller values as observed for sample 9M0215 (8500 kS-s$^{1/2}$.cm² < 20,000 kS-s$^{1/2}$.cm²), however, final measurements at an overpotential of 2 A.cm^{-2} reveal a value of 17,000 mOhm.cm². It has to be stated that in comparison to LSCF-cathodes, the respective resistance-values of ESCs with LSF and LSC-cathodes are between 1-2 orders of magnitude larger.

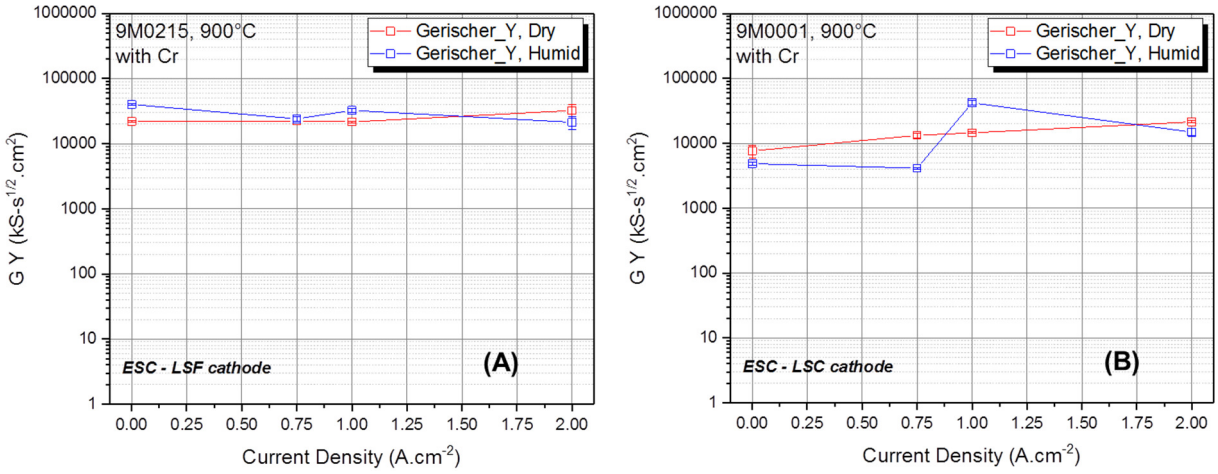

Figure 5.40: ESC-LSF and ESC-LSC: Current density dependent development of the Gerischer-element G_Y in dry and humid atmospheres for 900 °C for LSF- (A) and LSC-cathodes (B) in the presence of chrome.

In general, the electrochemical in-depth analysis of ESCs with LSCF- and LSF-cathodes reveals strongly increased resistance-values for the cathode-gas diffusion process R3 and an increasing oxygen-ion diffusivity process contribution in the presence of chrome. For LSC, however, no degradation trend of both resistances can be observed. With regard to the oxygen surface exchange kinetics (charge transfer process), which are represented by the Gerischer-element, LSCF cathodes show noticeably increased values in the presence of a Cr-source than in its absence. Contrary to LSCF-cathodes, LSF- and LSC-cathodes reveal higher charge transfer resistances, with only LSC-cathodes showing an increasing degradation trend rather than a continuous trend (all related to the current density and the operational time).
By analyzing these results, one can assume strong formations of Cr-species for all three cell types (incl. LSCF-, LSF-and LSC-cathodes) which lead to increased values of gas, oxygen-ion diffusion processes as well as charge transfer reactions.
In order to prove or disprove these assumptions, several post-test analyses are performed.

5.2.5. ESC Post-Test Analysis

In a first step, analogously to the post-test analysis of ASCs, ICP-OES measurements are performed to determine the exact amount of chrome deposits within the specimen. It can be stated that the highest amounts of Cr-deposits are found within ESCs which are equipped with LSC-cathodes (see Figure 5.41). Here, the amount of Cr-deposits (26.40 µg) is more than 3x higher as observed for LSF (7.99 µg) and even more than 12x higher as detected for LSCF-cathodes (2.13 µg). Since cobalt is the electrochemical most active element on the B-site of the perovskite material, higher chrome concentrations in the atmosphere are inevitably leading to larger amounts of deposits. There is no such thermodynamical explanation for the low amount of Cr-species within LSCF-cathodes, which still show a defined concentration of cobalt. However, sufficient amounts of Cr-species have been deposited which can influence the cells electrochemistry and accelerate performance degradation.

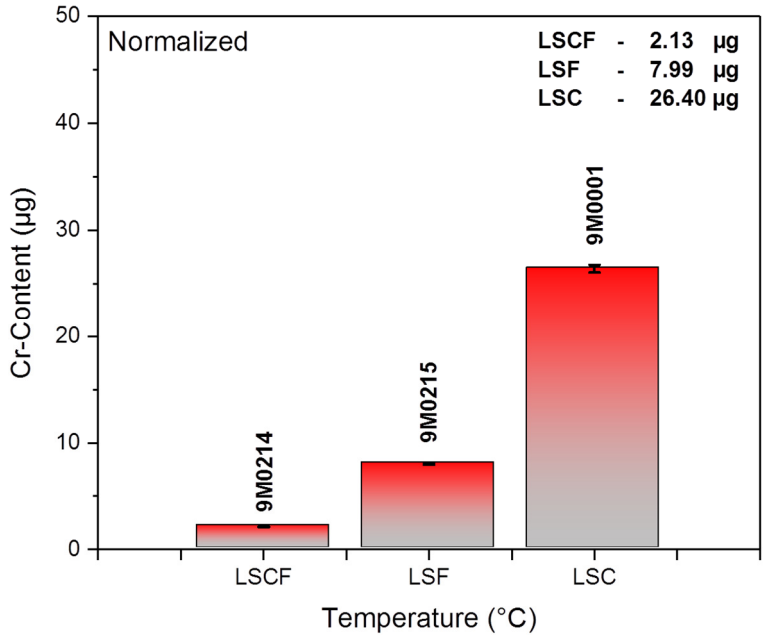

Figure 5.41: ICP-OES measurements of all three Cr-exposed electrolyte-supported SOFC samples (equipped with LSCF, LSF and LSC-cathodes). The values are normalized to the respective weight of the sample and cathode-layer.

In Figure 5.42, the complete XPS-survey spectra of all electrolyte-supported SOFCs are described. A Cr(2p3)-signal double-peak can be detected for each individual cell, confirming the experimental findings of the ICP-OES experiments. Contrary to the ICP-OES analysis, less intense Cr-signals are shown for ESCs with LSC-cathodes. As the XPS-method is known to be a surface sensitive analysis procedure with a penetration depth of only a few nanometers, it is possible that higher amounts of Cr-deposits can be found in the LSC-structure rather than on its surface. However, these features cannot be sufficiently analyzed with the XPS-method. Furthermore, within the LSC spectrum, a stronger signal background as seen of LSCF- and LSF-cathodes (especially for high binding energies, 850-1400 eV) can be observed. Nevertheless, regardless of their cathode compositions, all survey spectra reveal larger amounts of Cr-deposits within ESCs than detected for ASCs. Higher cathodic current densities (i.e. 2 $A.cm^{-2}$) and larger particle sizes (2 µm, ESCs > 0.8 µm, ASCs), inducing higher local overpotentials, are considered as key factors for these findings.

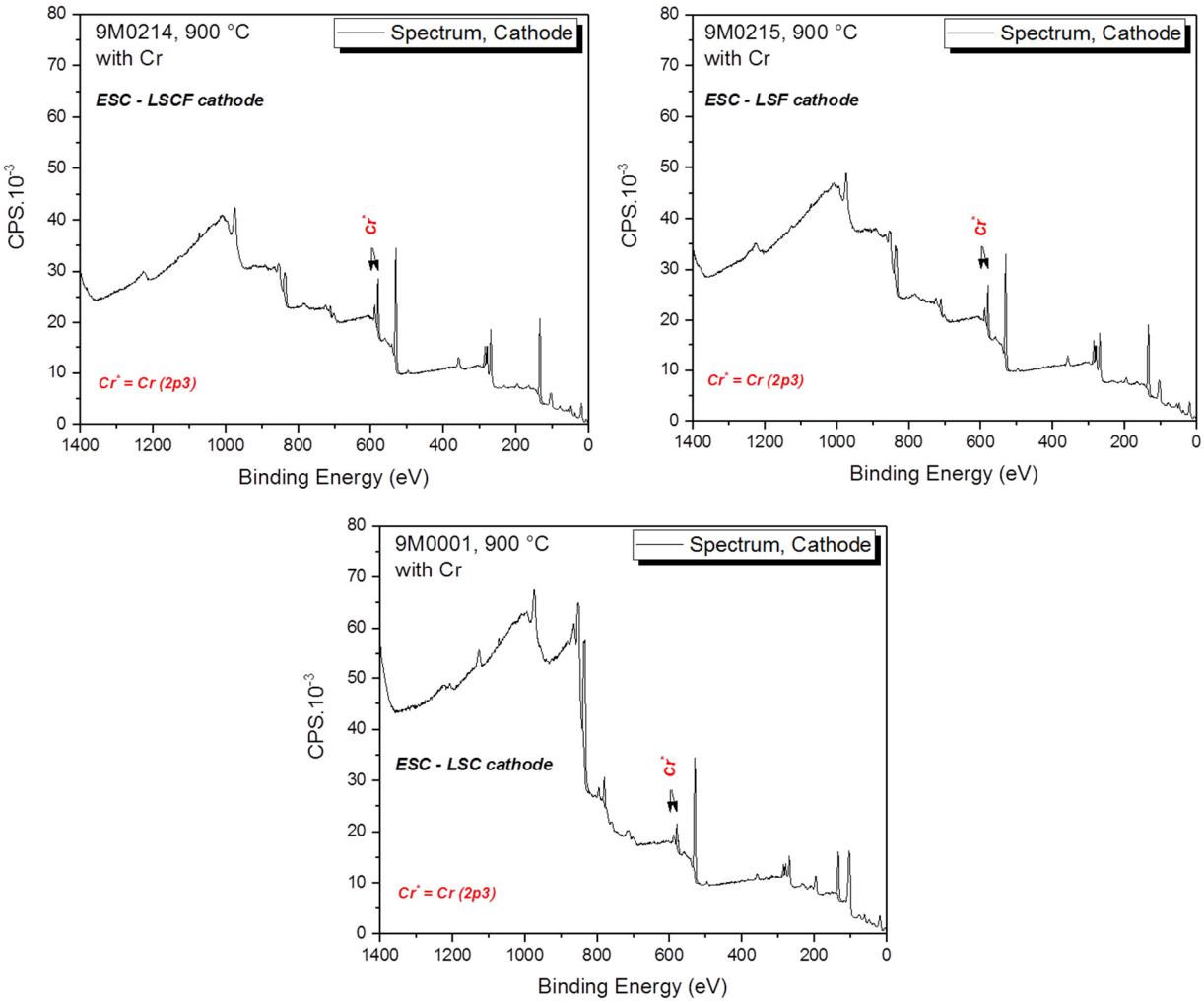

Figure 5.42: XPS-spectra of the elemental composition of electrolyte-supported SOFCs which are equipped with either LSCF-, LSF- or LSC-cathodes and are operated at various current densities at. All measurements are performed on the cathode surface.

Since Sr-signals show the same behavior as already described for ASCs, it is solely focused on the evaluation of the Cr-peaks (see Figure 5.43). It can be stated that the highest amounts of Cr-deposits near the surface region can be found for ESCs equipped with either LSCF- or LSF-cathodes. Both samples show large concentrations of Cr(VI)-species (67.1 % for LSCF- and 65.6 % LSF-cathodes). In comparison to the analysis of ASCs, the ratio between Cr(VI)- and Cr(III)-species for ESCs, operated at 900 °C, is more than 2:1 whereas for ASCs, a ratio of 1:4 (for experiments according to the ASC measurement schedule, sample 9M0199) and 1:2 for (for measurements at constantly high overpotentials, sample 9M0231) is detected. In case of LSC-cathodes, the analysis reveals lower concentrations of Cr(VI)-species and, thus, a ratio of Cr(VI) vs. Cr(III) of almost 1:1. It can be noticed that a reduction of the amount of Cr(VI) directly affects the concentration of Cr(III)-species and vice versa. Furthermore, the presence of $Cr(III)(OH)_3$ is revealed. Here, LSC-cathodes show stronger relative contents than observed for LSCF- and LSF-cathodes. However, it is not possible to define the total amount of chrome with help of the XPS-method, as only an area that equals the measuring spot size, is characterized.

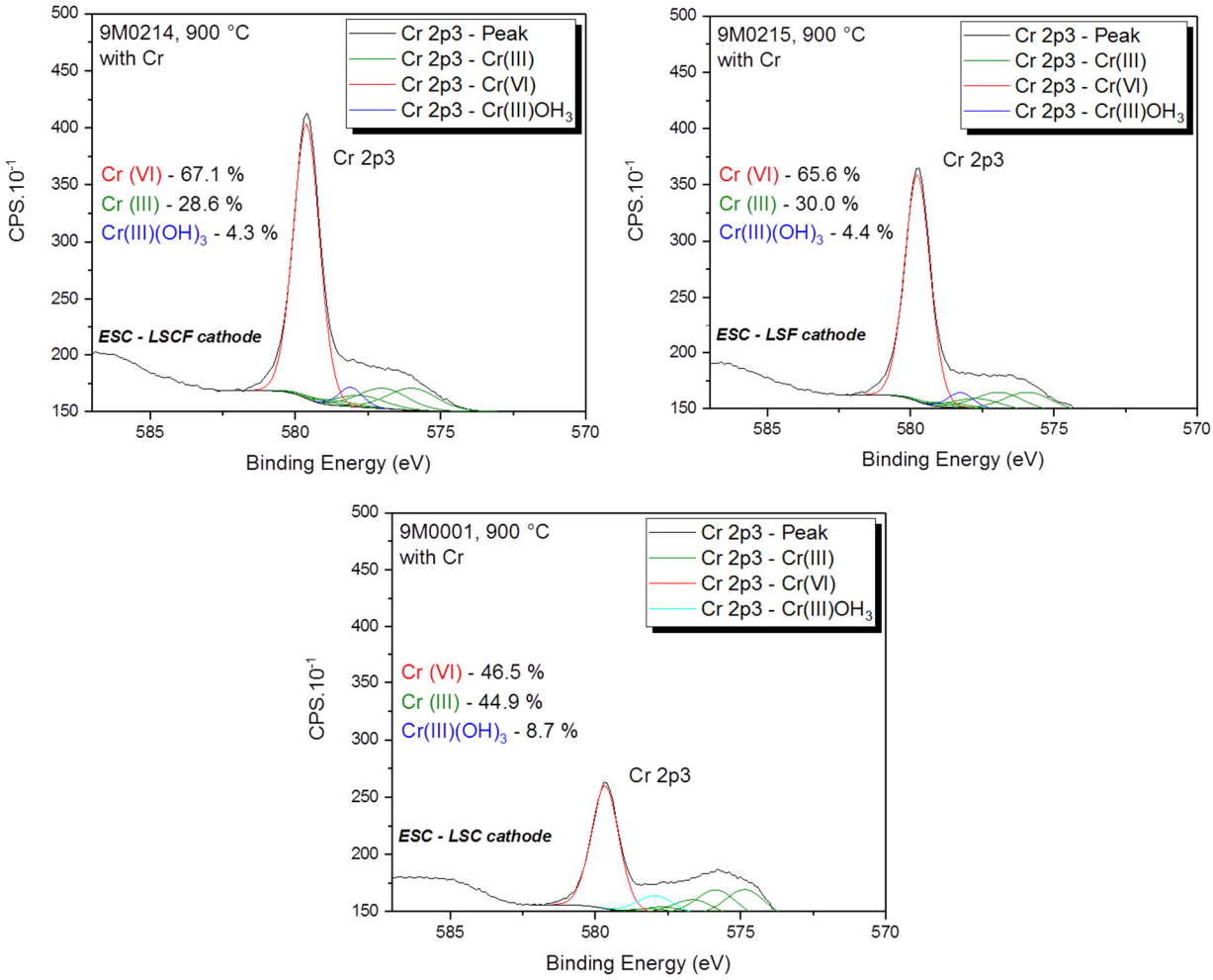

Figure 5.43: XPS in-depth analysis of occurring Cr-signals for symmetrical, electrolyte-supported SOFCs (half-cells), which are equipped with LSCF-, LSF- and LSC-cathodes and operated at a temperature of 900 °C.

In a last step, SEM top-views of all three samples are depicted in Figure 5.44. A strong formation of agglomerated particles on the entire surface of sample 9M0214 (LSCF) and 9M0215 (LSC) is illustrated. As XPS-analysis already revealed an enhanced presence of Cr-species and Cr-related Sr-species close to the LSCF- and LSF-cathode surface, agglomerated particles to be $SrCrO_4$ can be strongly assumed. Since the XPS procedure did not confirm the presence of larger amounts of platinum, one can exclude stronger depositions of Pt-species from the current collector that may cause this topography. According to the microscopical evaluation, the formation of $SrCrO_4$ seems to occur on top of the cathode without affecting the cathode structure beneath. However, by comparison of the microscopic results from ESCs (with LSCF- and LSF- cathodes) with the analysis of an anode-supported sample that has also been operated at high current densities, such as sample 9M0231 (see chapter 5.1.5, Figure 5.23), an integration of the cathode surface structure is assumed. After previous densification of the porous cathode structure by deposition of chrome, further Cr-species primarily deposit at these spots and form dense agglomerates. With continuation of operation, larger areas of $SrCrO_4$ agglomerates are formed, leading to the formation of a dense phase. In case of LSF-cathodes an advanced growth of $SrCrO_4$-agglomerates can be stated as well as tendencies towards merging of individual agglomerates and, thus, the formation of a dense layer.

According to the literature and experimental findings for internal cell-stack tests, this behavior supports a chemical mechanism behind the formation of the $SrCrO_4$-phases. However, for LSC cathodes no such trend can be observed. Here, solely a filling of the porous cathode structure can be observed. Although ICP-OES measurements revealed the highest concentration of Cr-deposits for LSC-cathodes, no dense layer on top of the cathode is formed. On the other hand, larger pore areas are partly filled which can be caused by an increased incorporation of Cr-species within the cathode rather than on its surface.

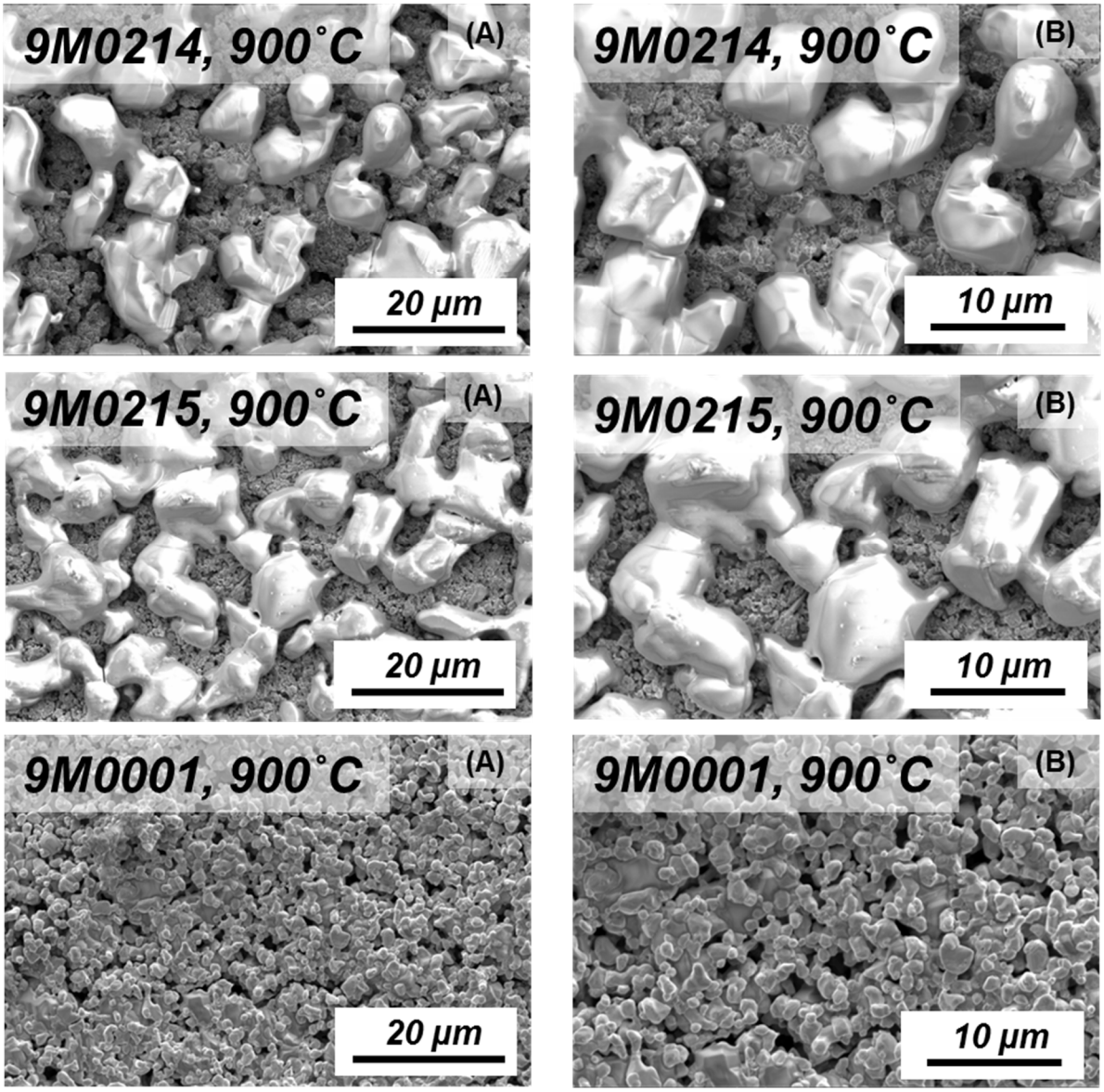

Figure 5.44: SEM top-view images with a magnification of 3000x (A) and 5000x (B) of samples 9M214 (LSCF), 9M0215 (LSF) and 9M0001 (LSC) which are exposed to chrome at an operating temperature of 900 °C according to the ESC measuring schedule.

The in-depth analysis of symmetrical electrolyte-supported SOFCs (half-cells), which are equipped with either LSCF-, LSF- or LSC-cathodes, has helped to separate influences of Cr-poisoning on the electrochemistry of the cathode materials from any superimposing anode degradation processes. With the introduction of a suitable EC-model, it is possible to identify cathode processes such as the oxygen surface exchange kinetics, the oxygen-ion diffusivity

and the gas diffusion. Furthermore, by comparison of the individual process-related resonance frequencies and resistance-values, a correlation to the literature model (KIT-model developed for ASCs) is shown.
For LSCF-cathodes, it is possible to detect increased resistances for the processes of gas diffusion (R3) as well as oxygen-ion diffusivity (R2) in the presence of a Cr-source. Furthermore, a strongly enhanced resistive behavior has been observed for the oxygen surface exchange kinetics (G1). These trends can be assumed to be mostly Cr-related as non-exposed samples do not show these effects. Additionally, the post-test analysis reveals the presence of Cr-species for LSCF-cathodes that have been operated in its presence. Strong Cr-deposits are found on top of the entire LSCF-surface by simultaneously reducing the electrode porosity. According to the XPS-analysis, these deposits can be assumed to be $SrCrO_4$. Related to the electrochemical process development of LSCF-cells, the formation of porosity reducing $SrCrO_4$-deposits on the cathode surface can lead to increased gas diffusion resistances. Simultaneously, as besides Cr(VI)- also Cr(III)-species are detected, an infiltration of Cr-species at least within the first few nanometers of the electrode can be assumed. Since infiltrated species also decrease the porosity of the LSCF-material, the gas transport is hindered, inducing higher resistances. Due to only small resistance-values for process R2, the oxygen ion diffusivity is assumed to be less affected by the deposition of chrome close to the cathode surface.
In comparison to LSCF, LSF-electrodes show continuous increases of both resistances, R2 and R3, respectively. Even though this development can be detected for dry and humid air conditions, a stronger increase of the degradation tendency can be determined in humid atmospheres. Analogously to LSCF, the post-test analysis illustrates the presence of $SrCrO_4$-deposits on the electrode surface. As, besides an increased value for the oxygen ion diffusivity, also large amounts of Cr(III)-species are detected, one can expect even higher Cr-concentrations within the LSF-cathode structure as seen for LSCF.
Contrary to LSCF- and LSF-cathodes, LSC does not exhibit agglomerated $SrCrO_4$-particles on the electrode surface. Nevertheless, an increased filling of the cathode pores can be observed. With regard to the electrochemistry, LSC-cathodes show lower values of gas diffusion but enhanced oxygen-ion diffusion resistances. This, together with the highest detected concentration of Cr-deposits, points to an increased Cr-infiltration of the cathode structure.
Considering the process of oxygen surface exchange kinetics (G1), both, LSF- and LSC-electrodes, show higher resistance values as LSCF-cathodes. However, only LSC shows a continuously increasing value of G1, indicating stronger Cr-penetration depths towards the TPB. However, since the utilized methods do not allow for in-depth investigations of the TPB, it is not possible to determine the amount of Cr-species and their oxidation state in the electrochemically most active area.

6. Summary & Conclusion

Within the work of this thesis, it was proven that the Cr-related degradation of anode-supported as well as electrolyte-supported SOFCs is strongly dependent on the operating temperature, the cathode-gas humidity, the applied current densities (i.e. the overpotential) and the cathode composition.

Starting with the analysis of ASCs, it was known that with increasing operating temperatures, also the evaporation of either CrO_3 or $CrO_2(OH)_2$ (dry or humid air conditions) is favored and, thus, the Cr-partial pressure within the gas chamber noticeably increases. A microscopical analysis of the topography of ASCs after operation at temperatures between 900 °C-650 °C showed an increased deposition of $SrCrO_4$-species on the LSCF-cathode surface, leading to a reduction of the cathode porosity by padding of the pores. Besides the formation of $SrCrO_4$ (Cr(VI)) also Cr(III) deposits were found. Contrary to Cr(VI)-species, the presence of Cr(III) was detected close to the cathode surface as well as at the TPB (at least for 900°C). Additionally, it can be stated, that with decreasing operating temperatures, less Cr(VI)- and more Cr(III)-species were formed. With this knowledge, it can be stated that the formation of $SrCrO_4$-species was mainly induced by the temperature, as all cells were operated in accordance to the ASC measuring schedule (i.e. with the same variation in humidity and applied overpotentials).

With help of the electrochemical impedance spectroscopy (EIS), it was possible to interpret changes of the individual processes in relation to the cathode-gas humidity and the applied overpotentials. In humid environments (i.e. air with 3.5 % H_2O), EIS analysis revealed increasing degradation tendencies of the process related resistances. Furthermore, also with applying defined overpotentials, the cell degradation increased. Here, major degradation tendencies were observed with the initial application of a continuous load as well as with high overpotentials ($\geq$ 0.75 $A.cm^{-2}$). In order to prove the influence of humidity and high cathodic-overpotentials, experiments at a constant current density of 2 $A.cm^{-2}$ in humid environments were performed. Here, the post-test analysis revealed higher amounts of deposited Cr-species and an increased ratio between Cr(VI)- and Cr(III)-species. This proved a significant influence of the applied humidity and overpotential on the deposition and formation of Cr-species. Furthermore, EIS measurements indicated slight performance recoveries with switching from high overpotentials back to OCV (e.g. from 1 $A.cm^{-2}$ in dry air to OCV in humid air humid, see ASC measuring schedule).

With the implementation of the 2-D DRT-method, it was possible to identify and distinguish four different ASC processes. By comparison of the process related time constants and frequencies with the literature data, the most common EC-model (i.e. the KIT-model for anode-supported SOFCs) was modified to the experimental findings as well as some test-rig induced properties. With this knowledge, it was possible to confirm the presence of at least one additional process, which develops at temperatures below 800 °C and is strongly superimposed by anodic contributions. According to the KIT-model as well as the experimentally determined resonance frequency the process was assumed to be most likely cathode related. As, due to strong contributions of the anode, it was not possible to sufficiently separate anode and cathode related time constants, half-cell measurements were

performed to completely exclude any influence of the anode layer. Furthermore, to investigate the influence of the B-site stoichiometry of the cathode material on its response to Cr-poisoning, LSF- and LSC-materials were evaluated in addition to the standard LSCF-material. To describe the system related electrochemistry, an EC-model with three time constants was developed. In accordance to the modified EC-model for anode-supported SOFCs, the model should describe the oxygen surface exchange kinetics as well as the processes of oxygen ion diffusivity and gas diffusion on the cathode side. It turned out that a Gerischer-element instead of a Warburg-element (as utilized for ASCs), provided the best theoretical description of the cathode-related charge transfer process. It can be assumed that this process is strongly overlapped by anode contributions within ASCs. Even though the developed EC-model was adequate for the description of LSCF-cathodes, it can be improved for its use with regard to LSF- and LSC-cathodes.

The electrochemical in-depth analysis by EIS revealed a strongly increased resistive behavior of the gas diffusion resistance for LSCF- and LSF-cathodes. Here, an advanced formation of $SrCrO_4$-species on the cathode surfaces can be confirmed to be the main reason for these findings. Additionally, it can be stated that no such $SrCrO_4$-agglomerates were found for LSC-cathodes. In accordance to the theory, also the gas diffusion resistance for these cathodes showed a less pronounced resistive behavior. In terms of the process of oxygen-ion diffusion, solely LSF- and LSC-cathodes showed increased resistances. As the ICP-OES analysis revealed the highest amount of Cr-deposits as well as Cr(III) for LSC- followed by LSF-cathodes, one can assume a larger penetration depth of Cr-species within the electrodes. Deposited Cr-species within the electrode structure can cause blocking of oxygen-ion conduction pathways and, thus, an increased resistive behavior of the ionic transport. This assumption can be further concretized as also the charge transfer resistance (oxygen surface exchange kinetics) showed resistance values that are increased by an order of magnitude compared to LSCF-electrodes. Here, again, penetrating Cr-species can cause blocking of electrochemically active areas of the cathode by simultaneously increasing the related resistance.

However, with respect to LSC-cathodes, the results can be discussed controversially. As highly reactive cobalt in LSC tends to change its oxidation and valence state (supported by high overpotentials), leading to an increased disassembly of strontium out of the lattice structure, one could have assumed to detect an increased amount of $SrCrO_4$ on the cathode surface. Furthermore, due to the lattice destabilization, also an inclusion of chrome into the perovskite lattice is facilitated and can be possible. Latter process would be able to describe higher amounts of Cr within the LSC-cathode structure as on its surface.

In order to conclude the experimental findings related to the previously defined goals of this thesis, it can be stated that each cell that was exposed in-operando to a Cr-source revealed the presence of Cr(VI)- as well as Cr(III)-species. Here, Cr(VI) was identified as $SrCrO_4$ and solely found on the cathode surface, whereas Cr(III)-species were located on the electrode surface, within the cathode structure and at the TPB. Larger amounts of $SrCrO_4$ were detected after cell-operation in humid environments and at temperatures above 750 °C. Additionally, the ratio between $SrCrO_4$ (i.e. Cr(VI)) and Cr(III)-species on the cathode surface was increased by the application of high current densities (2 $A.cm^{-2}$). As the formation of $SrCrO_4$

is thermodynamically preferred, mainly the Cr-concentration within the gas-phase as well as the gas-flow velocity should influence its formation.
Nevertheless, these results showed that, in fact, the poisoning procedure can be directly supported with the application of higher cathodic overpotentials which lower the initial activation energy to start the process. Furthermore, even though the electrochemically most active area of the electrode is located in close proximity (several µm) to the TPB it is possible that the reaction occurs next to the current collector on the cathode surface. Contrary to this assumption and, even more likely, high current densities can indirectly promote the formation of $SrCrO_4$ as they induce a change of the oxidation state of cobalt within the cathode lattice that simultaneously causes a destabilization by disassembly of strontium from the perovskite (as discussed for LSC). Disassembled strontium-/oxide can then diffuse towards the grain boundaries and undergo a chemical reaction with gaseous Cr(VI)-species.
In case of the formation of Cr(III)-species again, both, a chemical as well as pure electrochemical formation mechanism are possible. Here, the question is whether electrons from the external circuit are used for the development of Cr(III) or if a chemical reaction mechanism (incl. the formation of metastable intermediates) is the main reason for its reduction. According to the nuclei formation theory, also Cr_2O_3-species (i.e. Cr(III)) can be formed as a byproduct within the reaction of previously formed Cr-Sr-O nuclei with gaseous CrO_3- or $CrO_2(OH)_2$-species [30]. Apart from that, it is possible that with the application of high cathodic overpotentials and, thus, a larger quantity of electrons, gaseous Cr(VI)-species are simply reduced to Cr(III) electrochemically. As measurements at (continuously) high overpotentials revealed an even increased ratio between Cr(VI)- and Cr(III)-species, the formation of Cr(III)-species on the cathode surface is assumed to be chemically induced. However, this assumption is only valid for the formation of Cr(III) on the cathode surface. Experimental findings of increased amounts of solely Cr(III)-species at the electrochemical highly active TPB point on a pure electrochemical reduction mechanism of chrome. As no Cr(VI)-species (i.e. $SrCrO_4$) were found at the TPB, the validity of the nuclei formation theory can be excluded for this region.
Even though Cr-exposed samples showed noticeable increases of related process resistances during the operation of symmetrical electrolyte supported half-cells, only slight degradation tendencies were observed for anode-supported full-cells. Although extremely harsh operating conditions such as high overpotentials in humid air environments at low and high operating temperatures were applied, no complete performance losses had been observed. This confirms, as already expected, that the deposition of Cr-species noticeably affects the cell performance after long-term operation and, thus, can be considered as a long-term degradation mechanism.
Nevertheless, this work defined Cr-deposition promoting parameters such as high operating temperatures, humid environments and high cathodic overpotentials and helped to understand their influences on the local formation of Cr-species. In order to reduce the deposition of chrome within the system to a minimum, the cells should be operated at temperatures below 800 °C. Although it was possible to detect chrome species even at these temperatures, no influences on the cathode structure were detected. Furthermore, since electrochemical in-operando measurements identified enhanced resistance-values with slightly increasing the air

humidity up to a value of 3.5 %, cells/stacks should be operated in dry atmospheres at best. Additionally, applied current densities should not surpass values of 0.75 $A.cm^{-2}$ as higher values lead to relatively strong increased resistive behaviors. However, with help of this knowledge, further long-term degradation experiments can be performed which can help to gain a deepened understanding of the described degradation mechanisms and/or investigate less-harmful operational parameters. Finally, by setting optimized operational conditions, it should be possible to establish an optimal ratio between cell-performance and cell-lifetime.

7. Outlook

In the previous chapters of this work, several different parameters and their influence on the Cr-degradation behavior of SOFC cathodes were investigated. As, due to the large number of variables and the limited time-frame of a Phd-thesis, it was not always possible to fully isolate the influence of single parameters on the Cr-degradation behavior, further experiments can be performed.

Additionally, long-term tests with at least 1500 h of operation should be conducted. Especially in case of anode-supported SOFCs, long-term tests in combination with high operating temperatures, large overpotentials and humid air environments, would guarantee an increased deposition of Cr-species and, thus, enable a stronger influence of Cr(III)-species. Besides stronger pronounced electrochemical Cr-related cell degradation tendencies, this also facilitates the preparation and detection of these species.

Since higher amounts of Cr-deposits enable their microscopic detection within embedded SEM cross-sections, the Cr-poisoning behavior within the cathode structure as well as possible Cr-gradients towards the TPB can be detected. Otherwise, to exclude issues during the preparation of poisoned cells, the focused ion beam (FIB) procedure can be utilized. Here, with help of a highly energetic focused beam of ions, thin sample lamellae can be cut out of the sample structure and be analyzed by SEM and EDX using the same device.

I would also assume to perform a more detailed analysis regarding the cathode-gas humidity level and applied overpotential in combination with the advantageous of the 2-D DRT procedure. By changing operational parameters such as the water-content of the cathode-gas gradually, the DRT-method allows for an illustration of the development of related degradation processes. This enables better process identifications and possibly a more adequate separation of the process related time constants. In general, the 2-D DRT procedure should be stronger embedded within the establishment of a suitable EC-model (for each cell-concept), as its significance in the field of process-identification with regard to a change in the operational parameters cannot be denied.

As an experimental advice within the analysis of electrolyte-supported SOFCs, I would assume the synthesis of cathode materials with particle sizes of 0.7-0.8 µm (standard). Even though stronger Cr-degradation tendencies can be detected for cathodes with less electrochemical active areas (i.e. larger particle sizes), microstructural changes and, thus, influences on the degradation behavior cannot fully be excluded. However, with increasing the evaporation time also the deposition of Cr-species should be enhanced which guarantees their adequate detection.

Finally, to almost fully prevent Cr-poisoning, protective coatings can be applied to the metallic interconnect. These can effectively reduce the volatility of Cr-species and, thus, minimize Cr-related interactions with the cathode material and their influence on the cell performance [21,75–77].

8. Literature

1. Wei, B., Chen, K., Wang, C. C., Lü, Z. & Jiang, S. P. Cr deposition on porous La0.6Sr0.4Co0.2Fe0.8O3-δ electrodes of solid oxide cells under open circuit condition. *Solid State Ionics* **281,** 29–37 (2015).
2. De Haart, L. G. J., Mougin, J., Posdziech, O., Kiviaho, J. & Menzler, N. H. Stack degradation in dependence of operation parameters; the Real-SOFC sensitivity analysis. *Fuel Cells* **9,** 794–804 (2009).
3. Beez, A., Yin, X., Menzler, N. H., Spatschek, R. & Bram, M. Insight into the Reaction Mechanism of (La0.58 Sr0.40)(Co0.20 Fe0.80)O 3-δ Cathode with Volatile Chromium Species at High Current Density in a Solid Oxide Fuel Cell Stack. *J. Electrochem. Soc.* **164,** F3028–F3034 (2017).
4. Menzler, N. H., Sebold, D. & Wessel, E. Interaction of La0.58Sr0.40Co0.20Fe0.80O3-δcathode with volatile Cr in a stack test - Scanning electron microscopy and transmission electron microscopy investigations. *J. Power Sources* **254,** 148–152 (2014).
5. Menzler, N. H., Sebold, D. & Fang, Q. Chromium-Related Degradation of Thin-Film Electrolyte Solid Oxide Fuel Cell Stacks. *J. Electrochem. Soc.* **162,** F1275--F1281 (2015).
6. Singhal, S. C.; Kendall, K. *High Temperature Solid Oxide Fuel Cells - Fundamentals, Design and Applications*. (Elsevier Ltd., 2003).
7. Stambouli, A. B. & Traversa, E. Solid oxide fuel cells (SOFCs): A review of an environmentally clean and efficient source of energy. *Renew. Sustain. Energy Rev.* **6,** 433–455 (2002).
8. Neumann, A. Chrom-bezogene Degradation von Festoxid-Brennstoffzellen. (Ruhr-University Bochum, 2011).
9. Carrette, L. & Friedrich, K. A. Fuel Cells : Principles , Types , Fuels , and Applications. *CHEMPHYSCHEM* **1,** 162–193 (2000).
10. O´Hayre, R., Cha, S. W., Colella, W. & Prinz, F. B. *Fuel Cell Fundamentals*. (John Wiley & Sons Ltd., 2009).
11. Mun, A. B., Ritzmann, A. M., Pavone, M., Keith, J. A. & Carter, E. A. Oxygen Transport in Perovskite-Type Solid Oxide Fuel Cell Materials : Insights from Quantum Mechanics. **47,** 3340–3348 (2014).
12. Leonide, A. SOFC Modelling and Parameter Identification by means of Impedance Spectroscopy. (Karlsruher Institut für Technologie (KIT), 2010).
13. Tu, H. & Stimming, U. Advances, aging mechanisms and lifetime in solid-oxide fuel cells. *J. Power Sources* **127,** 284–293 (2004).
14. Mai, A. Katalytische und elektrochemische Eigenschaften von eisen- und kobalt-haltigen Perwoskiten als Kathoden für die oxidkeramische Brennstoffzelle (SOFC). (Ruhr-University Bochum, 2004).
15. Ormerod, R. M. Solid oxide fuel cells. *Chem. Soc. Rev.* **32,** 17–28 (2003).
16. Blum, L. *et al.* Solid oxide fuel cell development at Forschungszentrum Juelich. *Fuel Cells* **7,** 204–210 (2007).

17. Schütze, M. & Quadakkers, W. J. *Novel approaches to improving high temperature corrosion resistance*. (Woodhead Publishing Limited, 2008).
18. Sachitanand, R., Sattari, M., Svensson, J. E. & Froitzheim, J. Evaluation of the oxidation and Cr evaporation properties of selected FeCr alloys used as SOFC interconnects. *Int. J. Hydrogen Energy* **38,** 15328–15334 (2013).
19. Froitzheim, J. *et al.* Development of high strength ferritic steel for interconnect application in SOFCs. *J. Power Sources* **178,** 163–173 (2008).
20. *VDM ® Crofer 22 H*. (VDM Metals GmbH, 2010).
21. Jiang, S. P. & Chen, X. Chromium deposition and poisoning of cathodes of solid oxide fuel cells - A review. *Int. J. Hydrogen Energy* **39,** 505–531 (2014).
22. Simner, S. P. *et al.* SOFC Performance with Fe-Cr-Mn Alloy Interconnect. *J. Electrochem. Soc.* **152,** A740 (2005).
23. Konysheva, E. *et al.* Chromium Poisoning of Perovskite Cathodes by the ODS Alloy Cr5Fe1Y2O3 and the High Chromium Ferritic Steel Crofer22APU. *J. Electrochem. Soc.* **153,** A765 (2006).
24. Matsuzaki, Y. & Yasuda, I. Dependence of SOFC Cathode Degradation by Chromium-Containing Alloy on Compositions of Electrodes and Electrolytes. *J. Electrochem. Soc.* **148,** A126 (2001).
25. Hilpert, K. Chromium Vapor Species over Solid Oxide Fuel Cell Interconnect Materials and Their Potential for Degradation Processes. *J. Electrochem. Soc.* **143,** 3642 (1996).
26. Ebbinghaus, B. B. Thermodynamics of gas phase chromium species: The chromium oxides, the chromium oxyhydroxides, and volatility calculations in waste incineration processes. *Combust. Flame* **93,** 119–137 (1993).
27. Chen, X., Zhen, Y., Li, J. & Jiang, S. P. Chromium deposition and poisoning in dry and humidified air at (La0.8Sr0.2)0.9MnO3+δ cathodes of solid oxide fuel cells. *Int. J. Hydrogen Energy* **35,** 2477–2485 (2010).
28. Tucker, M. C., Kurokawa, H., Jacobson, C. P., De Jonghe, L. C. & Visco, S. J. A fundamental study of chromium deposition on solid oxide fuel cell cathode materials. *J. Power Sources* **160,** 130–138 (2006).
29. Jiang, S. P., Zhang, J. P. & Zheng, X. G. A comparative investigation of chromium deposition at air electrodes of solid oxide fuel cells. *J. Eur. Ceram. Soc.* **22,** 361–373 (2002).
30. Jiang, S. P., Zhang, S. & Zhen, Y. D. Deposition of Cr Species at (La,Sr)(Co,Fe)O3 Cathodes of Solid Oxide Fuel Cells. *J. Electrochem. Soc.* **153,** A127 (2006).
31. Zhen, Y. & Jiang, S. P. Characterization and performance of (La,Ba)(Co,Fe)O3cathode for solid oxide fuel cells with iron-chromium metallic interconnect. *J. Power Sources* **180,** 695–703 (2008).
32. Chen, X., Zhang, L. & Jiang, S. P. Chromium Deposition and Poisoning on (La0.6Sr0.4−xBax)(Co0.2Fe0.8)O3 (0≤x≤0.4) Cathodes of Solid Oxide Fuel Cells. *J. Electrochem. Soc.* **155,** B1093 (2008).
33. Finsterbusch, M. *et al.* Effect of Cr2O3 on the 18O tracer incorporation in SOFC materials. *Solid State Ionics* **181,** 640–645 (2010).

34. Bucher, E., Yang, M. & Sitte, W. In Situ Investigations of the Chromium-Induced Degradation of the Oxygen Surface Exchange Kinetics of IT-SOFC Cathode Materials La0.6Sr0.4CoO3−δ and La0.58Sr0.4Co0.2Fe0.8O3−δ. *J. Electrochem. Soc.* **159,** B592 (2012).
35. Lee, S.-N., Atkinson, A. & Kilner, J. A. Effect of Chromium on La0.6Sr0.4Co0.2Fe0.8O3-δ Solid Oxide Fuel Cell Cathodes. *J. Electrochem. Soc.* **160,** F629–F635 (2013).
36. Ardigò, M. R. *et al.* Interface reactivity study between La0.6Sr0.4Co 0.2Fe0.8O3-δ (LSCF) cathode material and metallic interconnect for fuel cell. *J. Power Sources* **196,** 2037–2045 (2011).
37. Bentzen, J. J., Hogh, J. V. T., Barfod, R. & Hagen, A. Chromium poisoning of LSM/YSZ and LSCF/CGO composite cathodes. *Fuel Cells* **9,** 823–832 (2009).
38. Viitanen, M. M., Welzenis, R. G. V, Brongersma, H. H. & Van Berkel, F. P. F. Silica poisoning of oxygen membranes. *Solid State Ionics* **150,** 223–228 (2002).
39. Miura, N., Okamoto, Y., Tamaki, J., Morinaga, K. & Yamazoe, N. Oxygen semipermeability of mixed-conductive oxide thick-film prepared by slip casting. *Solid State Ionics* **79,** 195–200 (1995).
40. Van Der Heide, P. A. W. Systematic x-ray photoelectron spectroscopic study of La1-xSrx-based perovskite-type oxides. *Surf. Interface Anal.* **33,** 414–425 (2002).
41. Simner, S. P., Anderson, M. D., Engelhard, M. H. & Stevenson, J. W. Degradation Mechanisms of La–Sr–Co–Fe–O3 SOFC Cathodes. *Electrochem. Solid-State Lett.* **9,** A478 (2006).
42. Yokokawa, H. *et al.* Thermodynamic and kinetic considerations on degradations in solid oxide fuel cell cathodes. *J. Alloys Compd.* **452,** 41–47 (2008).
43. Roehrens, D. *et al.* Formation of chromium containing impurities in (La,Sr)MnO3solid-oxide-fuel-cell cathodes under stack operating conditions and its effect on performance. *Ceram. Int.* **42,** 9467–9474 (2016).
44. Hamann, C. H. & Vielstich, W. *Elektrochemie*. (Wiley-VCH, 2005).
45. Vetter, K. J. *Elektrochemische Kinetik*. (Springer-Verlag, 1961).
46. Singhal, S. C. Solid oxide fuel cells for stationary, mobile, and military applications. *Solid State Ionics* **152,** 405–410 (2002).
47. Müller, A. C., Opfermann, J. R. & Ivers-Tiffée, E. Modelling and optimisation of solid electrolyte sintering behaviour by thermokinetic analysis. *Thermochim. Acta* **414,** 11–17 (2004).
48. Takeda, Y., Kanno, R., Noda, M., Tomida, Y. & Yamamoto, O. Cathodic Polarization Phenomena of Perovskite Oxide Electrodes with Stabilized Zirconia. *J. Electrochem. Soc.* **134,** 2656–2661 (1987).
49. Adler, S. B. Factors Governing Oxygen Reduction in Solid Oxide Fuel Cell Cathodes†. 4791–4843 (2004). doi:10.1021/CR020724O
50. Sase, M. *et al.* Interfacial reaction and electrochemical properties of dense (La,Sr) CoO3-δ cathode on YSZ (1 0 0). *J. Phys. Chem. Solids* **66,** 343–348 (2005).
51. Orazem, M. E. & Tribollet, B. *Electrochemical Impedance Spectrscopy*. (2008).
52. Bard, A. J. & Faulkner, L. R. *Electrochemical Methods*. (2001).

53. Primdahl, S. & M.Mogensen. Gas Diffusion Impedance in Characterization of Solid Oxide Fuel Cell Anodes. *J. Electrochem. Soc.* **146,** 2827 (1999).
54. Kim, J., Virkar, A. V, Fung, K., Mehta, K. & Singhal, S. C. Polarization Effects in Intermediate Temperature , Anode-Supported Solid Oxide Fuel Cells. *J. Electrochem. Soc.* **146,** 69–78 (1999).
55. Weber, A. Entwicklung von Kathodenstrukturen für die Hochtemperatur-Brennstoffzelle SOFC. (Karlsruher Institut für Technologie (KIT), 2002).
56. Barsoukov, E. & MacDonald, J. R. *Impedance Spectroscopy: Theory, Experiment, and Applications*. (Wiley-Interscience, 2005).
57. Macdonald, J. Impedance spectroscopy. *Ann. Biomed. Eng.* 289–305 (1992).
58. Adler, S. B. Limitations of charge-transfer models for mixed-conducting oxygen electrodes. *Solid State Ionics* **135,** 603–612 (2000).
59. Adler, S. B., Lane, J. A. & Steele, B. C. H. Electrode Kinetics of Porous Mixed-Conducting Oxygen Electrodes. *J. Electrochem. Soc.* **143,** 3554–3564 (1996).
60. Leonide, A., Rüger, B., Weber, A., Meulenberg, W. A. & Ivers-Tifée, E. Performance Study of Alternative (La,Sr)FeO3-δ and (La,Sr)(Co,Fe)O3-δ MIEC Cathode Compositions. **25,** 2487–2496 (2009).
61. Brichzin, V., Fleig, J., Habermeier, H. U., Cristiani, G. & Maier, J. The geometry dependence of the polarization resistance of Sr-doped LaMnO3microelectrodes on yttria-stabilized zirconia. *Solid State Ionics* **152–153,** 499–507 (2002).
62. Leonide, A., Sonn, V., Weber, A. & Ivers-Tiffée, E. Evaluation and Modeling of the Cell Resistance in Anode-Supported Solid Oxide Fuel Cells. *J. Electrochem. Soc.* **155,** B36–B41 (2008).
63. Sonn, V., Leonide, A. & Ivers-Tiffée, E. Combined Deconvolution and CNLS Fitting Approach Applied on the Impedance Response of Technical Ni/8YSZ Cermet Electrodes. *J. Electrochem. Soc.* **155,** B675 (2008).
64. Müller, A. Mehrschicht-Anode für die Hochtemperatur-Brennstoffzelle (SOFC). (Universität Fridericiana zu Karlsruhe, 2004).
65. Bunaciu, A. A., Udriştioiu, E. gabriela & Aboul-Enein, H. Y. X-Ray Diffraction: Instrumentation and Applications. *Crit. Rev. Anal. Chem.* **45,** 289–299 (2015).
66. FIZ Karlsruhe - Leibniz-Institut für Informationsinfrastruktur GmbH. ICSD-Database. (2018). Available at: https://icsd.fiz-karlsruhe.de/search/basic.xhtml.
67. Kollenberg, W. *Technische Keramik - Grundlagen, Werkstoffe, Verfahrenstechnik*. *Keramik* (Vulkan-Verlag, 2009).
68. Vernon-Parry, K. D. Scanning Electron Microscopy : An Introduction. *III-Vs Rev.* **13,** 40–44 (2000).
69. Menzler, N., Batfalsky, P. & Groß, S. Post-Test Characterization of an SOFC Short-Stack after 17,000 Hours of Steady Operation. *ECS Trans.* **35,** 195–206 (2011).
70. Moulder, J. F., Stickle, W. F., Sobol, P. E. & Bomben, K. D. *Handbook of X-Ray Photoelectron Spectroscopy*. (Physical Electronics, Inc., 1995).
71. Mertens, A. & Granwehr, J. Two-dimensional impedance data analysis by the distribution of relaxation times. *J. Energy Storage* **13,** 401–408 (2017).
72. Schönleber, M. & Ivers-Tiffée, E. Approximability of impedance spectra by RC

elements and implications for impedance analysis. *Electrochem. commun.* **58,** 15–19 (2015).

73. Oustaloup, A., Levron, F., Mathieu, B. & Nanot, F. M. Frequency-band complex noninteger differenciator: characterization and systhesis. *IEEE Trans. Circuits Syst. I Fundam. Theory Appl.* **47,** 25–39 (2000).
74. Yin, X. & Singheiser, L. Unpublished Results. (2018).
75. Hua, B. *et al.* A promising NiCo2O4 protective coating for metallic interconnects of solid oxide fuel cells. *J. Power Sources* **195,** 7375–7379 (2010).
76. Chen, X., Hou, P. Y., Jacobson, C. P., Visco, S. J. & De Jonghe, L. C. Protective coating on stainless steel interconnect for SOFCs: Oxidation kinetics and electrical properties. *Solid State Ionics* **176,** 425–433 (2005).
77. Grünwald, N., Sebold, D., Sohn, Y. J., Menzler, N. H. & Vaßen, R. Self-healing atmospheric plasma sprayed Mn1.0Co1.9Fe0.1O4 protective interconnector coatings for solid oxide fuel cells. *J. Power Sources* **363,** 185–192 (2017).